

GLAUCONITE AS AN INDICATOR OF SEQUENCE STRATIGRAPHIC
PACKAGES IN A LOWER PALEOCENE PASSIVE-MARGIN
SHELF SUCCESSION, CENTRAL ALABAMA

Except where reference is made to the work of others, the work described in this thesis is my own or was done in collaboration with my advisory committee. This thesis does not include proprietary or classified information.

Devi Bhagabati Prasad Udgata

Certificate of Approval:

Ashraf Uddin
Associate Professor
Geology

Charles E. Savrda, Chair
Professor
Geology

Willis E. Hames
Professor
Geology

Joe F. Pittman
Interim Dean
Graduate School

GLAUCONITE AS AN INDICATOR OF SEQUENCE STRATIGRAPHIC
PACKAGES IN A LOWER PALEOCENE PASSIVE-MARGIN
SHELF SUCCESSION, CENTRAL ALABAMA

Devi Bhagabati Prasad Udgata

A Thesis

Submitted to

the Graduate Faculty of

Auburn University

in partial fulfillment of the

Requirements for the

Degree of

Masters of Science

Auburn, Alabama
December 17, 2007

GLAUCONITE AS AN INDICATOR OF SEQUENCE STRATIGRAPHIC
PACKAGES IN A LOWER PALEOCENE PASSIVE-MARGIN
SHELF SUCCESSION, CENTRAL ALABAMA

Devi Bhagabati Prasad Udgata

Permission is granted to Auburn University to make copies of this thesis at its discretion, upon request of individuals or institutions and at their expenses. The author reserves all publication rights.

Signature of Author

Date of Graduation

VITA

Devi Bhagabati Prasad Udgata, son of Narayan Otta and Gouripriya Otta, was born on January 1, 1980, in a small village of the Orissa Province, in eastern India. He graduated from Katyayani High School, in Puri, India, in 1993. He attended Utkal University, in Bhubaneswar, India, and graduated in July 1998 with a Bachelors of Science degree in Geology. He attended the Indian School of Mines, Dhanbad, India, and graduated in May 2001 with a Masters of Science and Technology degree in Applied Geology. He entered the graduate program in Geology at Auburn University in the Fall of 2005.

THESIS ABSTRACT

GLAUCONITE AS AN INDICATOR OF SEQUENCE STRATIGRAPHIC
PACKAGES IN A LOWER PALEOCENE PASSIVE-MARGIN
SHELF SUCCESSION, CENTRAL ALABAMA

Devi Bhagabati Prasad Udgata

Master of Science, December 17, 2007
(M. Sc. Tech., Indian School of Mines, Dhanbad, India, 2001)

124 typed pages

Directed by Charles E. Savrda

The Lower Paleocene Clayton Formation in central Alabama comprises a complete third-order depositional sequence that accumulated mainly on a passive-margin marine shelf. Glauconite occurs throughout the sequence, providing the opportunity to systematically evaluate changes in glauconite abundance and character that resulted from sea-level-mediated fluctuations in sedimentation rates expressed at both the systems-tract and parasequence scale. To this end, detailed studies of glauconite were carried out using a combination of reflected and transmitted light microscopy, microprobe analyses, and x-ray diffraction studies.

Total glauconite abundance increases upward from lowstand systems tract (LST) incised valley-fill sands through the transgressive systems tract (TST) and condensed section (CS) and then generally decreases through the highstand systems tract (HST). Parasequences in the CS/HST are defined by asymmetrical cycles characterized by abrupt increases and gradual decreases in glauconite abundance. Although detrital glauconite is common in the LST and TST, most glauconite grains are authigenic. The relative abundances of various authigenic glauconite morphotypes vary with total glauconite content. Mature morphotypes (e.g., mammillated and lobate grains), as well as glauconitized skeletal grains and glauconite-coated detrital grains, are prevalent in the condensed section and lower parts of parasequences, while less mature varieties (e.g., vermicular grains) dominate parasequence tops. Decreases in glauconite maturity upward through parasequences also are indicated by lighter grain colors, decreasing K content, and increasing importance of glauconite smectite relative to glauconite mica.

Observations from this study indicate that glauconite can be an effective tool for delineating sequence stratigraphic packages and bounding surfaces, particularly in relatively sediment-starved, passive-margin shelf successions. Notably, in quiet-water shelf sequences, sea-level-controlled changes in glauconitization result in fining-upward parasequences.

ACKNOWLEDGMENTS

This study was supported by grants-in-aid of research from the Geological Society of America (GSA) and the Gulf Coast Association of Geological Societies (GCAGS). I am very much thankful to my research advisor Dr. Charles E. Savrda for his constant support, help, and advice. Thanks also due to my thesis committee members Dr. Ashraf Uddin, and Dr. Willis E. Hames for their support and encouragement. I thank Dr. Uddin for bringing me to Auburn University for a Master's Degree in Geology. Drs. Joey Shaw (Agronomy and Soils) and James Saunders (Geology and Geography) provided guidance in the preparation of samples for x-ray diffraction and microprobe analyses, respectively. Chris Fleisher facilitated microprobe analysis at the University of Georgia. Fellow graduate students Trent Hall, Sean Bingham, Mohammad Shamsudduha, Derick Unger, Prakash Dhakal, and Wahidur Rahman assisted in field or laboratory work. I dedicate my thesis to my family.

Journal style used: Palaios

Computer software used: Microsoft Word 2003, Microsoft Excel 2003, Microsoft PowerPoint 2003, Adobe Photoshop 7, Endnote 8

TABLE OF CONTENTS

LIST OF FIGURES	xii
LIST OF TABLES	xv
1.0 OBJECTIVES	1
2.0 GLAUCONITE.....	3
2.1 MINERALOGY	3
2.2 FORMATION OF GLAUCONITE	3
2.3 GRAIN FORMS AND FABRICS.....	4
2.4 GLAUCONITE MATURITY	5
2.4.1 Glauconite Chemistry and Color	6
2.4.2 Glauconite Morphology and Texture.....	11
2.5 USE OF GLAUCONITE IN SEQUENCE STRATIGRAPHY.....	12
2.5.1 Glauconite in Passive-Margin Depositional Sequences	12
2.5.2 Glauconite in Parasequence-Scale Studies	15
3.0 CLAYTON FORMATION.....	16
3.1 GENERAL STRATIGRAPHY	16
3.2 SEQUENCE STRATIGRAPHY	18
3.3 PALEOENVIRONMENT.....	20
4.0 LOCATION AND METHODS	22
4.1 STUDY LOCALITY	22
4.2 FIELD STUDIES	24

4.3 LABORATORY INVESTIGATIONS	25
4.3.1 Textural Analyses	25
4.3.2 Carbonate and Organic-Carbon Analyses	26
4.3.3 Binocular Microscopic Examination	26
4.3.4 Thin Section Petrography	26
4.3.5 X-Ray Diffraction Analyses	27
4.3.6 Electron Microprobe Analysis and Scanning Electron Microscopy	28
5.0 SEDIMENTOLOGICAL CHARACTER OF THE STUDY SECTION.....	30
5.1 GENERAL SECTION DESCRIPTIONS	30
5.1.1 Lowstand Incised Valley Fill (Unit 1, Clayton Sand)	30
5.1.2 Transgressive Lag (Unit 2)	35
5.1.3 Transgressive Systems Tract (Units 3-8)	35
5.1.4 Condensed Section (Units 9-11)	35
5.1.5 Highstand Systems Tract (Units 12-30)	37
5.2 TEXTURAL ANALYSES	38
5.3 CARBONATE AND ORGANIC CARBON ANALYSES	41
5.4 GENERAL PETROGRAPHY AND POINT-COUNT ANALYSES	47
5.4.1 General Observations	47
5.5 SUMMARY AND INTERPRETATION	54
6.0 CHARACTER OF GLAUCONITE	57
6.1 INTRODUCTION	57
6.2 MODES OF GLAUCONITE OCCURRENCE	57
6.2.1 Glauconite Morphotypes	57

6.2.2 Glauconite-Coated Grains.....	66
6.2.3 Glauconitized Skeletal Grains	71
6.2.4 Relationships to Systems Tracts and Parasequences	71
6.3 GLAUCONITE GRAIN COLOR	73
6.4 GLAUCONITE CHEMISTRY	74
6.5 XRD ANALYSIS	80
7.0 DISCUSSION	85
7.1 ROLE OF GLAUCONITE IN DELNEATING SEQUENCE STRATIGRAPHIC PACKAGES	85
7.2 COMPARISON WITH PREVIOUS PARASEQUENCE-SCALE STUDIES	86
7.3 COMPARISON WITH FORELAND BASIN PARASEQUENCES	87
7.4 ORIGIN OF CLAYTON LIMESTONES	87
8.0 CONCLUSIONS	89
REFERENCES	91
APPENDIX	97

LIST OF FIGURES

Figure 1 – The X-ray diffractogram peaks showing progressive stages of glauconitization (from Odin and Matter, 1981)	10
Figure 2 - Generalized shelf stratigraphic sequence showing systems tracts, bounding surfaces, and relations to sedimentation rate and authigenic glauconite content.	13
Figure 3 – Distribution of Lower Paleocene strata in Alabama	17
Figure 4 – Sequence stratigraphic interpretations of the Lower Paleocene Clayton Formation and enveloping strata, central Alabama	19
Figure 5 – Location of the Mussel Creek and Highway 263 sections (source: www.nationalgeographic.com/topo , 2002)	21
Figure 6 – Stratigraphic column of study section showing sequence stratigraphic context, informal units (1-30), and sampling horizons	31
Figure 7 – Photographs of the study section	32
Figure 8 – Photograph of unit 1 (Clayton sand) associated with underlying Prairie Bluff Chalk and overlying transgressive lag unit (unit 2).....	33
Figure 9 – Representative photomicrographs from the study section	34
Figure 10 – Representative photograph of carbonate cemented transgressive lag bed (unit 2) with phosphate clasts (P), and quartz pebbles (Q)	36
Figure 11 – Representative photograph of Clayton sand (unit 1), transgressive lag bed (unit 2), and overlying transgressive systems tract (units 3-8)	36
Figure 12 – Representative photographs of highstand systems tract	39
Figure 13 – Percent sand and mean grain size of sand in the study section	40
Figure 14 – Percent sand, carbonate and organic carbon in the study section	45
Figure 15 – General inverse relationship between percent carbonate and organic carbon.	46

Figure 16 – Percent sand, percent glauconite, and percent skeletal grains (including glauconitized grains) in the study section	50
Figure 17 – Percent glauconite vs. percent sand in the samples	52
Figure 18 – Relationship between percent carbonate and percent glauconite	52
Figure 19 – Relationship between percent sand, percent phosphate, and percent pyrite in the study section.....	53
Figure 20 – Stratigraphic column and inferred sea-level curves for the Clayton Formation	55
Figure 21 – Different grain morphotypes as viewed in reflected light.....	58
Figure 22 – Photomicrographs showing different glauconite grain types	60
Figure 23 – Backscattered electron images of different glauconite morphotypes	61
Figure 24 – Percent total glauconite, percent mammillated/lobate grains, and percent capsule-shaped grains in the study section	64
Figure 25 – Percent total glauconite, percent vermicular/tabular grains, and percent ovoidal grains in the study section	65
Figure 26 – Photomicrograph showing glauconite coatings on and fracture fillings in quartz (Q)	67
Figure 27 – Percent total glauconite, percent glauconite-coated detrital grains, and percent glauconitized skeletal grains in the study section	70
Figure 28 – Photomicrographs showing glauconitized fossil fragments	72
Figure 29 – Reflected light photographs showing color variation of glauconite grains in parasequences	75
Figure 30 – Plane-light photomicrographs showing color variation of glauconite grains in parasequences	76
Figure 31 – Relationships among average oxide contents for thirteen glauconite samples.....	78
Figure 32 – Percent sand, percent glauconite and K ₂ O % in the study section	79

Figure 33 – X-ray diffractograms derived from the parasequence 281

Figure 34 – X-ray diffractograms derived from the parasequence 482

Figure 35 – X-ray diffractograms of samples from unit 9 (condensed section; base of parasequence 2) and unit 19 (middle of parasequence 4)83

LIST OF TABLES

Table 1 – Morphological varieties of glauconite	6
Table 2 – Internal fabrics within glauconite grains	7
Table 3 – Characteristics of glauconite at different stages of maturity	8
Table 4 – Percent sand, mean sand size, and percent carbonate and organic carbon data.	42
Table 5 – Relative abundance of grain types based on point-counts of selected samples from the study section.....	48
Table 6 – Normalized percentages of assignable glauconite grain types derived from point-count data	62
Table 7 – Abundances of glauconitized skeletal grains and glauconite-coated detrital grains based on point-count analysis	68
Table 8 – Average abundances (weight percent) of major oxides in glauconite grains as determined by microprobe analysis	77
Table TA1 - Abundances (weight percent) of major oxides in glauconite grains as determined by microprobe analysis	97

1.0 OBJECTIVES

The term “glaucinite,” derived from the Greek word *glaukos* for “blue-green,” is used to collectively refer to a broad spectrum of minerals that fall within what is known as the “glaucinity facies.” According to Odin and Matter (1981), the glaucinity facies includes dark green to greenish brown grains that fall within the spectrum between immature ‘glaucinitic smectite’ and mature ‘glaucinitic mica’ end members. Glaucinite, or glaucinity, is an authigenic component that forms via replacement of, or precipitation on or within, existing grains (mainly fecal pellets, shells or tests, or phyllosilicate grains) within marine sediments. Formation of glaucinite is generally restricted to marine environments wherein supply of iron (Fe) is high, conditions are suboxic, and, most important, sediment influx is very low (McRae, 1972; Odin and Matter, 1981).

Because glaucinite is a sensitive indicator of low sedimentation rate, it constitutes a powerful tool for sedimentological interpretation of glaucinite-bearing marine successions (Amorosi, 1997). By reflecting the residence time of grains at or near the seafloor, the presence and compositional maturity of glaucinite can help recognize and assess the magnitude of relative breaks in sedimentation (Odin and Matter, 1981; Amorosi, 1995). This is particularly important for sequence stratigraphic studies. Given its link to sediment starvation, authigenic glaucinite traditionally has been taken as an indicator of transgressive systems tracts and condensed sections (Van Wagoner et al., 1988). Recent studies of glaucinite in a sequence stratigraphic framework (e.g., Amorosi,

1995; Harris and Whiting, 2000; Hesselbo and Hugget, 2001) show that glauconite may be present in almost all systems tracts, but its maturity may vary systematically from one systems tract to another. Glauconite also potentially could be used to study shorter-term relative sea-level changes reflected at the parasequence scale. However, studies of glauconite at the parasequence level are rare (Amorosi, 1995; Urash, 2005).

The objective of this thesis research is to test two related hypotheses: (1) abundance and maturity of glauconite vary systematically through a depositional sequence in response to sea-level dynamics and associated changes in sedimentation rate; and (2) abundance and maturity of glauconite vary systematically through individual parasequences in response to shorter-term changes in relative sea level. These hypotheses were evaluated through a detailed study of glauconite and other sedimentary parameters in the Lower Paleocene Clayton Formation exposed along Mussel Creek and nearby roadcuts in Lowndes County, central Alabama.

2.0 GLAUCONITE

2.1 Mineralogy

Minerals placed into the glauconite group are iron- and potassium-rich aluminophyllosilicates having the general chemical composition of $(K, Na) (Fe, Al, Mg)_2 (Si, Al)_4 O_{10} (OH)_2$. These minerals constitute a continuous family with smectite and micaceous end members (Odin and Fullagar, 1988). Glauconite mica is a Fe- and K-rich dioctahedral mica with tetrahedral Al (or Fe^{3+}) usually comprising >0.2 atoms per formula unit and octahedral R^{3+} comprising >1.2 atoms (Huggett, 2005). Typically, 5–12% of the total iron is ferrous. Glauconite mica is chemically distinguished from ferric illite by having higher total iron content, and from celadonite by higher levels of substitution of aluminum for silicon in the tetrahedral layer and by a higher octahedral charge (Duplay and Buatier, 1990). Glauconitic-smectite is a mixed-layer clay that has lower K and Fe contents but higher Al contents than glauconite mica. As will be described in subsequent sections, the spectrum of glauconite smectite to glauconite mica reflects mineralogic maturity (Thompson and Hower, 1975; Odin and Matter, 1981; Odin and Fullagar, 1988).

2.2 Formation of Glauconite

The formation of glauconite occurs via authigenesis under a relatively narrow range of environmental conditions. It forms at or near the sediment-water interface in oxygenated to mildly reducing marine environments wherein sedimentation rates are very

low (McRae, 1972; Odin and Matter, 1981; Amorosi, 1997). Glauconization mainly occurs in fine-grained muds deposited in shelf and slope settings at depths between 30 m to 500 m (Bornhold and Giresse, 1985; Amorosi, 1997; Kelly and Webb, 1999).

Glauconite may precipitate as coatings or films on the walls of fissures, borings, and other semi-confined microenvironments associated with carbonate hardgrounds (Pemberton et al., 1992; Kitamura, 1998; Ruffel and Wach, 1998). However, it forms most commonly in granular siliciclastic substrates via replacement, infilling, or coating of individual grains. Fecal pellets are the most common type of precursor substrate. Aggregation of clay-rich sediment during passage through the digestive tracts of the organisms creates microenvironments that are favorable for glauconitization (Anderson et al., 1958; Pryor, 1975; Chafetz and Reid, 2000). In addition to pellets, glauconite may replace a variety of other grain types, including micas, quartz, chert, feldspar, calcite, dolomite, phosphate, and volcanic rock fragments (McRae, 1972; Pryor, 1975; Odin and Matter, 1981). Glauconite also may precipitate as cements within microfossil cavities or as coatings or films on other grains (Triplehorn, 1966; McRae, 1972; Odin and Matter, 1981).

2.3 Grain Forms and Fabrics

Glauconite mainly occurs in the form of sand-sized grains in the range of 100-500 μm (McRae, 1972). Grains typically exhibit an earthy or lustrous appearance (Odin and Matter, 1981; Odin and Morton, 1988; Kelly and Webb, 1999). Morphology of these grains varies considerably with regard to size, gross shape, and surface characteristics (grain smoothness, external ornamentation, and fractures). Based on these attributes, Triplehorn (1966) identified nine morphological varieties: (1) spheroidal or ovoidal

pellets; (2) tabular or discoidal pellets; (3) mammilated pellets; (4) lobate pellets; (5) capsule-shaped pellets; (6) composite pellets; (7) vermicular grains; (8) fossil casts and internal molds; and (9) pigmentary glauconite. Defining characteristics of these varieties, summarized in Table 1, reflect to varying degrees the morphology of the precursor grain and the compositional maturity of the glauconite.

The internal textures and fabrics of glauconite grains, as viewed in cross-sections of broken grains or in thin section, are also variable. Previous workers (Triplehorn, 1966; McRae, 1972) have employed a variety of terms to describe internal fabrics (Table 2). Most fabrics (e.g., micaceous or vermicular fabrics) reflect the structure of replaced precursor grains, while others reflect formation of glauconite as a primary precipitate.

2.4 Glauconite Maturity

Odin and Matter (1981) recognized four common varieties of glauconite that reflect different levels of maturation: nascent, slightly evolved, evolved, and highly evolved grains. Level of maturity reached by glauconite depends on residence time of grains at or near the sediment-water interface and, hence, sedimentation rate. The glauconitization process normally ceases after burial beneath several decimeters of sediment, and formation of fully mature grains may require residence times of 10^5 - 10^6 years (Odin and Matter, 1981). Levels of maturity of glauconite can be assessed based on chemical composition, grain color, and morphology (Table 3).

2.4.1 Glauconite Chemistry and Color

The formation of glauconite begins at the sediment-water interface with the development of iron-rich smectitic clay (nascent glauconite). As the glauconitization process proceeds, grains progressively alter towards the glauconite mica end member

Table 1 – Morphological varieties of glauconite (after Triplehorn, 1966).

Glauconite Variety	Characteristics
<i>spheroidal or ovoidal pellets</i>	simple, rounded, equidimensional grains with smooth surfaces
<i>tabular or discoidal pellets</i>	flattened, elongate or disk- or bowl-shaped pellets
<i>mammilated pellets</i>	irregular grains with small rounded knobs separated by shallow sutures
<i>lobate pellets</i>	very irregular grains with deep radial cracks; commonly triangular in cross-section
<i>capsule-shaped pellets</i>	simple cylindrical grains with nearly circular cross-sections
<i>composite pellets</i>	relatively large (up to 3-4 mm) grains composed of smaller grains of glauconite and detrital minerals embedded in glauconitic matrix
<i>vermicular grains</i>	accordion-shaped grains; also known as caterpillar, zebra, concertina, accordion, or booklet grains
<i>fossil casts and internal molds</i>	shapes correspond to skeletal fragments or internal molds (e.g., foraminiferal tests, sponge spicules, echinoderm spines, etc.)
<i>pigmentary glauconite</i>	coatings on surfaces of and/or penetrating cracks/cleavage within other minerals

Table 2 – Internal fabrics within glauconite grains (after Triplehorn, 1966; McRae, 1972).

Fabrics	Characteristics
<i>random microcrystalline</i>	homogeneous aggregates of overlapping micaceous flakes with no preferred orientation
<i>oriented microcrystalline</i>	lamellar aggregates of oriented microcrystals (exhibit unit extinction in polarized light)
<i>micaceous or vermicular</i>	similar to oriented microcrystalline fabrics but with incipient micaceous cleavage
<i>coatings on grains</i>	accretionary, oolitic textures
<i>organic replacement structures</i>	various fibrous, perforate, or lamellar structures reflecting the internal structure of replaced or infilled skeletal grains
<i>fibroradiated rims</i>	rims, differing in color and structure from core grains, formed by accumulation or precipitation (rather than alteration)

Table 3 – Characteristics of glauconite at different stages of maturity (after Odin and Matter, 1981; Amouric and Parron, 1985; Amorosi, 1995; Huggett and Gale, 1997; Kelly and Web, 1999).

Glauconite types	Maturity	K₂O content	Mineralogical structure	Color	XRD peak position
<i>nascent</i>	low	< 4%	glauconite smectite	pale green	14 Å
<i>slightly evolved</i>	moderate	4-6%	↓	light green	↓
<i>evolved</i>	high	6-8%		green	
<i>highly evolved</i>	very high	> 8%		glauconite mica	

(highly evolved grains). This maturation process involves the uptake of Fe at the expense of Al and the uptake of K in lattice spaces to balance the remaining charge (McRae, 1972; Odin and Matter, 1981). Hence, level of maturation can be assessed based on mineral chemistry and associated mineral structure.

Potassium (K) content, measured via microprobe analysis or other technique, is most commonly employed to evaluate compositional maturity of glauconite. Nascent, slightly evolved, evolved, and highly evolved stages generally are indicated by K₂O contents of 2-4%, 4-6%, 6-8%, and >8%, respectively (Birch et al., 1976; Odin and Matter, 1981; Amorosi, 1995) (Table 3). K₂O contents of ~7% or more generally are indicative of significant breaks in deposition (McRae, 1972; Odin and Matter, 1981; Odin and Fullagar, 1988; Chafetz and Reid, 2000). Chemical changes are accompanied by structural changes that can be recognized in x-ray diffraction analysis. Increases in glauconitic maturity are accompanied by a progressive shift from a glauconite smectite peak at ~14 Å to a glauconite mica peak at 10 Å (Table 3, Fig. 1) (Odin and Matter, 1981; Amouric and Parron, 1985; Amorosi, 1995; Huggett and Gale, 1997; Kelly and Web, 1999).

Glauconite is generally greenish, as viewed under normal reflected light and in thin section under plane-polarized light (McRae, 1972). However, grain color does vary with degree of maturation (Table 3). Nascent grains are typically brownish, light green to pale greenish-yellow, slightly evolved grains are normally olive green, and evolved and highly evolved grains range from dark green to almost black (McRae, 1972; Odin and Matter, 1981; Amorosi, 1995). The progressive darkening of grains reflects increasing

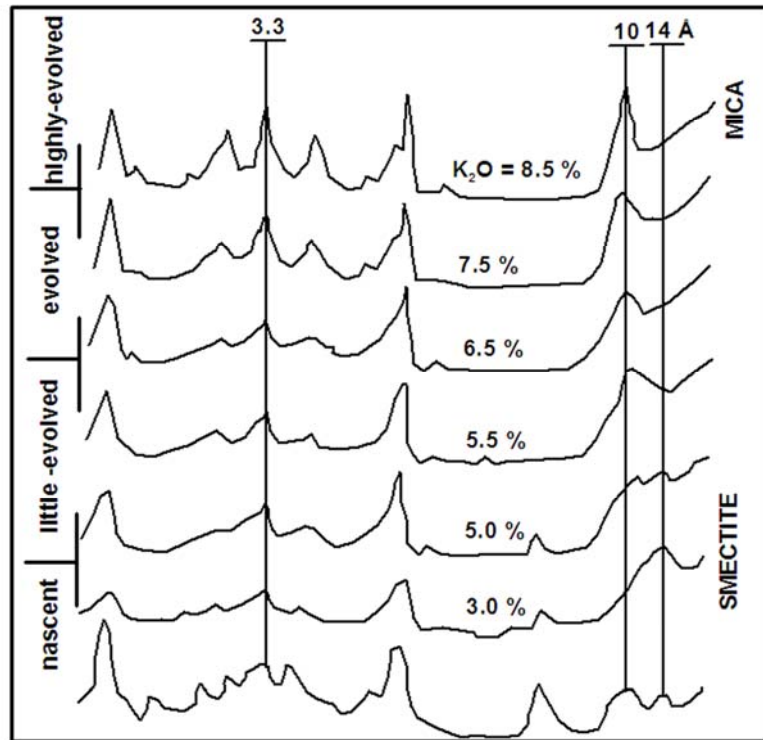


Figure 1 – The X-ray diffractogram peaks showing progressive stages of glauconitization (from Odin and Matter, 1981).

ferrous Fe contents. Where weathering has occurred and glauconite is oxidized to kaolinite and/or goethite, grains become rusty brown.

2.4.2 Glauconite Morphology and Texture

Various attempts have been made to link glauconite grain morphology to level of maturity. Nascent, weakly evolved grains generally retain the original size, shape, and texture of the host grain that has been replaced. With increased maturity, the shape and affinity of host grains may be masked (Odin and Matter, 1981). Of the morphological varieties listed in Table 1, mammillated, capsule-shaped, lobate, and vermicular grains are typically considered as relatively mature grain types, particularly if they exhibit marginal fractures and cracks (Odin and Matter, 1981; Odin and Fullagar, 1988; Amorosi, 1995, 1997). Cracks in glauconite, which are typically irregular and taper inward, are thought to form due to differential expansion during mineral growth (McRae, 1972; Odin and Morton, 1988; Huggett and Gale, 1997; Kelly and Web, 1999) or dehydration during the mineralogical evolution of the grains (McRae, 1972). Precipitation of glauconite within grain cracks and fractures is generally indicative of the highly evolved stage (Odin and Matter, 1981).

Huggett and Gale (1997) have suggested that grains with vermicular fabrics are less evolved than grains with fractures and/or healed fractures. They argue that the vermicular fabric is inherited from precursor grains (e.g., fecal pellets, micas), and that this fabric would be lost with further grain evolution during maturation. In contrast to other workers (Odin and Matter, 1981; Odin and Fullagar, 1988; Amorosi, 1995, 1997), Huggett and Gale (1997) also suggest that ovoidal pellets are more mature than the other morphological varieties.

Use of glauconite grain morphology to assess maturity may be complicated by grain transport and reworking. Cracks in grains represent zones of weakness. Hence, mature fractured grains are vulnerable to mechanical breakdown, during physical transport or bioturbation, into smaller, less irregular fragments. Further abrasion of these fragments can result in ovoidal or spherical grains (Amorosi, 1997). Such grains, known as *detrital* glauconite, are less reliable for evaluating maturity and, because they are transported, may not reflect the authigenic conditions that existed during deposition of the host sediment (McRae, 1972; Odin and Matter, 1981; Odin and Fullagar, 1988; Amorosi, 1997).

2.5 Use of Glauconite in Sequence Stratigraphy

2.5.1 Glauconite in Passive-Margin Depositional Sequences

Glauconite formation and maturation require prolonged residence at or near the sediment-water interface and, hence, are reliable indicators of low sedimentation rate (Odin and Matter, 1981; Odin and Fullagar, 1988; Amorosi, 1995). For this reason, occurrences of abundant glauconite have traditionally been interpreted to reflect marine transgression and associated sediment starvation (Odin and Matter, 1981; Baum and Vail, 1988; Odin and Fullagar, 1988; Amorosi, 1995, 1997). The link between glauconite and sedimentation rate gained significance with the development of sequence stratigraphy (Baum and Vail, 1988; Posamentier et al., 1988; Van Wagoner et al., 1988). Depositional sequences consist of systems tracts that correspond to distinct phases of sea-level cycles, and these phases govern sedimentation rates (Fig. 2).

Recent studies focusing on passive-margin successions have shown that glauconite may be ubiquitous throughout a depositional sequence, but its origins

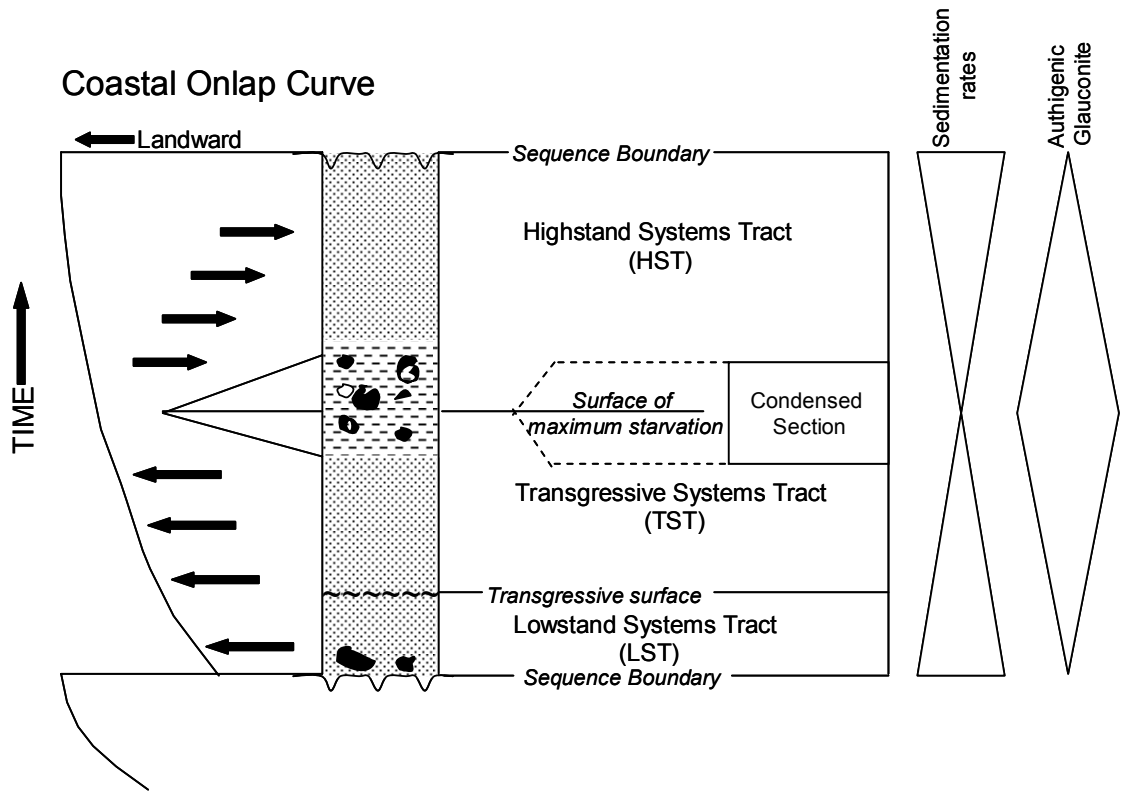


Figure 2 – Generalized shelf stratigraphic sequence showing systems tracts, bounding surfaces, and relations to sedimentation rate and authigenic glauconite content.

(authigenic vs. detrital), abundance, and maturity vary systematically within and through systems tracts (Amorosi, 1995, 1997; Huggett and Gale, 1997; Kelly and Web, 1999; Harris and Whiting, 2000; Giresse and Weiwióra, 2001; Hesselbo and Huggett, 2001). In marine shelf sequences, lowstand systems tracts (LST) normally consist of sediments that were deposited relatively rapidly in estuarine, lagoonal, or foreshore-shoreface settings wherein conditions are not favorable for glauconitization. Nonetheless, due to the erosion of older glauconitic deposits, lowstand sediments (e.g., incised valley fills) may contain detrital glauconitic grains (Baum and Vail, 1988).

Transgressive systems tracts (TST) form during phases of sea-level rise and diminished sediment influx. TST deposits typically contain detrital glauconite, particularly near the base of the systems tract (e.g., in association with transgressive lags on the transgressive surface, TS) and common to abundant authigenic glauconite. Abundance and maturity of authigenic glauconite in TST deposits vary as a function of specific deposition environments, shorter-term sea-level dynamics, and magnitude of sediment starvation but generally increase upwards through the system tract (Bhattacharya and Walker, 1991).

Maximum glauconite abundances and maturity are characteristic of the condensed section (CS) and the associated surface of maximum sediment starvation (SMS), which occur at the transition between the TST and the highstand systems tract (HST). In passive-margin condensed sections, glauconite is commonly associated with concentrations of fossil debris, phosphatic grains, sulphides, carbonates horizons, and intense bioturbation (Baum and Vail, 1988; Pemberton et al., 1992; Amorosi, 1995; Kitamura, 1998; Urash, 2005).

Vertical successions within highstand systems tracts (HST) generally reflect increasing sedimentation rates associated with late transgressive, highstand, and early regressive phases. Authigenic glauconite may be most common in the lower parts of the HST. However, glauconite abundance and maturity generally decrease upward through this systems tract. Authigenic glauconite is typically rare or absent in the upper part of the HST.

2.5.2 Glauconite in Parasequence-Scale Studies

Parasequences are the building blocks of systems tracts. Parasequences and parasequence sets are relatively conformable successions of genetically related beds or bedsets that reflect shorter-term sea-level changes. In marine depositional sequences, they are upward-shallowing sediment packages bounded by marine-flooding surfaces (Van Wagoner et al., 1988). Previous investigations of glauconite at the parasequence scale are relatively rare, but indicate that abundance and maturity of authigenic glauconite may decrease upward through parasequences in response to sea-level mediated increases in sedimentation rate (Amorosi, 1995; Urash, 2005). The Lower Paleocene Clayton Formation in central Alabama provides the opportunity to further explore the relationships between glauconite and sea-level dynamics at both the systems tract and parasequence scales.

3.0 CLAYTON FORMATION

3.1 General Stratigraphy

The Paleocene (Danian) Clayton Formation, part of the Midway Group, crops out in an arcuate belt trending northwest-southeast across Alabama (Fig. 3A, B) and adjacent states. Strata dip gently to the south and southwest at less 30-40 ft/mile (0.6-0.8°). The Clayton Formation overlies the Cretaceous (Maastrichtian) Prairie Bluff Chalk in western Alabama and the Providence Sand in eastern Alabama, and is overlain by the Paleocene Porters Creek Formation (Baum and Vail, 1988; Donovan et al., 1988).

The basal contact of Clayton Formation (the Cretaceous-Tertiary boundary) is a regional unconformity. At some localities, this unconformity is overlain by a lag bed of quartz grains, phosphate pebbles, and shark teeth. In central and western Alabama, the unconformity is locally overlain by thin, discontinuous lenses of quartzose fine- to coarse-grained sands (e.g., at Moscow Landing, along Shell Creek, at Prairie Bluff Landing, and along Mussel Creek) (Mancini et al., 1989, 1993; Savrda, 1993). The latter sand bodies, which contain Tertiary macrofossils and reworked Cretaceous microfossils, are known collectively as the Clayton basal sands (LaMoreaux and Toulmin, 1959). Locally, the sands fill depressions on the eroded surface of the underlying chalk (Mancini et al., 1989; Mancini and Tew, 1993).

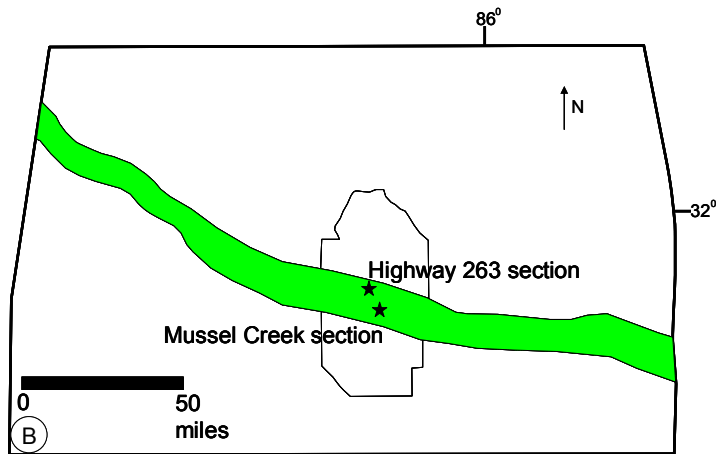
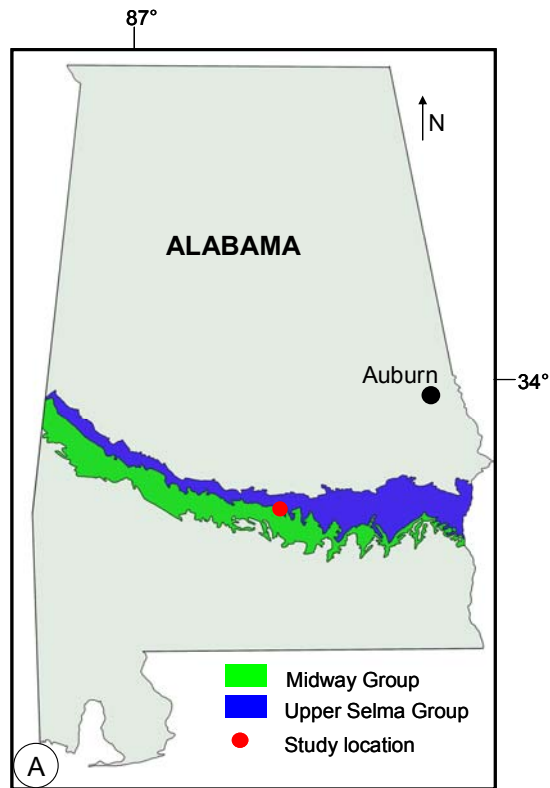


Figure 3 – Distribution of Lower Paleocene strata in Alabama. (A) Map showing the location of the study area and distribution of Cretaceous Upper Selma Group and Lower Paleocene Midway Group in Alabama. (B) Generalized map showing the distribution of Clayton Formation in southern Alabama, and study locations (stars) in Butler and Lowndes Counties.

The thickness and lithologic character of the Clayton Formation vary along the outcrop belt (Baum and Vail, 1988; Donovan et al., 1988; Mancini et al., 1989; Mancini and Tew, 1993). In the far eastern and far western parts of Alabama, the Clayton Formation is relatively thin and is not differentiated into members. In central Alabama, including the area of the current study, the Clayton Formation is relatively thick (up to 60 m) and is divided into two members; the Pine Barren and McBryde members (Fig. 4). The lower Pine Barren Member includes, in ascending order: the localized Clayton sands; a thin (~2.5 m) package of alternating glauconitic calcareous muddy sands and sandy limestones; a thicker package of alternating sandy, calcareous mudstones and fine-grained limestones and marls; and a very fossiliferous sandy limestone (informally known as the “*Turritella* Rock”) (Mancini et al., 1989). The McBryde Member, also known informally as the “*Nautilus* Rock,” consists of light gray to white, sandy, argillaceous limestones (Smith et al., 1894).

3.2 Sequence Stratigraphy

According to previous workers, the Clayton Formation contains parts of two marine shelf depositional sequences and, hence, records two sea-level cycles (Fig. 4) (Baum and Vail, 1988; Donovan et al., 1988; Mancini et al., 1989). The contact between the Clayton Formation and the underlying Prairie Bluff Chalk (or Providence Sand) generally is regarded as a sequence boundary that separates the uppermost Cretaceous depositional sequence UZAGC- 5.0 from the lowermost Paleocene depositional sequence TP 1.1 (Baum and Vail, 1988; Donovan et al., 1988; Mancini and Tew, 1988, 1993; Mancini et al., 1989, 1995; Savrda, 1991, 1993).

Period	Age	Relative Changes in Coastal Onlap		Lithostratigraphy		Systems Tracts
		Landward	Seaward			
Tertiary	Danian	TP1.2		Porters Creek Formation		highstand
				McBryde Member	Clayton	condensed section
				"Turritella Rock"		transgressive
		TP1.1			Clayton	shelf margin
				Pine Barren Member	Formation	highstand
				Clayton sands		condensed section
Cretaceous	Maastrichtian	UZAGC-5.0				highstand
						condensed section
						transgressive

Figure 4 – Sequence stratigraphic interpretations of the Lower Paleocene Clayton Formation and enveloping strata, central Alabama, (light gray area indicates the depositional sequence studied herein). Black triangles indicate condensed sections. SB- Sequence Boundary; UZAGC 5.0, TP 1.1, and TP 1.2 represent Upper Cretaceous and Lower Paleocene depositional sequences, respectively. Lower two sequence boundaries are type 1, while upper sequence is type 2, (after Mancini et al., 1989).

Sequence TP 1.1 includes all of the Pine Barren Member except for the *Turritella* Rock. The thin Clayton sand bodies have been interpreted as lowstand incised-valley fill deposits, although some of these sand bodies have been attributed to deposition in response to a K-T boundary impact event and associated megawave processes (Bourgeois et al., 1988; Hildebrand et al., 1991). Where the Clayton sands are absent, the basal Clayton contact is inferred to represent a coplanar sequence boundary/transgressive surface (SB/TS). Coarse-grained, fossiliferous, phosphatic, quartzose beds that immediately overlie the Clayton sand or the coplanar SB/TS are inferred to be transgressive lag deposits. Alternating glauconitic calcareous muddy sands and sandy limestones in lower parts of the Pine Barren Member are assigned to the transgressive systems tract/condensed section. The overlying package of calcareous sandy muds and fine limestones has been placed into the highstand systems tract. Decimeter- to meter-scale beds or bedsets in both transgressive and highstand deposits of sequence TP1.1 have been interpreted as parasequences formed in response to short-term changes in relative sea level (Huchison, 1993).

The remainder of the Clayton Formation has been assigned to depositional sequence TP1.2. The base of the *Turritella* Rock is interpreted as a sequence boundary. The *Turritella* Rock, McBryde Member, and Porters Creek Formation represent lowstand, transgressive, and highstand deposits, respectively.

3.3 Paleoenvironment

Strata of the Clayton Formation are interpreted to have been deposited in marginal marine and shallow marine settings (Mancini et al., 1989). Although some Clayton sand bodies are inferred to be impact-related tsunami deposits (e.g., Smit et al., 1996), the

Clayton sand in the study area likely was deposited in estuarine settings during an early stage of transgression (Habib et al., 1992; Savrda, 1993). The bulk of the Clayton Formation (Pine Barren and McBryde members) was deposited in passive-margin marine shelf settings under variable water depths and energy regimes controlled by sea-level dynamics and distance to the paleo-shoreline. As a generalization, deposits exposed in the eastern and western portions of the Clayton outcrop belt in Alabama represent relatively shallow and deeper shelf facies, respectively (Huchison and Savrda, 1994)

4.0 LOCATION AND METHODS

4.1 Study Locality

This study concentrated on exposures of the Pine Barren Member of the Clayton Formation in southern Lowndes County, central Alabama (Figs. 3A and B). The work focused on a relatively continuous section exposed in the banks of Mussel Creek and within immediately adjacent road cuts created during construction of a new bridge over the creek. However, supplementary observations and sampling were made at an equivalent section exposed a few miles north of the Mussel Creek locality along Highway 263 (Fig. 5).

Selected exposures were ideal for this study for several reasons. First, they include a relatively complete section of the Pine Barren Member for which the sequence stratigraphic context has already been established. Based on previous investigations (Baum and Vail, 1988; Donovan et al., 1988; Mancini and Tew, 1988; Mancini et al., 1989; Savrda, 1991), these exposures include, in ascending order: highstand marls (upper 4 m of Maastrichtian Prairie Bluff Chalk) of sequence UZAGC-5.0; the basal TP 1.1 sequence boundary locally separated from a transgressive (ravinement) surface by alleged lowstand estuarine incised valley-fill deposits (<1 m thick Paleocene Clayton sands); a thin (~ 2.5 m) transgressive systems tract dominated by glauconitic sandy limestones, marls, and marly sands; a purported surface of maximum starvation; and highstand

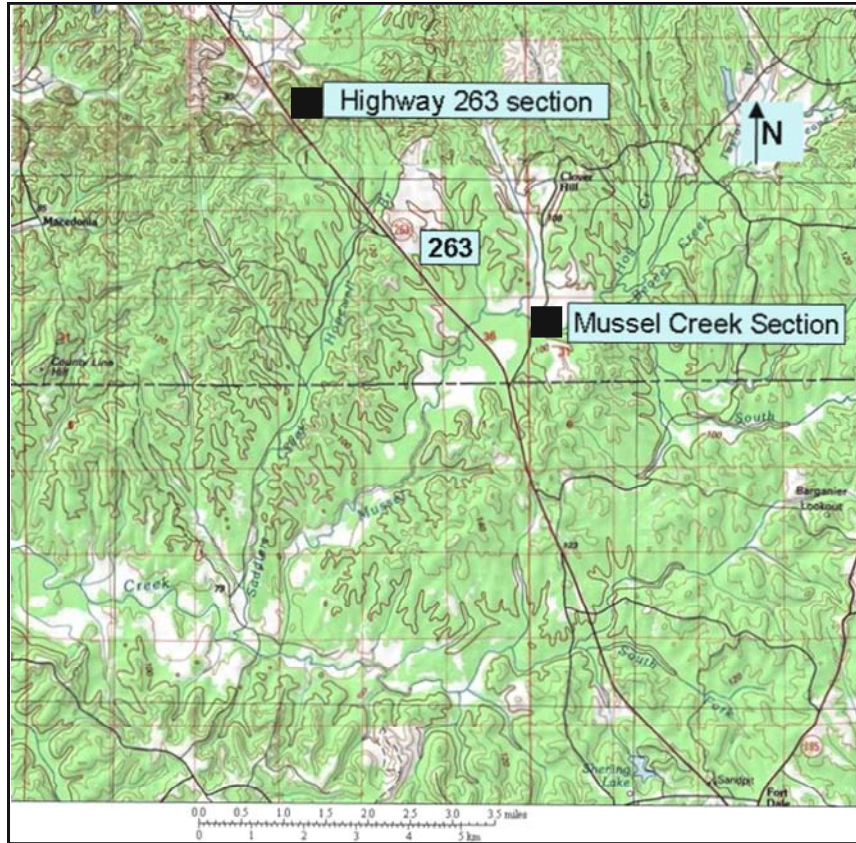


Figure 5 – Location of the Mussel Creek and Highway 263 sections (source: www.nationalgeographic.com/topo, 2002).

deposits (~ 8 m) dominated by alternating calcareous muds and muddy limestones. Both transgressive and highstand deposits in sequence TP1.1 are characterized by decimeter- to meter-scale beds or bedsets that have been interpreted as parasequences formed in response to short-term changes in relative sea level (Mancini and Tew, 1993; Huchison and Savrda, 1994). Second, glauconite is present throughout the section, providing an opportunity to examine variations in the abundance and character of glauconite through a depositional sequence and associated parasequences. Finally, the exposures are virtually complete and relatively unweathered. Only one interval of the section at Mussel Creek was weathered deeply enough to require supplementary sampling from Highway 263 road-cut exposures.

4.2 Field Studies

Field studies involved section description and collection of samples. The Mussel Creek section was carefully measured and described using Jacob staff, tape, and line-level methods. Observations focused on general lithology and sedimentary structures, but included associated body and trace fossils. A total of 30 units were delineated in the Pine Barren Member of the Clayton Formation; one representing the lowstand incised valley fill (unit 1; Clayton sand), twelve in the transgressive systems tract (units 2-11; including a transgressive lag and condensed bed), and seventeen in the highstand systems tract (units 12-30). Sedimentologic characteristics observed in the field were employed in the preliminary delineation of parasequences.

A total of 110 samples were collected throughout the section for laboratory analyses. Generally, only one or two samples were collected from thinner, commonly indurated beds. For thicker typically less indurated beds, multiple samples were collected

in series throughout the beds. Vertical spacing of samples was variable but averaged ~10 cm. One ~1.5-m-thick interval of the Mussel Creek section (unit 13) was deeply weathered and oxidized. Hence, samples for this unit were derived from an unweathered outcrop along Highway 263.

4.3 Laboratory Investigations

Sediment samples were subjected to various analyses in the laboratory. These included general analyses of sediment texture and composition (including carbonate and organic carbon contents) and petrographic, XRD, and microprobe studies of glauconite.

4.3.1 Textural Analyses

Sediment textures for all samples were determined using a combination of wet- and dry-sieve techniques. A small subsample (~25 g) of each sediment sample was dried, weighed and disaggregated. Most of the subsamples (muddy sands, sandy muds) could be disaggregated in distilled water. However, disaggregation of more indurated carbonate-rich subsamples required digestion in 10% HCl. Subsamples (or insoluble residues) were then wet-sieved through a 4 Φ (63-micron) screen to remove the mud (silt and clay) fraction. The sand-sized fraction was removed from the screen, dried, weighed, and then dry-sieved (using a Gilson screen shaker) for 15 minutes at 1 Φ intervals through the range of 0 Φ (1 mm) to 4 Φ (63 μ). Each size fraction was weighed and retained for latter inspection. Sand content (% sand) was determined by weight loss during wet-sieve and acid digestion procedures. Graphic mean size of the sand fractions was calculated using the GRADISTAT program (Blott, 2000) following Folk and Ward (1957).

4.3.2 Carbonate and Organic-Carbon Analyses

Carbonate and organic-carbon contents were determined using acid digestion and a LECO CS-200 carbon/sulfur analyzer, respectively. Subsamples weighing ~3-4 g were extracted from each of the field samples, powdered, and then dried for 24 hours. Approximately 0.25 g of the powdered subsamples were weighed and digested in 10% HCl. Residues were filtered through pre-weighed carbon-free borosilicate filters. The filters and residues were then dried for 24 hours and weighed. Carbonate contents of subsamples were determined by weight loss during acid digestion. Dried filters and residues were then combusted with metal accelerators in a LECO CS-200 carbon/sulfur analyzer. Organic carbon content (wt %) was determined by infrared detection of CO₂ released during sample combustion.

4.3.3 Binocular Microscopic Examination

Sand fractions derived from subsample sieving were examined under a binocular microscope. Examination focused on grains contained within the mean sand size range for each sample. The mean grain-size fraction was used to visually estimate the relative abundance of glauconite in each sample, to identify and describe the glauconite grain morphologies, and to qualitatively assess glauconite color.

4.3.4 Thin Section Petrography

A total of 110 thin sections, representative of all samples collected in the field, were prepared for petrographic analyses. Thin sections were prepared commercially by Wagner Petrographic Laboratory. Thin sections were initially examined under a petrographic microscope to recognize and generally describe sediment textures and various components, including clastic or detrital grains (e.g., quartz, feldspars, micas),

allochemical grains (e.g., skeletal fragments), matrix and cements, and glauconite (color, morphotypes, etc.). Representative fabrics, textures, and grain types were documented via digital photography.

Following general petrographic studies of all thin sections, a total of sixty-one representative thin sections were subject to point-count analysis in order to quantify the relative abundances of major detrital and authigenic constituents, including various glauconite types. A total of 300 grains were counted per thin section. Point counting was performed at 50X magnification with the aid of an automatic point-counting stage.

4.3.5 X-Ray Diffraction Analyses

Owing to time and cost constraints, only eight samples were selected for X-ray diffraction (XRD) analyses. Grains were extracted from the mean sand fraction of these samples, wherein glauconite grains were abundant. Grains were powdered using a mortar and pestle. Powders were then used to prepare oriented samples using the filter-membrane peel technique (Drever, 1973, as cited by Moore and Reynolds, 1989, 1997). Approximately 150 mg of powder were suspended in water and filtered under vacuum through carbon-free borosilicate filters. After the water was removed, three separate 5-ml aliquots of a cation-saturating solution [MgCl_2 of 0.5 M (1N)] were filtered through the sample. The sample was then filter washed several times with 5-ml aliquots of deionized water to remove the extra salts from the sample. After completion of the saturation process, samples were allowed to dry to a moist state. The filter paper was then placed with the sediment face down on a clean, ethanol-washed glass slide. Air bubbles between the filter paper and the glass slide were removed by rolling a plastic cylinder across the

filter paper. The filter paper was then gently peeled away, leaving the oriented sample on the glass slide.

Oriented mounts were sprayed with ethylene glycol and placed into a Siemens D 5000 x-ray diffractometer housed in the Department of Agronomy and Soils at Auburn University. Samples were run using a Cu K α radiation source at a speed of 0.05°/3 s. through the range of 0 to 60° 2 θ . X-ray diffractograms were used to evaluate the structural states of glauconites (i.e., within the glauconite smectite-glauconite mica spectrum).

4.3.6 Electron Microprobe Analysis and Scanning Electron Microscopy

As with XRD analysis, time and cost limited the number of samples that were subject to electron microprobe analysis (EMPA). A total of thirteen samples were strategically selected. Glauconite grains were manually picked from the sand-sized fractions of these samples, mixed with an embedding medium (epoxy resin), and set in a plastic cylindrical mold. After the epoxy set, lower portions of the molds were hand polished with 600 to 1000 grit to expose grains for microprobe analysis.

EMPA of polished sections were performed using the microprobe facility in the Department of Geology at the University of Georgia (Athens, GA). Specifically, analyses were performed using a JEOL 8600 Scanning Electron Microprobe fitted with wavelength-dispersive spectrometer (WDS). Analyses were run at an accelerating voltage of 10 KeV, with a 10 nA (nano-ampere) current flowing for 10 seconds and a fixed beam diameter of 10 μ m. A Phi-Rho-Z metric correction was used.

Samples were pre-coated with carbon using the evaporated carbon-coating method to make the samples conductive. Before selecting individual points for EMPA,

grains were examined using backscattered-electron (BSE) imagery to recognize primary and secondary glauconite infillings and compositional variations within single grains. Only primary glauconitic parts of grains (those having higher atomic number and brighter parts in BSE images) were selected for EMPA.

Ten grains per sample were analyzed to evaluate major element abundances. Data for the 10-grain sets were used to calculate average compositions for each sample. K, Fe, and Al were the major elements of interest. Natural and synthetic mineral standards were used to calculate $K_2O\%$. Orthoclase was used as the primary standard, and lemhi biotite prepared by USGS was used as secondary standard. Total oxygen content was measured by the stoichiometry method, and total Fe% was measured as FeO.

5. 0 SEDIMENTOLOGICAL CHARACTER OF THE STUDY SECTION

5.1 General Section Descriptions

The composite Mussel Creek/Highway 263 section provides approximately 12 m of continuous vertical exposure that includes the upper part of the Cretaceous Prairie Bluff Chalk (~1 m) and much of the Pine Barren Member of the Clayton Formation (~11 m). Thirty informal units were delineated in the Pine Barren Member (Figs. 6 and 7). The general character of these units is described below, in sequence stratigraphic context.

5.1.1 Lowstand Incised Valley Fill (Unit 1, Clayton Sand)

Lowstand incised valley-fill deposits are represented by the Clayton sand (unit 1). This lenticular sand body, which varies from 0-90 cm in thickness, is composed of unconsolidated, yellowish-gray, weakly bioturbated, laminated and cross-laminated, fine- to medium-grained, carbonaceous, micaceous, quartzose sand (Figs. 7, 8, 9A). Although burrows attributed to resident organisms are present, most larger burrows pipe down from and are filled with sand derived from unit 2. The sand contains reworked Cretaceous macrofossils, localized carbonate concretions, plant detritus (including large lignite clasts), and detrital glauconite grains (Fig. 9A). The erosional base of the Clayton sand is sharp and irregular; locally, large irregular masses of the underlying Prairie Bluff Chalk extend upward into the sand bed (Fig. 8). The upper contact, a transgressive surface of erosion or ravinement surface, is also sharp and erosional and truncates stratification within the sand (Fig. 8).

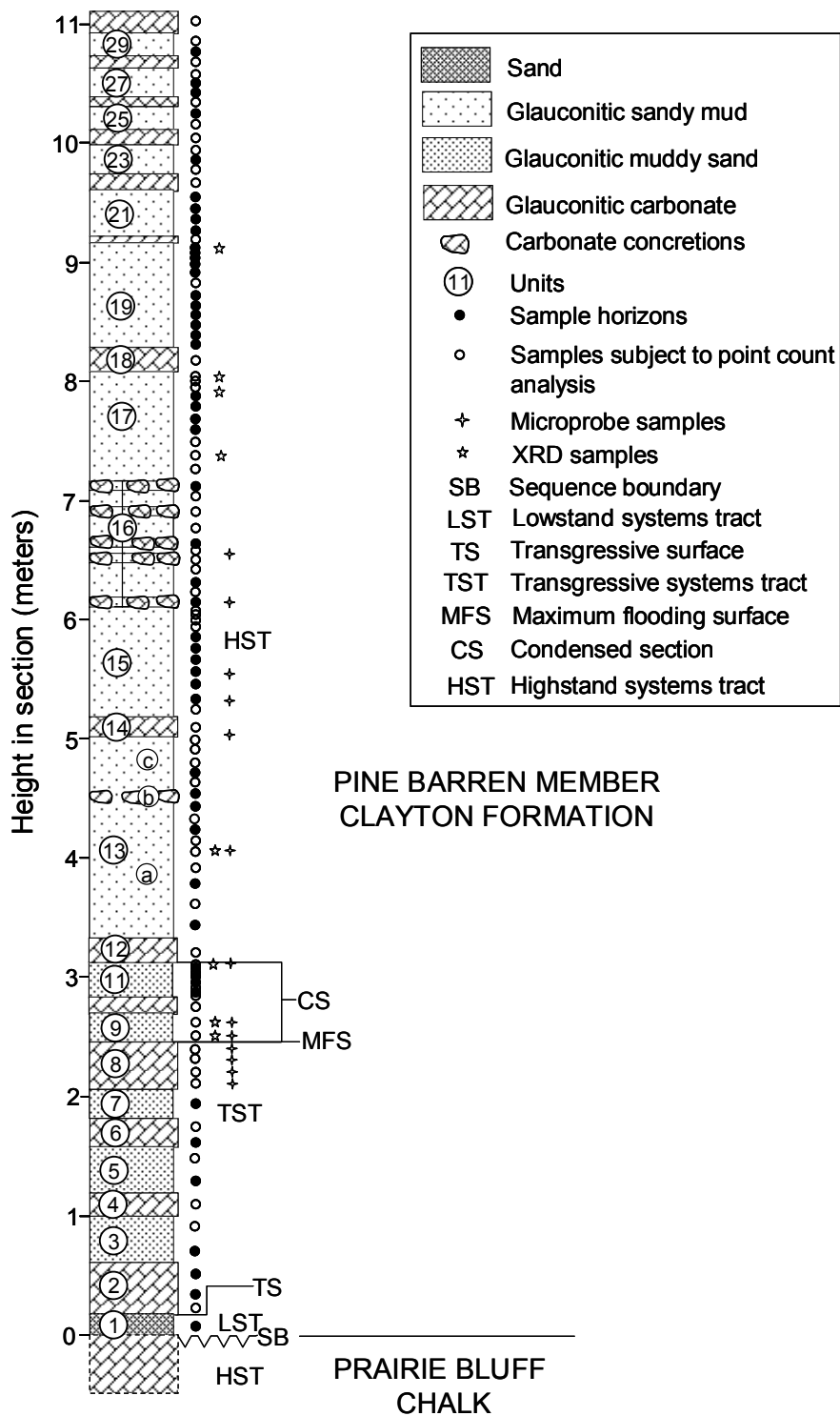


Figure 6 – Stratigraphic column of study section showing sequence stratigraphic context, informal units (1-30), and sampling horizons. Prairie Bluff Chalk and Pine Barren intervals belong to depositional sequences UZAGC 5.0 and TP 1.1, respectively.

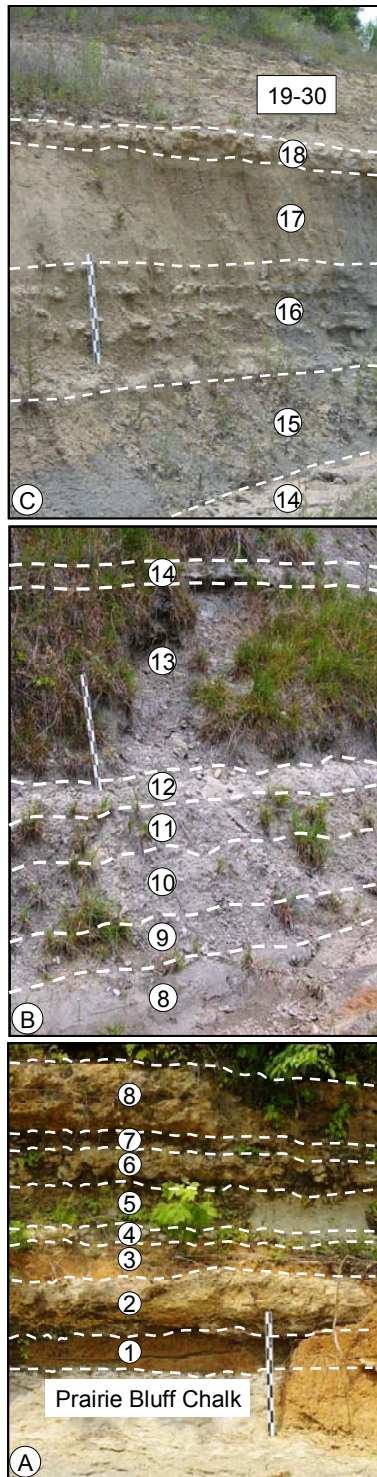


Figure 7 – Photographs of the study section. (A) Units 1-8 overlying the Prairie Bluff Chalk (Mussel Creek exposure); (B) Units 8-14 (Highway 263 exposure); (C) Units 14-30 (Mussel Creek exposure). Scale = 1 m.

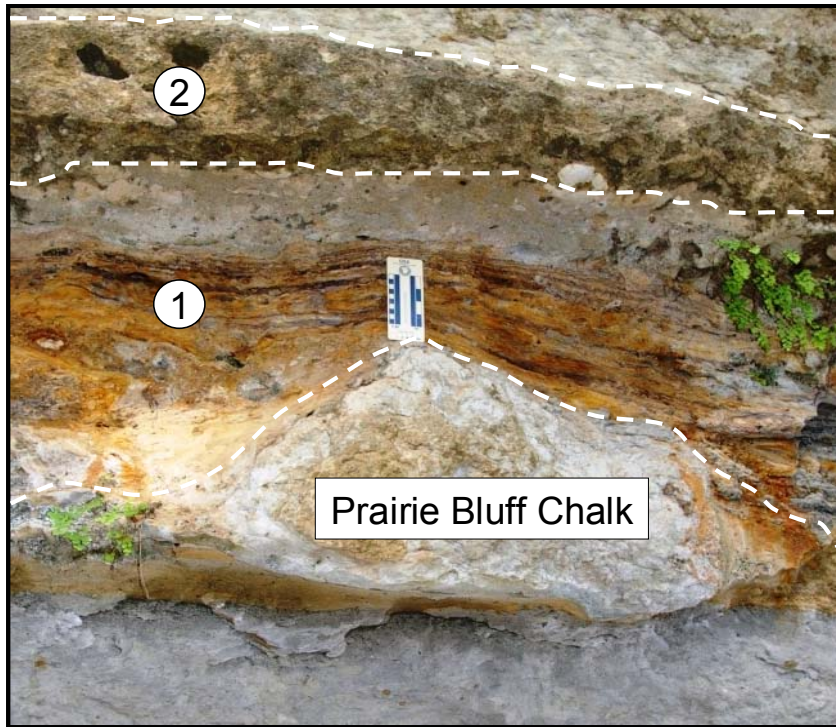


Figure 8 – Photograph of unit 1 (Clayton sand) associated with underlying Prairie Bluff Chalk and overlying transgressive lag unit (unit 2).

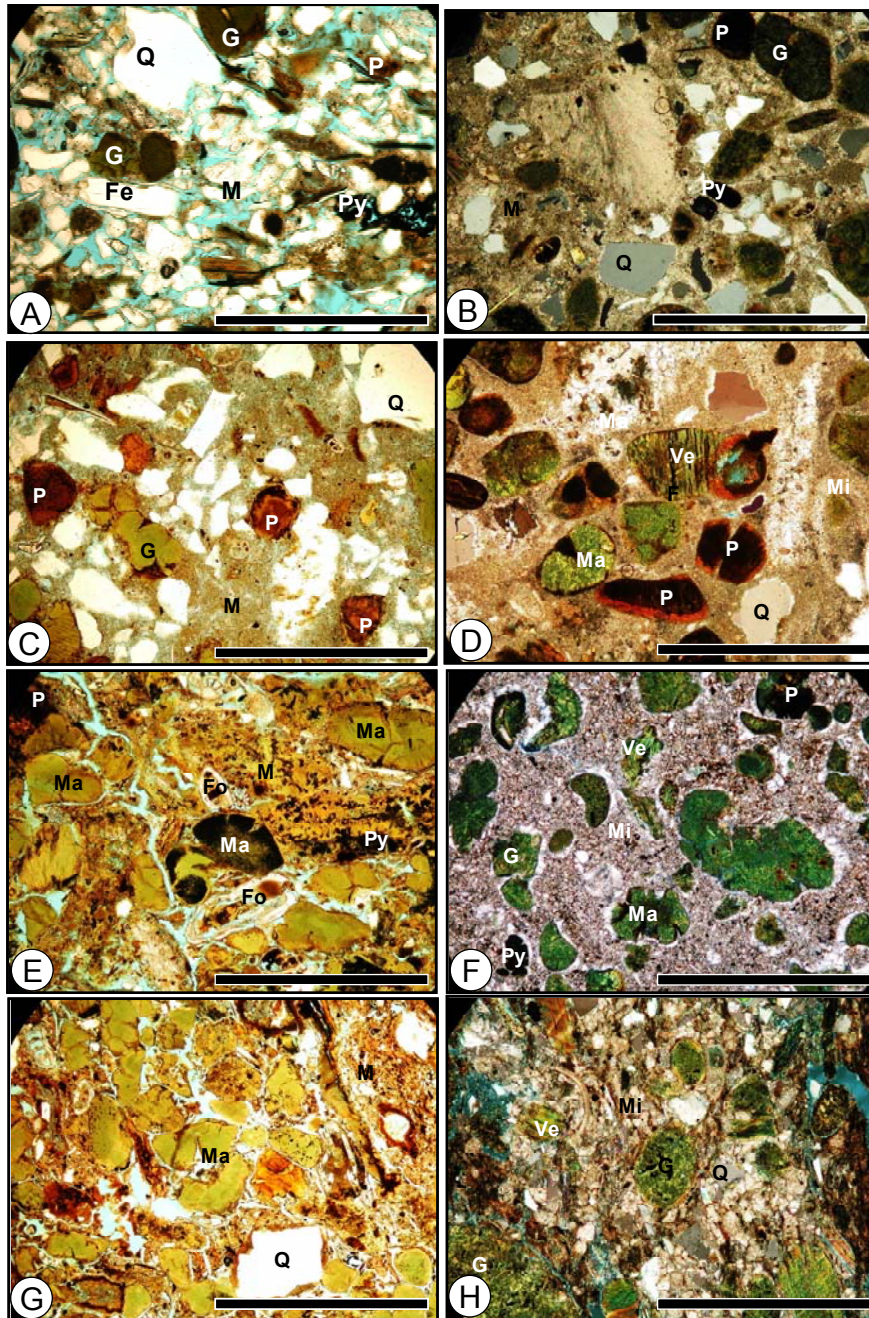


Figure 9 – Representative photomicrographs from the study section. (A) Clayton sand (unit 1); (B) Transgressive lag unit (unit 2); (C) lower part of TST (unit 3); (D) upper part of TST (unit 6); (E) muddy sand (unit 9) and (F) sandy limestone (unit 10) from condensed section; (G) sandy mud (unit 12) and (H) sandy limestone (unit 18) from HST. (G-glaucinite; Q-quartz; M-matrix; Mi-microspar; Fe-feldspar; P-phosphate; Py-Pyrite; Fo-foraminifera; Ma-mammillated glauconite grain; Ve-vermicular glauconite grain). Bar scales are ~ 1 mm.

5.1.2 Transgressive Lag (Unit 2)

Unit 2 represents a transgressive lag deposit (Figs. 6, 7). This unit, approximately 45 cm thick, is a light gray, massive, thoroughly bioturbated, micritic calcite-cemented, glauconitic, poorly-sorted, medium- to coarse-grained sandstone (Figs. 7, 9B, 10). In addition to angular clastic sand grains (quartz and subordinate feldspar), unit 2 contains common pebble-sized phosphate clasts (including molluscan steinkerns and rare shark teeth), reworked Cretaceous macrofossils (whole and fragmented), and rare quartz pebbles (Fig. 10). The contact between units 2 and 3 is irregular and gradational.

5.1.3 Transgressive Systems Tract (Units 3-8)

The transgressive systems tract, approximately 2 m thick, comprises six units (units 3-8; Figs. 6, 7, and 11). Units 3, 5, and 7 are relatively unconsolidated greenish gray glauconitic, calcareous, poorly-sorted, fine- to medium-grained muddy sands (Fig. 9C). Units 4, 6, and 8 are moderately indurated, variably glauconitic sandy limestones or marlstones (Fig. 9D). All of these units are fossiliferous, thoroughly bioturbated, and have irregular, gradational contacts (Fig. 11). Fossil assemblages include common foraminifers and bivalves (whole and fragmented) and rare bryozoans and echinoids. The upper surface of unit 8 is characterized by localized patches of small encrusting oysters and rare, intact bryozoan fronds.

5.1.4 Condensed Section (Units 9-11)

The condensed section, representing the upper- and lowermost parts of the transgressive and highstand systems tracts, respectively (Figs. 6, 7), is herein defined by maximum abundance of authigenic glauconite (see below). The glauconite maximum corresponds to a thin (<1 m) interval defined by units 9 through 11 (Fig. 7B). Units 9 and



Figure 10 – Representative photograph of carbonate cemented transgressive lag bed (unit 2) with phosphate clasts (P), and quartz pebbles (Q).

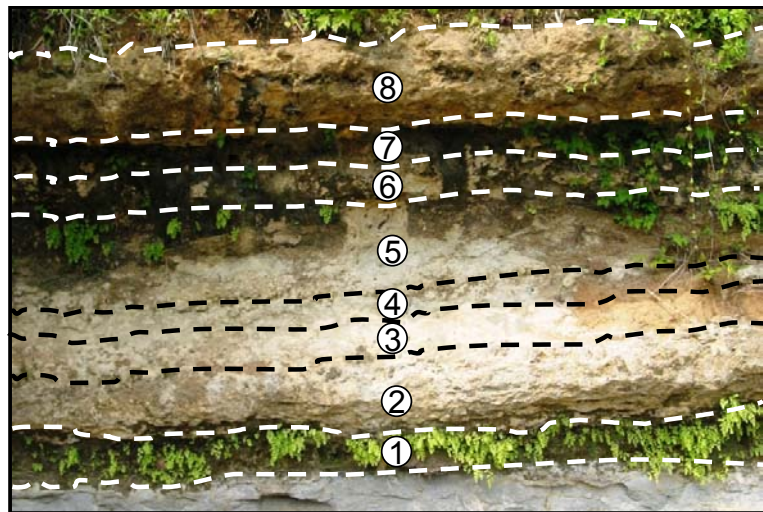


Figure 11 – Representative photograph of Clayton sand (unit 1), transgressive lag bed (unit 2), and overlying transgressive systems tract (units 3-8).

11 are unconsolidated, dark green, extremely glauconitic, poorly-sorted, fine- to medium-grained sandy muds (Figs. 6, 7, 9E). Unit 10 is an indurated, light greenish gray, highly glauconitic, sandy limestone (Fig. 9F). All of these units are thoroughly bioturbated and fossiliferous. Fossil assemblages are the same as that in the underlying units (see section 5.1.3). However, most fossils in the condensed section are partly to wholly replaced by glauconite. Contacts between units 9 through 11 and sub- and superjacent strata are relatively sharp but irregular. Irregular contacts reflect both bioturbation and differential cementation of limestones.

5.1.5 Highstand Systems Tract (Units 12-30)

The portion of the highstand systems tract represented in the composite section is characterized by alternating weakly indurated, gray to dark greenish gray, calcareous, poorly-sorted, fine- to medium-grained sandy muds (units 13a and c, 15, parts of unit 16, and all odd-numbered units from 17 through 29; Figs. 6, 7, 9G) and moderately to well-indurated, gray to light greenish gray, variably sandy, micritic limestones or marlstones (units 12, 13b, 14, parts of unit 16, and all even-numbered units from 18 through 30; Figs. 7, 9H). The uppermost four units (27-30) at the Mussel Creek section are deeply weathered and oxidized.

Limestones and marlstones generally form discrete, continuous beds. However, those in unit 16 are defined by discontinuous, irregular nodules (Fig. 7), reflecting a concretionary origin for at least some of the carbonate-rich units. In most limestones/marlstones, micrite has been recrystallized to microspar (Fig. 9H).

Contacts between sandy muds and limestones/marlstones are generally fairly sharp despite thorough bioturbation of the entire package. Large (up to 5 cm in diameter)

burrows assigned to *Thalassinoides* are particularly evident in and below nodular limestones owing to preferentially cementation of burrow fills (Fig. 12A).

All units in the highstand systems tract are fossiliferous. Macrofossils include common whole and fragmented molluscan remains (bivalves and gastropods) and rare shark teeth. Mollusks are most obvious in the limestones where they typically are preserved as relatively well preserved shells and as external molds and steinkerns (Fig. 12B). All of the units of the highstand systems tract contain glauconite. However, as will be described below, glauconite contents generally decrease upward through the package, in both the sandy muds and carbonate-rich units.

5.2 Textural Analyses

Textural analyses were performed on all 110 samples collected from units 1 through 30 (see Fig. 6). Calculated sand percentage and mean sand size are given in Table 4 and are plotted versus stratigraphic height in Figure 12.

As expected, sand content is highest (78%) in unit 1 (Clayton sand). In the remainder of the section, sand percentages vary significantly from 0% to ~60%. Several general patterns are observed in the data. First, there is a general trend toward decreasing sand content upward through the section. Second, higher-frequency variations in percent sand define four fining-upward cycles, one in the transgressive systems tract (units 1-8) and three in the condensed section/highstand systems tract (units 9-13, 13-16, and 17-30). Hereafter, these are referred to as cycles 1, 2, 3, and 4, in ascending order. Several of these cycles appear to contain even higher-frequency fining-upward cycles (e.g., mini-cycles 4a, b, and c, Fig. 13).

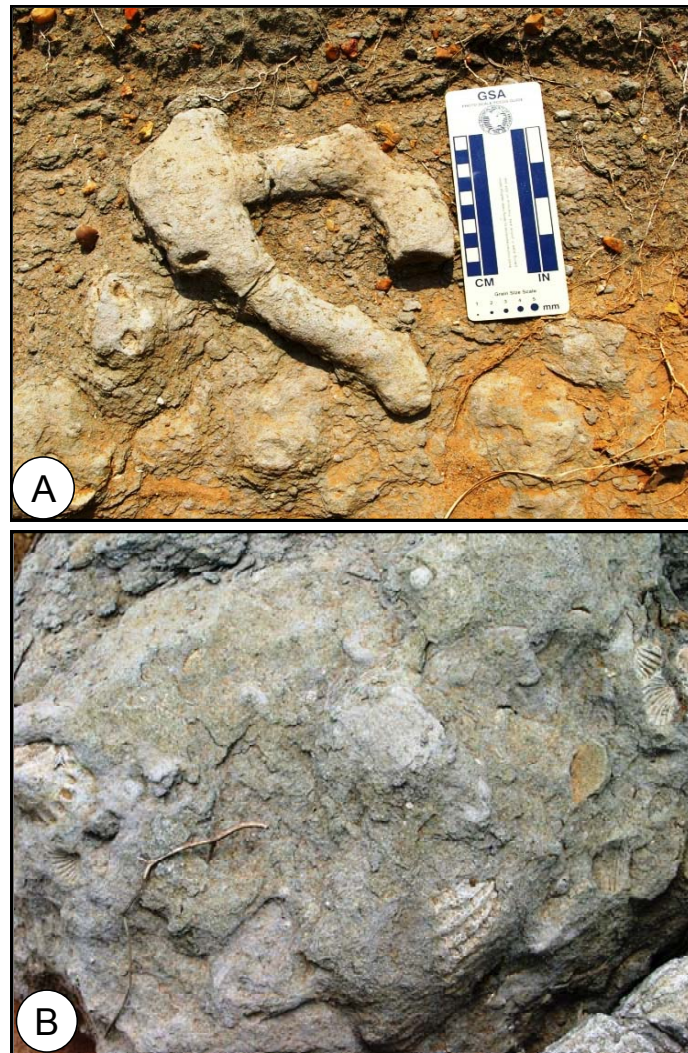


Figure 12 – Representative photographs of highstand systems tract. (A) Large *Thalassinoides* associated with the nodular limestones (unit 16); (B) Large mollusks in marlstone.

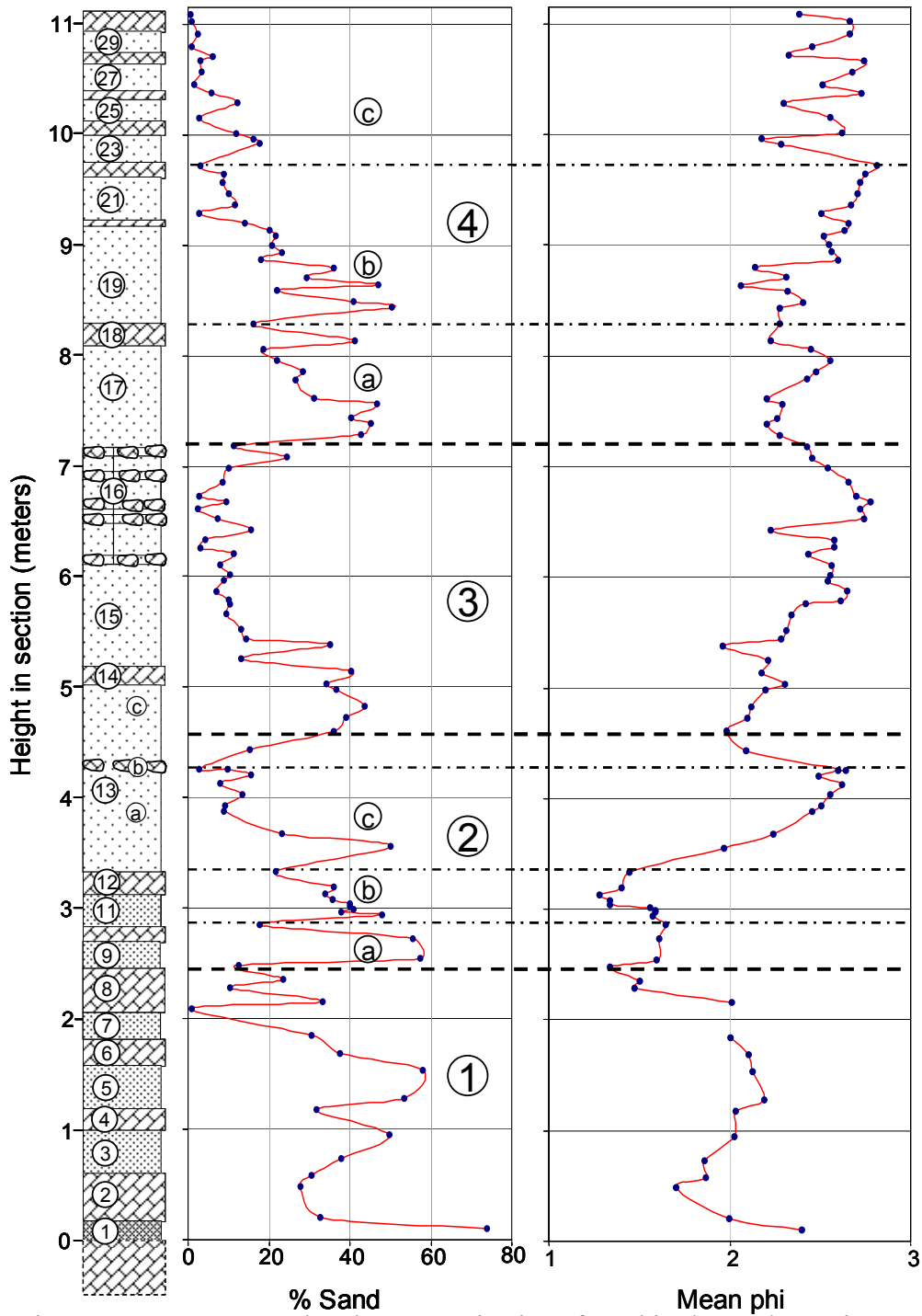


Figure 13 – Percent sand and mean grain size of sand in the study section. Textural data reveals four fining-upward cycles (1-4) and associated mini-cycles (e.g., 4a, b, and c). Dashed and dot-dashed lines define boundaries of cycles and mini-cycles, respectively. Section legend is shown in figure 6.

Mean sand size ranges from 2.75 Φ (fine sand) to ~1.25 Φ (medium sand) (Table 4, Fig. 13). As a generalization, mean sand size decreases (increasing Φ) upward through the section. Higher-frequency cycles of decreasing sand size match the cycles and, in some cases, the minicycles, in sand percent; i.e., sand size generally covaries with percent sand. Notably, the coarsest sands occur in units 8 through 12 and generally coincide with the condensed section.

5.3 Carbonate and Organic Carbon Analyses

Carbonate and organic carbon data derived from all 110 samples are given in Table 4 and plotted against stratigraphic height and percent sand in Figure 14. Carbonate contents are lowest (14.8%) in unit 1 (Clayton sand) and range widely from ~20% to ~80% throughout the remainder of the section. Not surprisingly, carbonate contents are highest in the indurated limestones/marlstones (mostly >60% CaCO₃) and lowest (typically <60% CaCO₃) in the poorly indurated muddy sand and sandy muds. As a generalization, carbonate-rich units seem to coincide with the upper parts of the cycles and/or minicycles defined from textural data (Fig. 14).

Organic carbon contents are generally low (0.13% to 0.37%) in the relatively carbonate-rich transgressive system tract and condensed section (units 2-12). Values are variable but generally higher in the highstand systems tract, with the exception of the upper oxidized portion of the section. Organic carbon contents vary inversely with carbonate content (Fig. 15). Higher organic contents (up to 1.1%) generally correspond to sandy muds (Fig. 14; e.g., lower part of unit 13, unit 15, etc.).

Table 4 – Percent sand, mean sand size, and percent carbonate and organic carbon data.

Sample name	Sample number	Height in section (cm)	% Sand	Mean Phi (Φ)	% Carbonate	% Organic Carbon
MC-1-1-11	1	10	73.849	2.395	14.799	0.370
MC-2-0-5	2	20.5	32.522	1.995	59.226	0.257
MC-2-23-37	3	48	27.824	1.704	68.222	0.174
MC-2-37-45	4	58	30.470	1.866	60.210	0.199
MC-3-0-15	5	73	37.945	1.859	47.292	0.222
MC-3-28-35	6	94.5	49.798	2.028	34.183	0.245
MC-4-12-17	7	118	31.814	2.030	65.437	0.216
MC-5-0-10	8	128	53.414	2.189	30.313	0.289
MC-5-25-35	9	153	57.985	2.124	46.985	0.233
MC-6-0-12	10	169	37.642	2.105	57.772	0.174
MC-6-18-25	11	184.5	30.547	2.006	69.043	0.139
MC-7-19-23	12	209	0.848		80.383	0.335
MC-8-0-5	13	215.5	33.426	2.014	62.448	0.153
MC-8-10-20	14	228	10.330	1.470	72.841	0.172
MC-8-20-25	15	235.5	23.392	1.505	75.517	0.146
MC-8-30-40	16	248	12.553	1.336	74.742	0.126
MC-9-0-3	17	254.5	57.388	1.598	28.998	0.249
MC-9-13-25	18	273	55.550	1.607	26.993	0.216
MC-10-0-15	19	285.5	17.730	1.648	69.658	0.204
MC-11-0-1	20	293.5	47.889	1.573	34.982	0.272
MC-11-1-5	21	297	37.908	1.590	21.768	0.276
MC-11-5-7	22	299	41.068	1.589	22.020	0.239
MC-11-7-9	23	301	40.051	1.560	20.070	0.268
MC-11-9-12	24	303.5	40.079	1.334	20.212	0.255
MC-11-12-18	25	308	35.863	1.335	24.614	0.270
MC-11-18-23	26	313	33.845	1.283	22.896	0.257
MC-11-24-29	27	319	36.084	1.401	21.818	0.274
MC-12-3-17	28	333	21.785	1.444	68.174	0.213
MC-13a-0-5	29	355.5	50.011	1.970	25.208	0.541
MC-13a-10-20	30	368	23.198	2.243	25.676	1.100
MC-13a-30-40	31	388	8.933	2.458	27.195	1.060
MC-13a-35-45	32	393	9.140	2.507	29.752	1.040
MC-13a-45-55	33	403	13.376	2.559	26.124	1.060
MC-13a-55-65	34	413	7.916	2.620	26.894	1.080
MC-13a-65-70	35	420.5	15.660	2.492	28.038	1.040
MC-13b-70-75	36	425.5	9.739	2.601	30.671	0.921
MC-13b-70-75	37	425.5	2.627	2.638	70.582	0.465
MC-13b-85-95	38	443	15.277	2.093	78.063	0.403
MC-13b-100-115	39	460.5	35.910	1.980	78.847	0.330
MC-13c-115-125	40	473	39.109	2.100	21.805	0.485

Table 4 – Continued.

Sample name	Sample number	Height in section (cm)	% Sand	Mean Phi (Φ)	% Carbonate	% Organic Carbon
MC-13c-125-135	41	483	43.554	2.120	21.204	0.537
MC-13c-140-147	42	498	36.549	2.194	20.507	0.644
MC-13c-147-153	43	503	34.189	2.307	21.700	0.546
MC-13c-160-162	44	514	40.414	2.176	31.862	0.504
MC-14-0-15	45	525.5	13.226	2.212	50.489	0.197
MC-15-3-7	46	538	35.039	1.959	31.417	0.718
MC-15-8-13	47	543.5	14.411	2.282	35.324	0.986
MC-15-15-23	48	552	13.101	2.314	32.310	0.942
MC-15-28-38	49	566	9.492	2.340	26.746	1.090
MC-15-40-45	50	575.5	10.504	2.418	25.438	1.070
MC-15-42-50	51	579	10.176	2.612	29.260	1.110
MC-15-50-58	52	587	7.106	2.646	30.958	1.100
MC-15-60-68	53	597	8.957	2.538	33.372	1.100
MC-15-65-72	54	601.5	10.234	2.554	28.655	1.080
MC-15-75-80	55	610.5	8.069	2.566	37.159	0.964
MC-15-85-90	56	620.5	11.346	2.437	51.396	0.848
MC-16a-0-7	57	626.5	3.140	2.575	72.394	0.473
MC-16b-bottom	58	634	4.263	2.576	33.219	1.030
MC-16b-middle	59	643	15.609	2.227	34.012	1.040
MC-16b-top	60	653	7.206	2.741	34.450	0.907
MC-16c-35-42	61	661.5	2.532	2.722	80.434	0.325
MC-16d-42-47	62	667.5	9.420	2.779	32.423	0.904
MC-16e-47-53	63	673	2.674	2.699	73.323	0.410
MC-16f-53-72	64	686	8.702	2.658	30.668	0.998
MC-16g-72-78	65	698	9.977	2.543	72.852	0.443
MC-16h-78-92	66	708	24.412	2.453	28.209	0.729
MC-16i-92-98	67	718	11.361	2.423	48.680	0.430
MC-17-0-15	68	728.5	42.737	2.274	26.283	0.527
MC-17-15-20	69	738.5	45.086	2.204	20.326	0.577
MC-17-20-25	70	743.5	40.385	2.261	20.247	0.818
MC-17-25-45	71	756	46.742	2.290	18.311	0.558
MC-17-35-45	72	761	31.129	2.205	20.362	0.678
MC-17-55-60	73	778.5	26.433	2.427	18.363	0.812
MC-17-60-70	74	786	28.269	2.478	20.101	0.473
MC-17-70-80	75	796	22.098	2.553	18.245	0.661
MC-17-80-90	76	806	18.524	2.446	16.195	0.853
MC-17-90-95	77	813.5	41.077	2.223	37.939	0.391
MC-18-5-20	78	828.5	16.207	2.276	68.456	0.249
MC-19-5-10	79	843.5	50.340	2.279	19.956	0.651
MC-19-10-15	80	848.5	40.924	2.407	19.006	0.420

Table 4 – Continued.

Sample name	Sample number	Height in section (cm)	% Sand	Mean Phi (Φ)	% Carbonate	% Organic Carbon
MC-19-20-25	81	858.5	22.130	2.316	36.202	0.579
MC-19-25-30	82	863.5	47.164	2.064	20.829	0.458
MC-19-30-40	83	871	29.241	2.315	24.028	0.512
MC-19-40-47	84	879.5	35.905	2.139	21.375	0.539
MC-19-47-55	85	887	17.990	2.598	20.271	0.599
MC-19-55-60	86	893.5	23.093	2.561	25.737	0.654
MC-19-60-68	87	900	20.901	2.548	27.836	0.693
MC-19-70-75	88	908.5	21.583	2.517	30.370	0.662
MC-19-75-80	89	913.5	20.132	2.631	35.658	0.657
MC-19-82-86	90	920	14.121	2.659	38.881	0.567
MC-20-0-5	91	928.5	2.820	2.504	46.011	0.245
MC-21-0-10	92	936	11.682	2.673	82.572	0.654
MC-21-10-20	93	946	10.124	2.708	39.040	0.529
MC-21-20-30	94	956	8.599	2.721	30.641	0.961
MC-21-30-37	95	964.5	8.833	2.747	29.880	0.840
MC-22-0-13	96	971.5	3.040	2.814	32.319	0.312
MC-23-5-10	97	991.5	17.721	2.284	74.628	0.154
MC-23-10-15	98	996.5	16.207	2.173	70.689	0.231
MC-23-15-20	99	1001.5	12.036	2.619	60.716	0.300
MC-24-0-12	100	1015	2.889	2.554	39.290	0.127
MC-25-5-10	101	1028.5	12.352	2.297	81.006	0.268
MC-25-15-18	102	1037.5	5.668	2.727	47.789	0.318
MC-26-0-8	103	1045	1.471	2.512	30.578	0.164
MC-27-5-10	104	1056.5	3.245	2.674	69.375	0.377
MC-27-15-20	105	1066.5	2.979	2.739	29.610	0.334
MC-27-20-24	106	1071	6.223	2.328	31.025	0.230
MC-28-1-11	107	1079.5	0.773	2.453	49.606	0.149
MC-29-2-10	108	1091	2.495	2.663	77.152	0.282
MC-29-15-20	109	1102.5	1.056	2.664	41.048	0.282
MC-30-1-8	110	1108.5	0.574	2.380	79.810	0.152

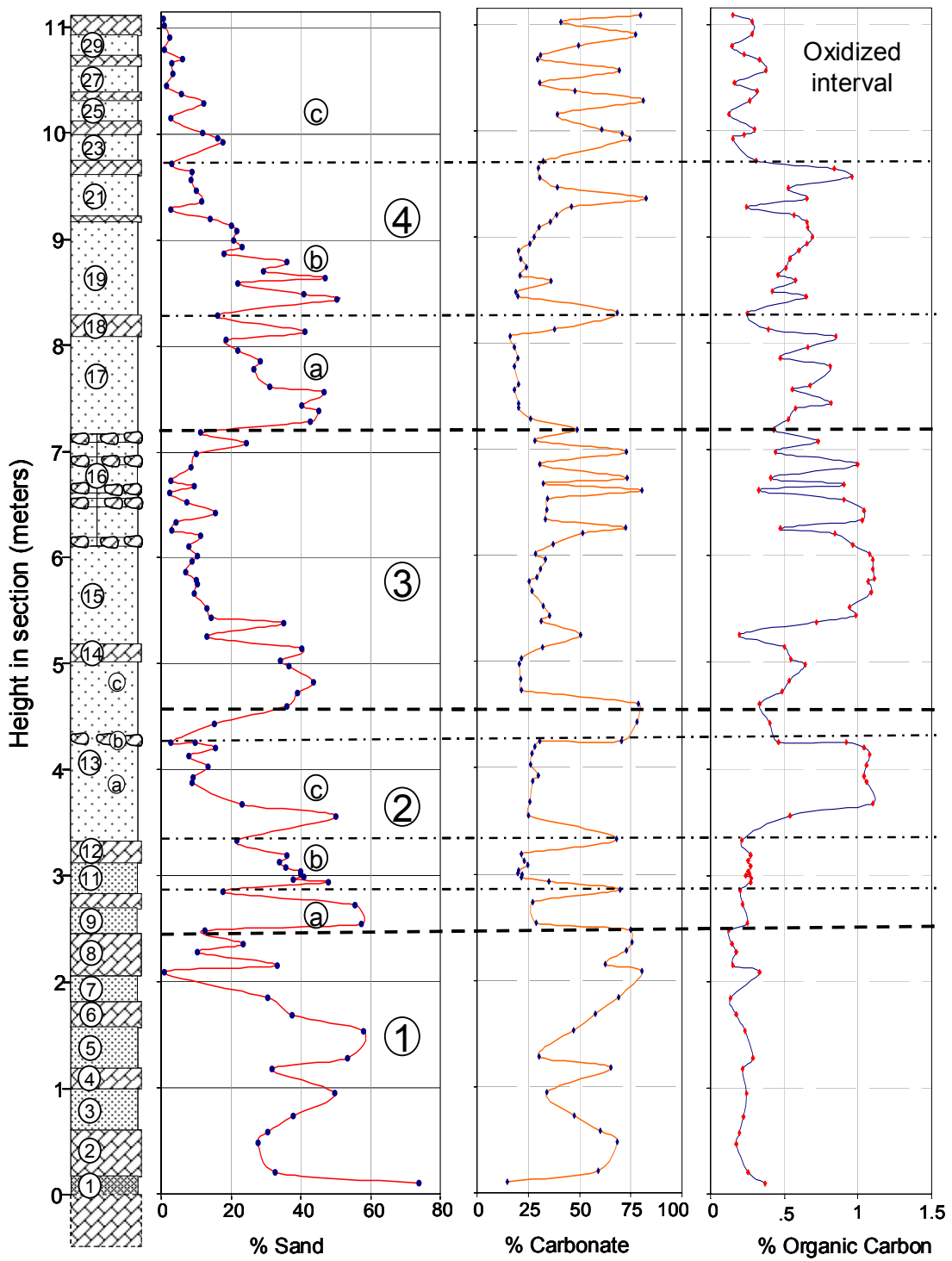


Figure 14 – Percent sand, carbonate, and organic carbon in the study section. Dashed and dot-dashed lines define boundaries of cycles and mini-cycles, respectively. Section legend is shown in figure 6.

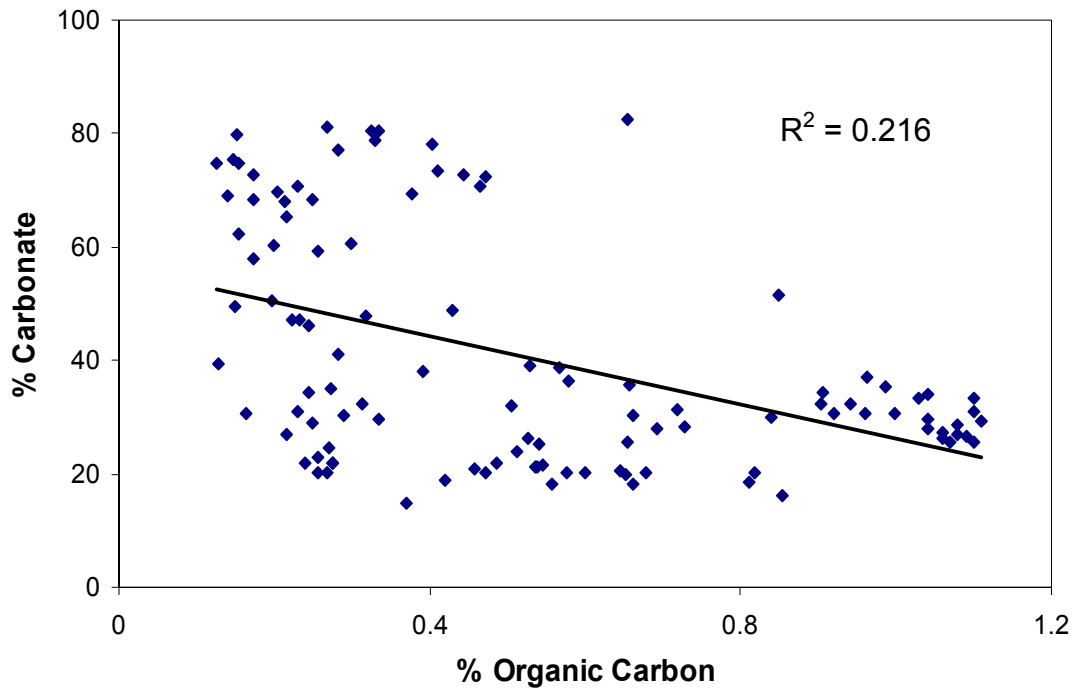


Figure 15 – General inverse relationship between percent carbonate and organic carbon.

5.4 General Petrography and Point-Count Analyses

5.4.1 General Observations

General petrographic observations of thin sections of all samples and point-count analyses of selected samples indicate that sediments are composed mostly of matrix (0% to 95%), glauconite (0% to 95%), quartz (0.3% to 20.9%), skeletal fragments (0% to 20%), and other diagenetic minerals (phosphatic grains, 0% to 10%; pyrite, 0% to 3.5%). The abundances of these major constituents based on point-count analyses are given in Table 5. Minor constituents include feldspars and large micas.

The matrix fractions in the sandy mud and muddy sand units are characterized by very fine-grained, randomly-oriented clay, fine micas, and other unidentifiable components. Matrix in carbonate-rich units (marlstones and limestones) is composed of micrite or recrystallized micrite (microspar).

Glauconite of various morphotypes (see Chapter 6) is observed in variable abundance in all units except those at the top of the section (units 27-30) (Fig. 16). Glauconite contents are relatively low in the Clayton sand (unit 1), transgressive lag (unit 2), and the transgressive systems tract (units 3-8). Glauconite abundance reaches a maximum (up to ~94%) in the condensed section (units 9-11) and trends toward lower values through the highstand systems tract (Fig. 16). However, glauconite abundance varies cyclically through the condensed section/highstand systems tract interval. These asymmetric cycles, marked by relatively rapid increases and gradual decreases in glauconite abundance are coincident with textural cycles 2, 3, and 4 and, in some cases, associated mini-cycles; above the transgressive systems tract, glauconite abundance correlates strongly with, and is responsible for, the observed fining-upward cycles. A

Table 5 – Relative abundance of grain types based on point-counts of selected samples from the study section.

Sample name	Height in section (cm)	% Matrix	% Glauconite	% Quartz	% Fossil Fragments	% Phosphate	% Pyrite	% Other
MC-2-0-5	20.5	57.7	11.2	15.7	6.3	3.9	0.0	5.1
MC-3-28-35	94.5	50.7	22.2	20.9	2.9	1.9	0.0	1.4
MC-4-12-17	118	62.2	5	16.8	7.8	1.3	2.8	4.3
MC-5-25-35	153	39.9	24.1	25.5	7.1	1.3	1.9	0.2
MC-6-18-25	184.5	51.5	9.5	18.5	16.2	0.0	0.6	3.7
MC-8-0-5	215.5	54.3	11.8	19.0	12.0	2.2	0.0	0.6
MC-8-10-20	228	41.7	27.1	14.3	13.0	4.4	0.0	0.0
MC-8-20-25	235.5	37.9	31.2	12.3	8.4	10.1	0.0	0.1
MC-8-30-40	248	2.4	91.2	3.2	13.8	1.6	0.0	0.0
MC-9-0-3	254.5	3.2	94.2	0.6	14.1	0.3	0.0	0.0
MC-9-13-25	273	15.5	76	3.0	14.1	0.0	0.0	0.0
MC-10-0-15	285.5	37.7	55.5	0.9	8.6	1.5	0.3	0.0
MC-11-0-1	293.5	0.0	93.2	1.5	19.9	1.5	0.0	0.0
MC-11-5-7	299	16.7	80.1	0.0	13.4	0.3	0.0	0.0
MC-11-12-18	308	34.6	63.8	1.5	12.6	0.0	0.0	0.0
MC-11-24-29	319	11.4	87.3	0.6	9.2	0.0	0.0	0.0
MC-12-3-17	333	54.4	41.2	0.3	10.3	0.3	0.0	0.0
MC-13a-10-20	368	66.9	27.2	1.9	4.6	0.3	0.0	0.0
MC-13a-35-45	393	83.1	8.8	1.7	3.3	1.4	1.4	0.3
MC-13a-45-55	403	84.1	11.4	1.6	2.2	0.3	0.6	0.0
MC-13a-55-65	413	87.0	8.4	0.3	4.6	0.0	0.0	0.0
MC-13b-70-75	425.5	82.8	10.9	1.7	4.6	0.0	0.0	0.0
MC-13c-115-125	473	33.4	53.5	1.7	8.0	0.0	0.0	3.4
MC-13c-140-147	498	61.4	36.2	0.9	2.6	0.0	0.3	0.0
MC-13c-147-153	503	28.4	64.6	3.1	3.1	0.0	0.0	0.8
MC-13c-160-162	514	45.6	40.1	3.3	6.1	0.0	0.0	4.9
MC-14-0-15	525.5	50.8	37.3	2.6	6.5	0.0	0.7	2.1

Table 5 – Continued.

Sample name	Height in section (cm)	% Matrix	% Glauconite	% Quartz	% Fossil Fragments	% Phosphate	% Pyrite	% Other
MC-15-3-7	538	33.0	56.3	2.3	10.3	0.0	0.7	0.0
MC-15-60-68	597	63.4	17.4	2.1	7.4	0.0	2.4	7.4
MC-15-65-72	601.5	77.6	13.3	2.0	5.2	0.0	1.7	0.1
MC-15-75-80	610.5	56.3	35.8	1.7	6.2	0.0	1.4	0.0
MC-15-85-90	620.5	59.7	35.2	3.8	2.0	0.0	3.4	0.0
MC-16b-bottom	634	64.9	32.8	0.3	3.1	0.0	1.6	0.0
MC-16b-top	653	66.6	31.5	0.0	2.8	0.0	0.0	0.0
MC-16c-35-42	661.5	82.5	14.4	0.3	0.6	0.0	2.7	0.0
MC-16d-42-47	667.5	77.0	18.9	0.0	4.8	0.0	3.0	0.0
MC-16f-53-72	686	79.7	17.6	0.3	2.0	0.0	0.7	0.0
MC-16g-72-78	698	84.2	12.2	0.0	1.0	0.0	2.6	0.0
MC-16h-78-92	708	88.1	5.4	0.0	5.4	0.0	1.0	0.0
MC-17-0-15	728.5	18.7	71.8	7.5	6.6	0.0	0.0	0.0
MC-17-15-20	738.5	45.8	53.4	0.0	3.2	0.0	0.0	0.0
MC-17-20-25	743.5	41.9	58.7	0.3	5.6	0.0	0.0	0.0
MC-17-70-80	796	76.6	21.9	0.0	2.5	0.0	0.0	0.0
MC-17-80-90	806	78.6	20	0.0	2.1	0.0	0.0	0.0
MC-17-90-95	813.5	39.2	52.5	6.5	7.2	0.0	0.0	0.0
MC-18-5-20	828.5	74.0	16.9	6.0	3.6	0.0	0.0	0.0
MC-19-47-55	887	61.2	32	5.4	3.4	0.0	0.0	0.0
MC-20-0-5	928.5	80.1	7.9	7.2	4.0	0.0	0.0	0.8
MC-22-0-13	971.5	94.3	0.6	1.9	3.1	0.0	0.0	0.0
MC-23-5-10	991.5	92.9	3	3.3	1.8	0.0	0.0	0.0
MC-23-15-20	1001.5	90.4	2.6	4.5	2.6	0.0	0.0	0.0
MC-24-0-12	1015	90.0	4	2.0	4.0	0.0	0.0	0.0
MC-25-5-10	1028.5	96.0	1.9	0.6	1.5	0.0	0.3	0.0
MC-26-0-8	1045	90.1	1.6	3.3	5.0	0.0	0.0	0.1
MC-27-20-24	1071	97.2	0	1.1	1.7	0.0	0.0	0.0
MC-28-1-11	1079.5	96.8	0	1.4	1.8	0.0	0.0	0.0
MC-29-15-20	1102.5	96.6	0	0.0	3.4	0.0	0.0	0.0
MC-30-1-8	1108.5	95.8	0	4.2	0.0	0.0	0.0	0.0

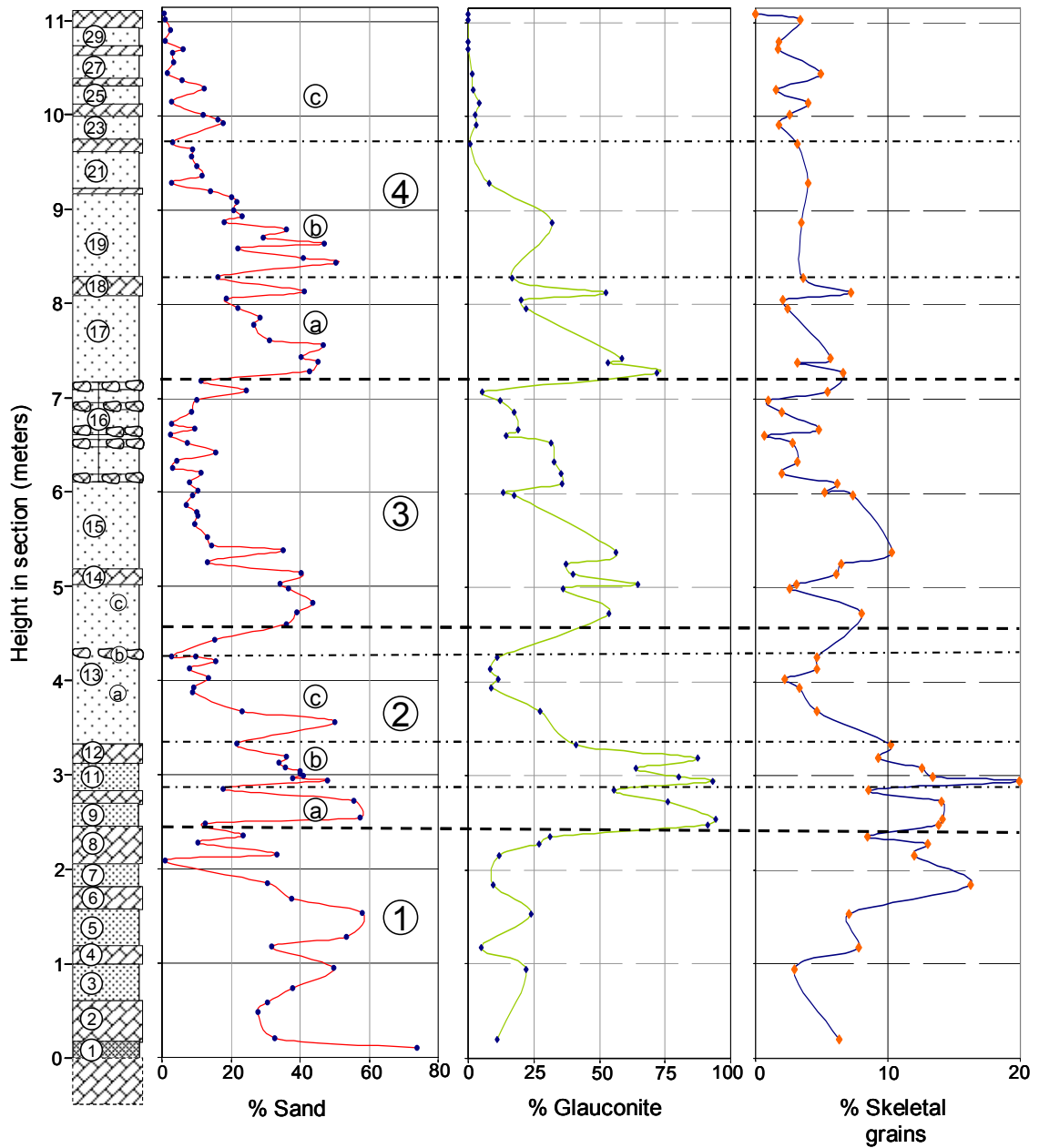


Figure 16 – Percent sand, percent glauconite, and percent skeletal grains (including glauconitized grains) in the study section. Dashed and dot-dashed lines define boundaries of cycles and mini-cycles, respectively. Section legend is shown in figure 6.

bivariate plot of sand versus glauconite shows a positive correlation (Fig.17). In contrast, glauconite shows a weak inverse relationship with carbonate content (Fig. 18).

Quartz grains fall within the fine- to medium-grained range. They are typically angular to subangular, monocrystalline, and nonundulose.

Skeletal allochems recognized include foraminifers and bivalve, echinoderm (echinoid spines), and bryozoan fragments. Skeletal grain abundance increases upward through the transgressive systems tract (units 3-8), reaches a peak in the condensed section (units 9-11), and generally decreases through the highstand systems tract (units 12-30) (Fig. 16). In the condensed section and highstand systems tract, abundance of skeletal allochems is generally proportional to percent glauconite, particularly within cycles 2 and 3. Replacement of fossil fragments by glauconite is common in the condensed section and lower part of highstand systems tract (units 8-13) and gradually decreases upward (see Chapter 6).

Diagenetic components other than glauconite include phosphate grains and pyrite.

Abundance of phosphatic grains decreases gradually upward through the bulk of the transgressive systems tract (units 3-7) and then increases abruptly to a maximum in unit 8 (top of cycle 1) (Fig. 19). Phosphate decreases through the condensed section and lowermost part of highstand systems tract. No phosphatic grains were recognized above unit 13. Pyrite is common only in units 4-6, 13, and 15-16, in the middle to upper portions of cycles 1-3 (Fig. 19). Notably, pyritiferous intervals in cycles 2 and 3 correspond to relatively glauconite-poor and organic-rich intervals (compare Figs. 14, 16, and 19).

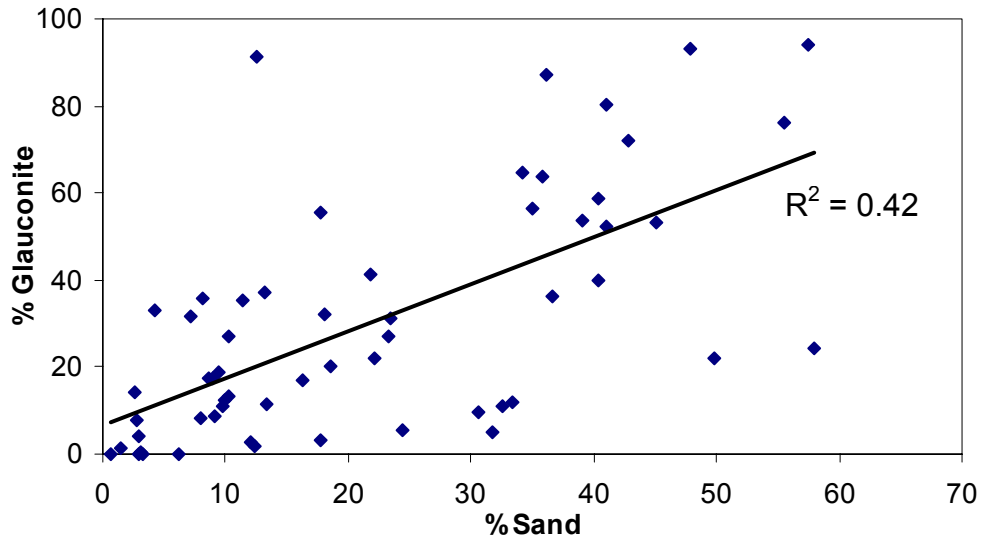


Figure 17 – Percent glauconite vs. percent sand in the samples.

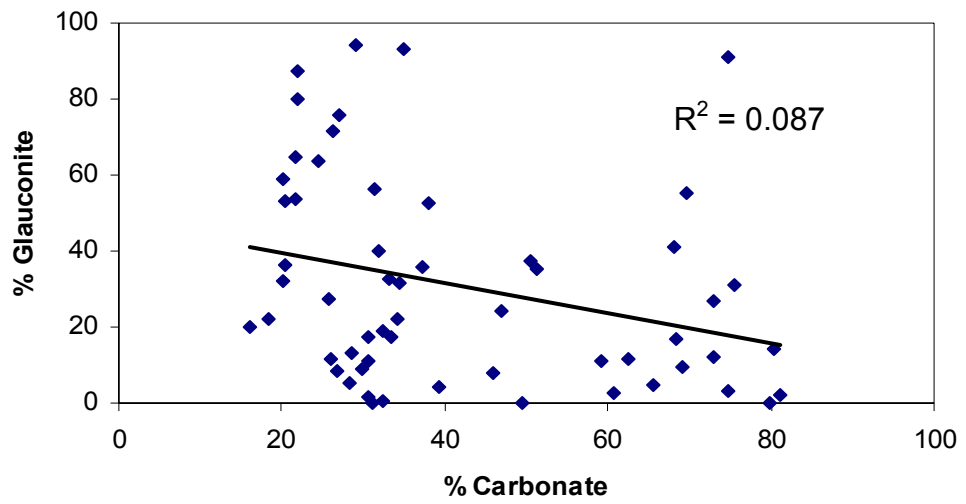


Figure 18 – Relationship between percent carbonate and percent glauconite.

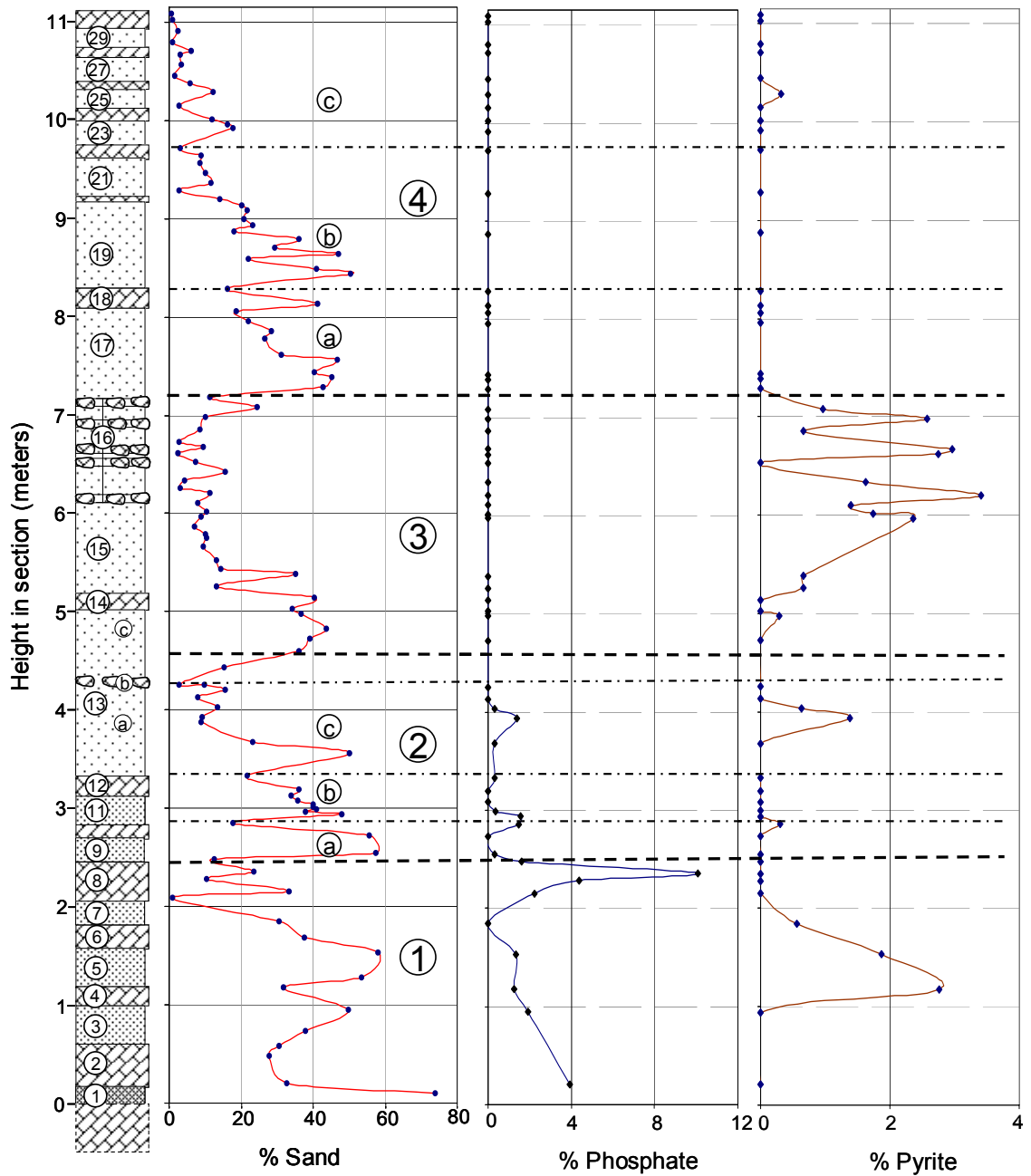


Figure 19 – Relationship between percent sand, percent phosphate, and percent pyrite in the study section. Dashed and dot-dashed lines define boundaries of cycles and mini-cycles, respectively. Section legend is shown in figure 6.

5.5 Summary and Interpretation

The observations described above support the general sequence stratigraphic interpretations for the study section. Units 9-11 were identified as the condensed section based on peak glauconite abundance (Fig. 16). This interpretation is supported by maxima in skeletal grain abundance (Fig. 16) and sand-grain size (Fig. 13) and by relatively high concentrations of phosphatic grains (Fig. 19) in this interval. Like glauconite, these parameters reflect limited supply of clastic sediment and/or winnowing. General trends towards decreased glauconite content, skeletal grain abundance (Fig. 16), sand percent, and mean sand size through the interval above unit 11 (Fig. 13) reflect a progressive increase in the influx of finer clastic sediments and limited winnowing of finer-grained sediments. These trends are consistent with a highstand systems-tract succession.

Observations also help to delineate parasequences that likely record 4th-order relative sea-level fluctuations. The aforementioned asymmetrical sand/glauconite cycles, particularly cycles 2 through 4, are interpreted as parasequences (Fig. 20). In this interpretation, the boundaries between cycles 1-4 are inferred to be marine flooding surfaces (Fig. 20). Abrupt increases in sand percent, mean sand size, and glauconite content (Figs. 13, 14, 20) across these surfaces represent phases of rapid sea-level rise and sediment starvation. Gradual decreases in these same parameters above each surface reflect progressive increases in clastic sediment flux associated with phases of slower transgression, sea-level stillstand, or perhaps minor regression. Parasequence delineation is supported by trends in the relative abundance of skeletal allochems and organic carbon. Skeletal allochems are generally more common near parasequence bases (Fig. 16),

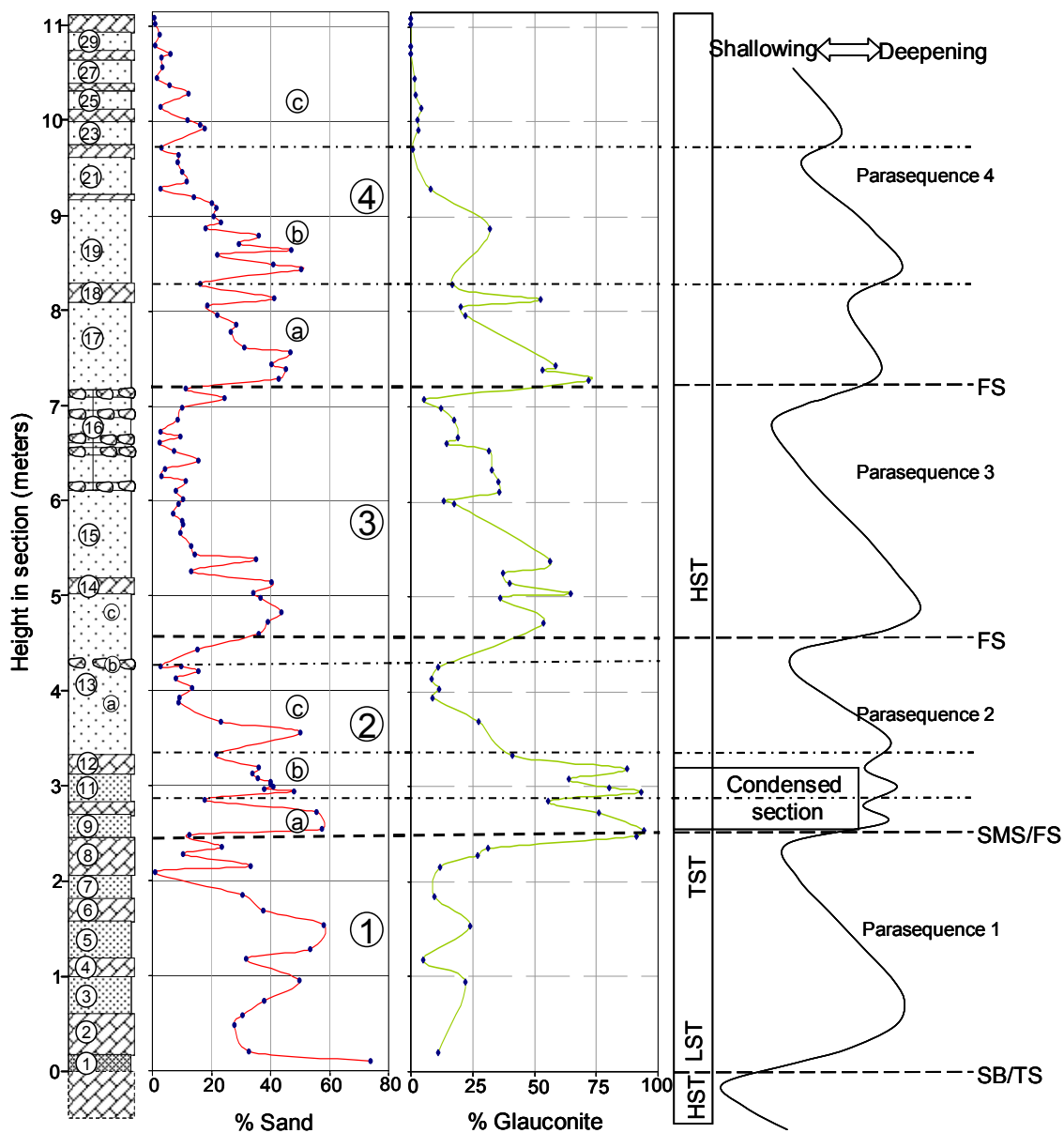


Figure 20 – Stratigraphic column and inferred sea-level curves for the Clayton Formation. HST-Highstand systems tract; LST-Lowstand systems tract; TST-Transgressive systems tract; SB-Sequence boundary; TS-Transgressive surface; SMS-Surface of maximum starvation; FS-Flooding surface. Dashed lines define boundaries of cycles, here inferred to the parasequence bounding flooding surfaces. Dot-dashed lines define boundaries of mini-cycles, which may correspond to higher-order sea-level fluctuations. Section legend is shown in figure 6.

reflecting limited dilution by clastic sediments. Organic carbon contents are generally higher in upper parts of parasequences (Fig. 14), perhaps reflecting increased preservation of organic matter associated with higher sedimentation rates. The relationships between inferred parasequences, sea-level dynamics, and limestone formation are problematic and will be addressed in subsequent discussion (Chapter 7).

Two of the sedimentary cycles (parasequences 2 and 4) contain minicycles (2a, b, and c; 4a, b, and c) defined by smaller-scale asymmetrical cycles in sand content and glauconite. These minicycles are interpreted to reflect shorter-term, 5th-order sea-level variations (Fig. 20).

The observations presented thus far indicate that glauconite is nearly ubiquitous throughout the study section. However, glauconite *abundance* varies considerably as a function of sea-level changes and can be used to delineate systems tracts and parasequences. The following chapter focuses on the relationship between sequence stratigraphic packages and glauconite *morphotypes*, color, and chemistry.

6.0 CHARACTER OF GLAUCONITE

6.1 Introduction

As noted above, glauconite is nearly ubiquitous throughout the study section, but its abundance varies significantly between systems tracts and parasequences. The goal of this chapter is to examine variations in the character of glauconite through the section. This includes modes of glauconite occurrence, color, chemistry, and x-ray diffraction signature.

6.2 Modes of Glauconite Occurrence

Glauconite in the study section occurs mainly as distinct grains of various morphotypes for which original precursor grains are not readily apparent. It also occurs as coatings on detrital grains, as a product of skeletal grain replacement, and locally as part of fine-grained matrix.

6.2.1 Glauconite Morphotypes

Examination of sand samples under a binocular microscope indicates that most previously recognized glauconite grain morphotypes (Table 1) are represented in the study section. These include capsule-shaped, mammillated, lobate, ovoidal, vermicular, tabular, and composite grains (Fig. 21). Capsule-shaped grains are crudely cylindrical and exhibit relatively deep, commonly transverse surface cracks (Fig. 21A). Mammillated grains are highly irregular grains with numerous surface protuberances separated by cracks (Fig. 21B). Lobate grains are similar to mammillated grains, but have deeper

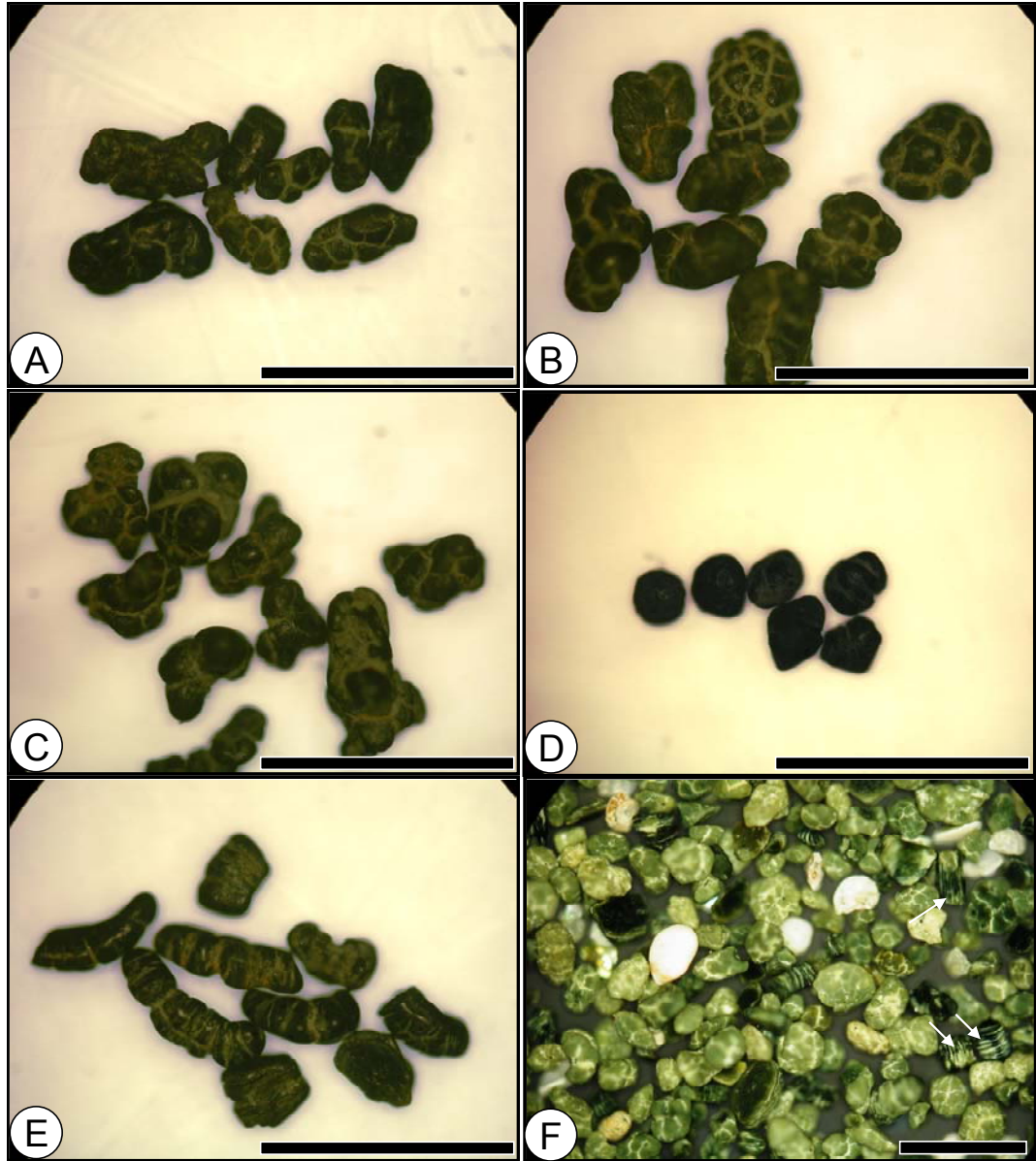


Figure 21 – Different grain morphotypes as viewed in reflected light. (A) Capsule-shaped grains. (B) Mammillated grains. (C) Lobate grains. (D) Ovoidal grains. (E) Vermicular grains. (F) Tabular grains (arrows). Bar scales are ~ 1 mm long.

cracks (Fig. 21C). Cracks observed on capsule-shaped, mammillated, and lobate grains typically are partially healed with lighter green glauconite. Ovoidal grains are equidimensional and exhibit relatively smooth, rounded surfaces (Fig. 21D). Vermicular grains generally are elongate, curved, and are longitudinally segmented (Fig. 21E). Tabular grains generally are flat or platy and commonly exhibit smooth surfaces (Fig. 21F). Composite grains are aggregates of detrital grains cemented by a glauconitic matrix.

Identification of grain morphotypes generally requires three-dimensional views and, hence, is difficult in thin-section analysis. Although many glauconite grains observed in two-dimensional thin-section views could not be classified based on their two-dimensional geometry, most could be placed into four morphological categories. These are mammillated/lobate grains (Figs. 22A,C, 23A,B), capsule-shaped grains (Figs. 22A,B, 23C), vermicular/tabular grains (Figs. 22C, 23D), and ovoidal grains (Fig. 22D). As viewed in thin section, the interiors of most glauconite grains are characterized by homogeneous, randomly oriented microcrystalline aggregates. In backscattered scanning electron images generated prior to microprobe analysis, compositional zonation is observed in some glauconite grains (Fig. 23).

The normalized percentages of the four glauconite grain types recognized in thin section are given in the Table 6. These data are plotted versus stratigraphic height and total glauconite abundance in Figures 24 and 25. Overall, mammillated/lobate and capsule-shaped grains are the most common grain types observed. The relative abundances of these grains types generally are proportional to total glauconite content (Fig. 24). Both types are relatively rare in the lowstand incised valley fill (Clayton sand)

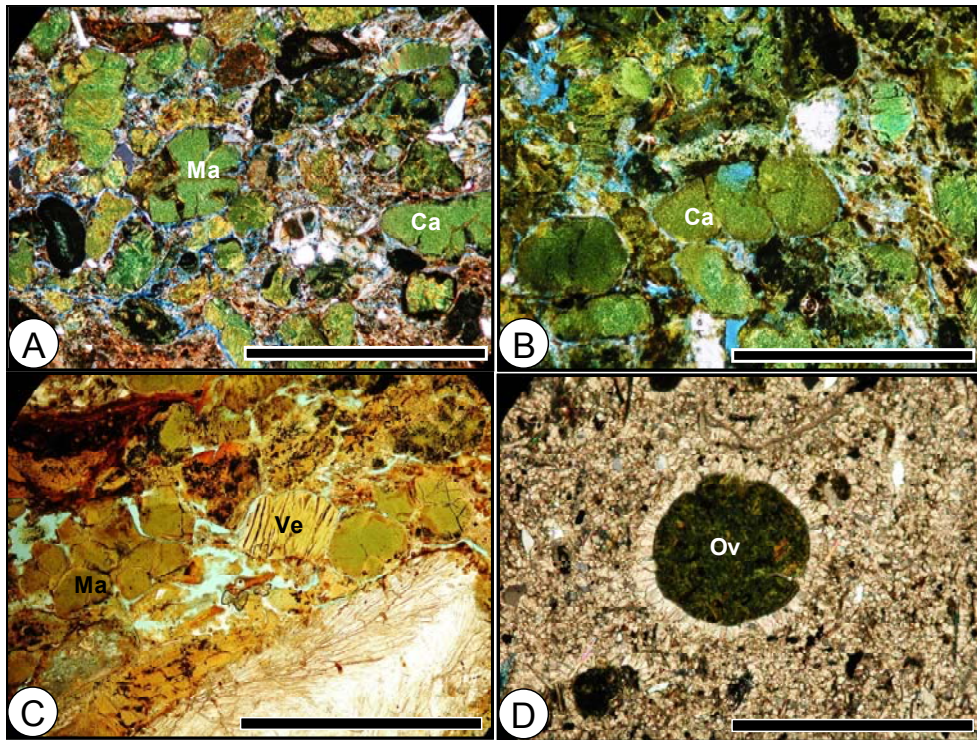


Figure 22 – Photomicrographs showing different glauconite grain types. (A) Mammillated/lobate (Ma) and capsule-shaped (Ca) grains. (B) Capsule-shaped grains (Ca). (C) Vermicular/tabular (Ve) and mammillated/lobate (Ma) grains. (D) Ovoidal (Ov) grain. Bar scales are ~ 1 mm long.

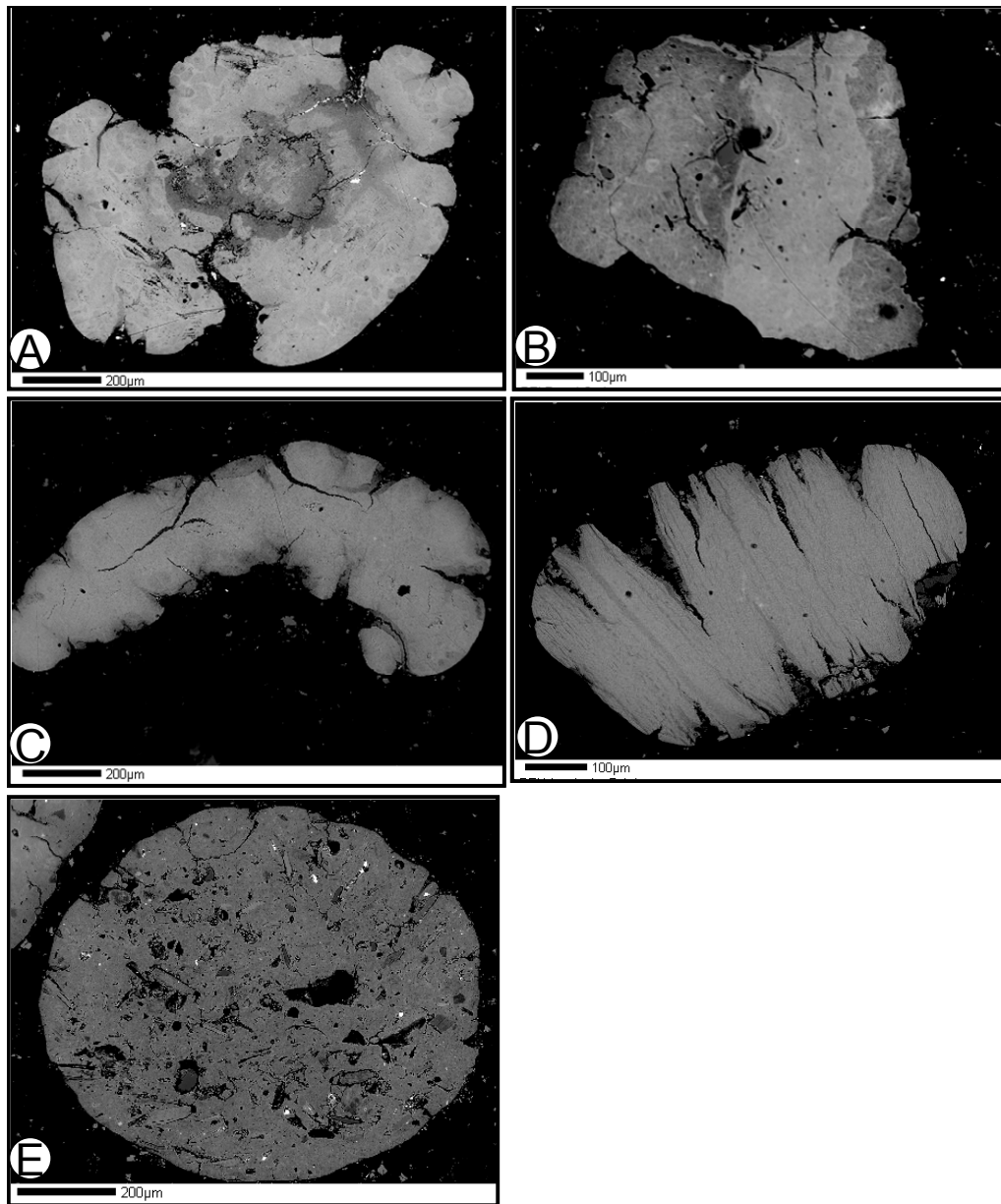


Figure 23 – Backscattered electron images of different glauconite morphotypes. (A and B) Mammillated/lobate grains revealing compositional zonation. Brighter areas in the grains represent higher average atomic number and Fe content. (C) Capsule-shaped grain. (D) Vermicular/tabular grain. (E) Ovoidal grain.

Table 6 – Normalized percentages of assignable glauconite grain types derived from point-count data.

Sample name	Height in section (cm)	% Mammilated/Lobate	% Vermicular/Tabular	% Capsule-shaped	% Ovoidal
MC-2-0-5	20.5	20.0	6.7	0.0	73.3
MC-3-28-35	94.5	19.0	2.4	9.5	69.0
MC-4-12-17	118	25.0	25.0	25.0	25.0
MC-5-25-35	153	5.1	20.5	7.7	66.7
MC-6-18-25	184.5	0.0	16.7	0.0	83.3
MC-8-0-5	215.5	3.8	15.4	0.0	80.8
MC-8-10-20	228	6.9	10.3	0.0	82.8
MC-8-20-25	235.5	39.6	16.7	10.4	33.3
MC-8-30-40	248	53.3	5.6	39.3	1.9
MC-9-0-3	254.5	52.6	21.6	21.6	4.3
MC-9-13-25	273	56.7	2.2	41.0	0.0
MC-10-0-15	285.5	63.9	6.9	26.4	2.8
MC-11-0-1	293.5	66.4	7.8	25.8	0.0
MC-11-5-7	299	51.9	6.2	42.0	0.0
MC-11-12-18	308	36.4	27.3	36.4	0.0
MC-11-24-29	319	60.7	8.9	30.4	0.0
MC-12-3-17	333	75.9	4.6	19.5	0.0
MC-13a-10-20	368	41.7	45.8	8.3	4.2
MC-13a-35-45	393	30.0	70.0	0.0	0.0
MC-13a-45-55	403	44.4	11.1	11.1	33.3
MC-13a-55-65	413	10.5	57.9	0.0	31.6
MC-13b-70-75	425.5	0.0	100.0	0.0	0.0
MC-13c-115-125	473	52.3	17.4	25.6	4.7
MC-13c-140-147	498	41.5	27.7	27.7	3.1
MC-13c-147-153	503	31.9	41.5	6.4	20.2
MC-13c-160-162	514	25.4	47.6	17.5	9.5
MC-14-0-15	525.5	22.2	66.7	11.1	0.0

Table 6 – continued.

Sample name	Height in section (cm)	% Mammilated/Lobate	% Vermicular/Tabular	% Capsule-shaped	% Ovoidal
MC-15-3-7	538	30.9	41.2	16.5	11.3
MC-15-60-68	597	0.0	20.0	20.0	60.0
MC-15-65-72	601.5	0.0	0.0	0.0	0.0
MC-15-75-80	610.5	12.5	62.5	0.0	25.0
MC-15-85-90	620.5	77.8	22.2	0.0	0.0
MC-16b-bottom	634	0.0	100.0	0.0	0.0
MC-16b-top	653	0.0	0.0	0.0	100.0
MC-16c-35-42	661.5	0.0	100.0	0.0	0.0
MC-16d-42-47	667.5	14.3	85.7	0.0	0.0
MC-16f-53-72	686	0.0	66.7	0.0	33.3
MC-16g-72-78	698	0.0	100.0	0.0	0.0
MC-16h-78-92	708	0.0	100.0	0.0	0.0
MC-17-0-15	728.5	38.8	40.0	20.0	1.3
MC-17-15-20	738.5	40.0	46.7	8.9	4.4
MC-17-20-25	743.5	65.1	30.2	4.7	0.0
MC-17-70-80	796	0.0	100.0	0.0	0.0
MC-17-80-90	806	0.0	100.0	0.0	0.0
MC-17-90-95	813.5	34.6	53.8	7.7	3.8
MC-18-5-20	828.5	33.3	63.0	3.7	0.0
MC-19-47-55	887	14.3	74.3	8.6	2.9
MC-20-0-5	928.5	28.6	57.1	14.3	0.0
MC-22-0-13	971.5	0.0	0.0	0.0	0.0
MC-23-5-10	991.5	50.0	50.0	0.0	0.0
MC-23-15-20	1001.5	0.0	0.0	0.0	0.0
MC-24-0-12	1015	16.7	83.3	0.0	0.0
MC-25-5-10	1028.5	0.0	0.0	0.0	0.0
MC-26-0-8	1045	0.0	0.0	0.0	0.0
MC-27-20-24	1071	0.0	0.0	0.0	0.0
MC-28-1-11	1079.5	0.0	0.0	0.0	0.0
MC-29-15-20	1102.5	0.0	0.0	0.0	0.0
MC-30-1-8	1108.5	0.0	0.0	0.0	0.0

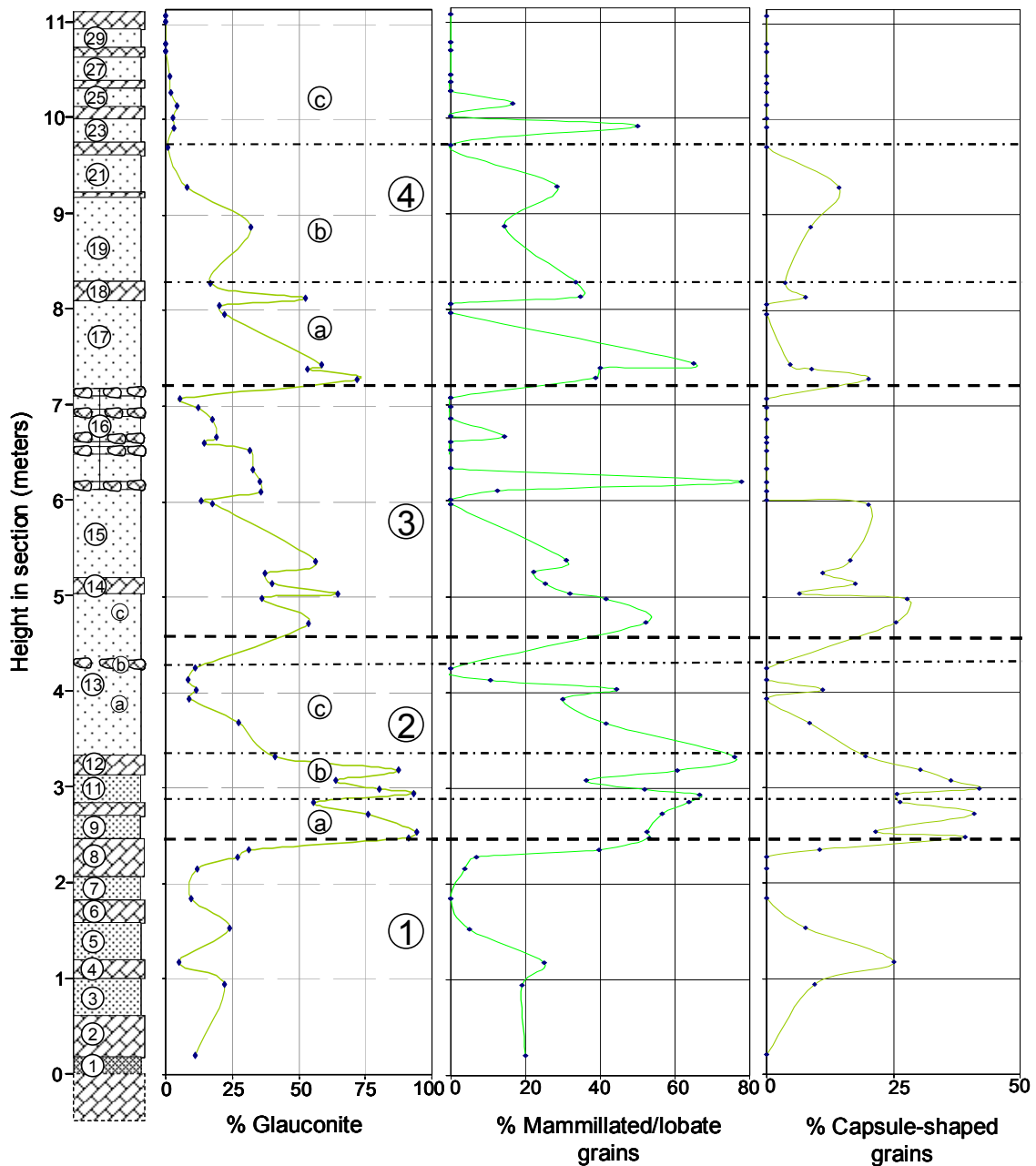


Figure 24 – Percent total glauconite, percent mammillated/lobate grains, and percent capsule-shaped grains in the study section. Dashed and dot-dashed lines define boundaries of parasequences (1-4) and mini-cycles (2a-c, 4a-c), respectively. Section legend is shown in figure 6.

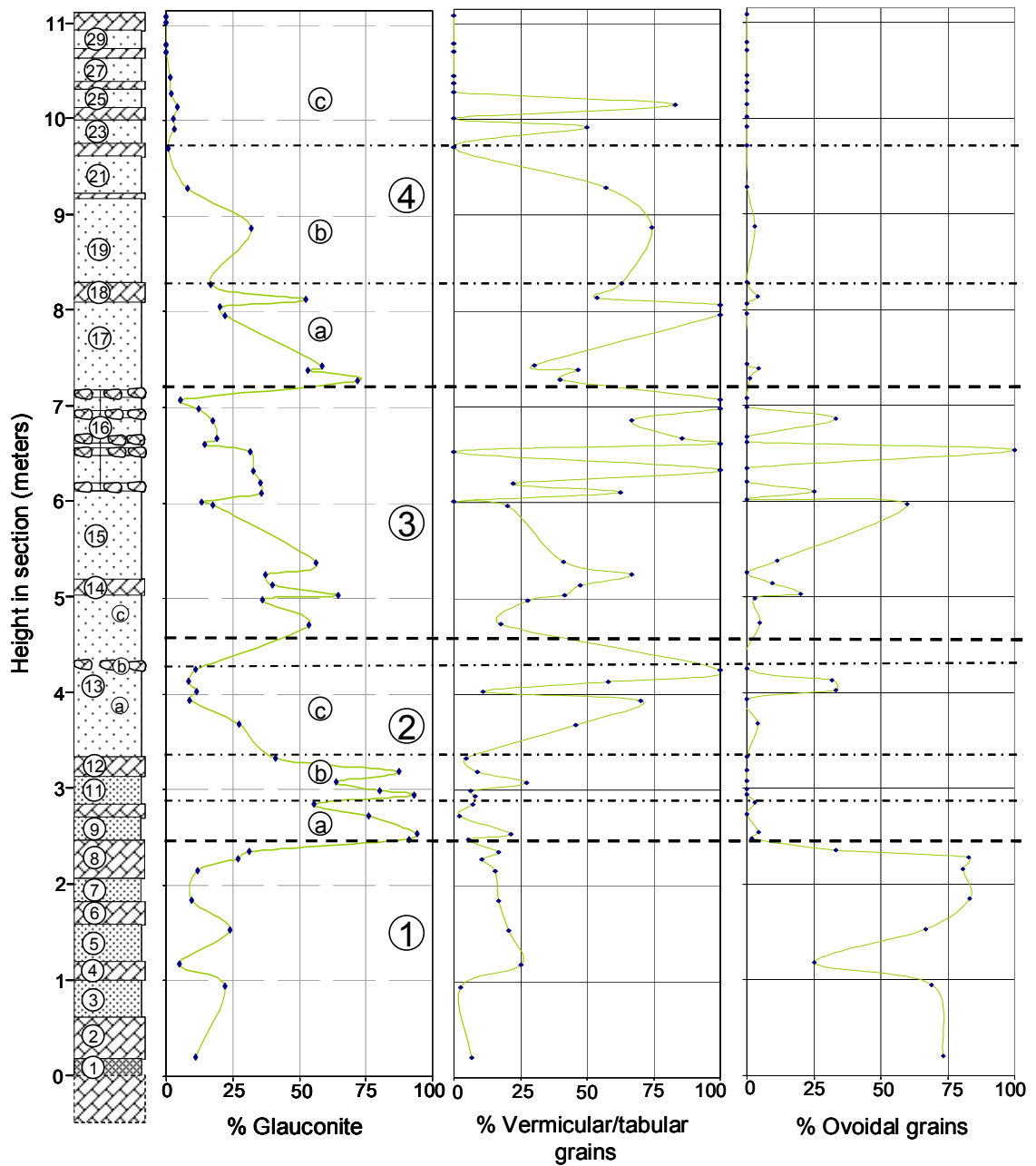


Figure 25 – Percent total glauconite, percent vermicular/tabular grains, and percent ovoidal grains in the study section. Dashed and dot-dashed lines define boundaries of parasequences (1-4) and mini-cycles (2a-c, 4a-c), respectively. Section legend is shown in figure 6.

and transgressive system tract (units 1-8) but increase abruptly to maxima in the condensed section. In general, both types progressively decrease in relative abundance upward through the highstand systems tract. However, abundances vary systematically through parasequences 2 through 4. Within each parasequence, relative abundances of mammillated/lobate and capsule-shaped grains are highest in the lower parts and decrease upwards (Fig. 24).

Distribution of vermicular/tabular grains is opposite of that of mammillated/lobate and capsule-shaped grains. Relative abundances of vermicular/tabular grains increase upward through the section in general, and upward through each parasequence. The latter pattern is most obvious in parasequences 2 and 3 (Fig. 25).

Ovoidal grains have a very different distribution (Fig. 25). They are the dominant glauconite grain type in the lowstand incised valley fill (Clayton sand). However, with the exception of isolated horizons in the highstand systems tract (e.g., in parasequence 3) they are rare or absent altogether in the remainder of the section (Fig. 25).

6.2.2 Glauconite-Coated Grains

In thin section, glauconite is observed as grain coatings on detrital grains, principally quartz (Fig. 26). Coatings vary in thickness and may be continuous or discontinuous around grain perimeters. Glauconite-coated quartz grains also commonly contain very thin glauconite-filled fractures (Fig. 26).

The relative abundances of glauconite-coated detrital grains in point-counted samples are provided in Table 7, and the stratigraphic distribution of these grains is shown in Figure 27. Relative abundances of coated grains generally vary with total

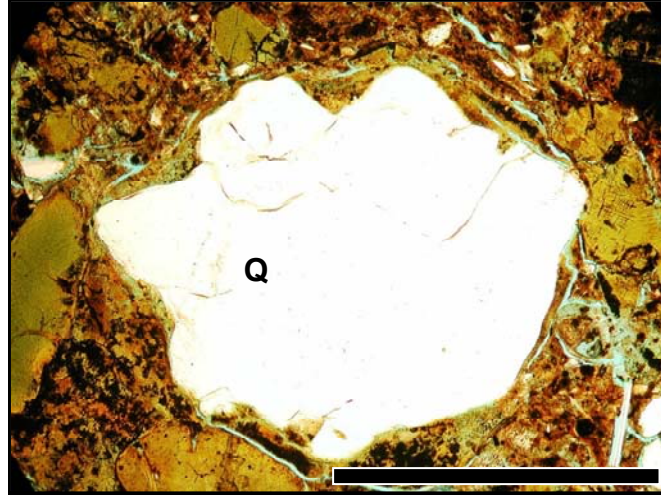


Figure 26 – Photomicrograph showing glauconite coatings on and fracture fillings in quartz (Q). Bar scale is ~ 1 mm long.

Table 7 – Abundances of glauconitized skeletal grains and glauconite-coated detrital grains based on point-count analysis.

Sample name	Height in section (cm)	% Coated detrital grains	% Replaced Skeletal grains
MC-2-0-5	20.5	0.3	0.6
MC-3-28-35	94.5	7.3	1.4
MC-4-12-17	118	0.0	0.0
MC-5-25-35	153	2.9	0.8
MC-6-18-25	184.5	0.3	1.1
MC-8-0-5	215.5	0.6	0.8
MC-8-10-20	228	0.0	1.6
MC-8-20-25	235.5	6.9	1.9
MC-8-30-40	248	2.4	12.3
MC-9-0-3	254.5	4.8	12.5
MC-9-13-25	273	1.7	6.9
MC-10-0-15	285.5	1.5	4.5
MC-11-0-1	293.5	10.2	16.4
MC-11-5-7	299	11.5	10.8
MC-11-12-18	308	6.0	12.7
MC-11-24-29	319	3.6	8.8
MC-12-3-17	333	0.3	6.6
MC-13a-10-20	368	2.8	1.5
MC-13a-35-45	393	0.0	0.0
MC-13a-45-55	403	0.0	0.3
MC-13a-55-65	413	0.0	0.0
MC-13b-70-75	425.5	0.0	0.0
MC-13c-115-125	473	6.7	0.3
MC-13c-140-147	498	2.9	1.4
MC-13c-147-153	503	14.4	0.9
MC-13c-160-162	514	6.7	0.3
MC-14-0-15	525.5	2.0	2.0

Table 7 – Continued.

Sample name	Height in section (cm)	% Coated detrital grains	% Replaced Skeletal grains
MC-15-3-7	538	4.0	2.3
MC-15-60-68	597	0.6	0.0
MC-15-65-72	601.5	2.0	0.0
MC-15-75-80	610.5	9.2	2.8
MC-15-85-90	620.5	0.3	0.3
MC-16b-bottom	634	12.3	2.6
MC-16b-top	653	18.5	1.3
MC-16c-35-42	661.5	0.0	0.3
MC-16d-42-47	667.5	4.4	3.7
MC-16f-53-72	686	5.3	0.0
MC-16g-72-78	698	0.0	0.0
MC-16h-78-92	708	2.6	0.0
MC-17-0-15	728.5	17.0	5.4
MC-17-15-20	738.5	15.1	2.4
MC-17-20-25	743.5	16.8	5.4
MC-17-70-80	796	6.2	1.1
MC-17-80-90	806	5.9	0.7
MC-17-90-95	813.5	10.6	5.3
MC-18-5-20	828.5	0.4	0.8
MC-19-47-55	887	5.8	2.2
MC-20-0-5	928.5	0.0	0.0
MC-22-0-13	971.5	0.0	0.0
MC-23-5-10	991.5	0.0	0.9
MC-23-15-20	1001.5	2.6	0.0
MC-24-0-12	1015	2.0	0.0
MC-25-5-10	1028.5	0.3	0.3
MC-26-0-8	1045	1.3	0.0
MC-27-20-24	1071	0.0	0.0
MC-28-1-11	1079.5	0.0	0.0
MC-29-15-20	1102.5	0.0	0.0
MC-30-1-8	1108.5	0.0	0.0

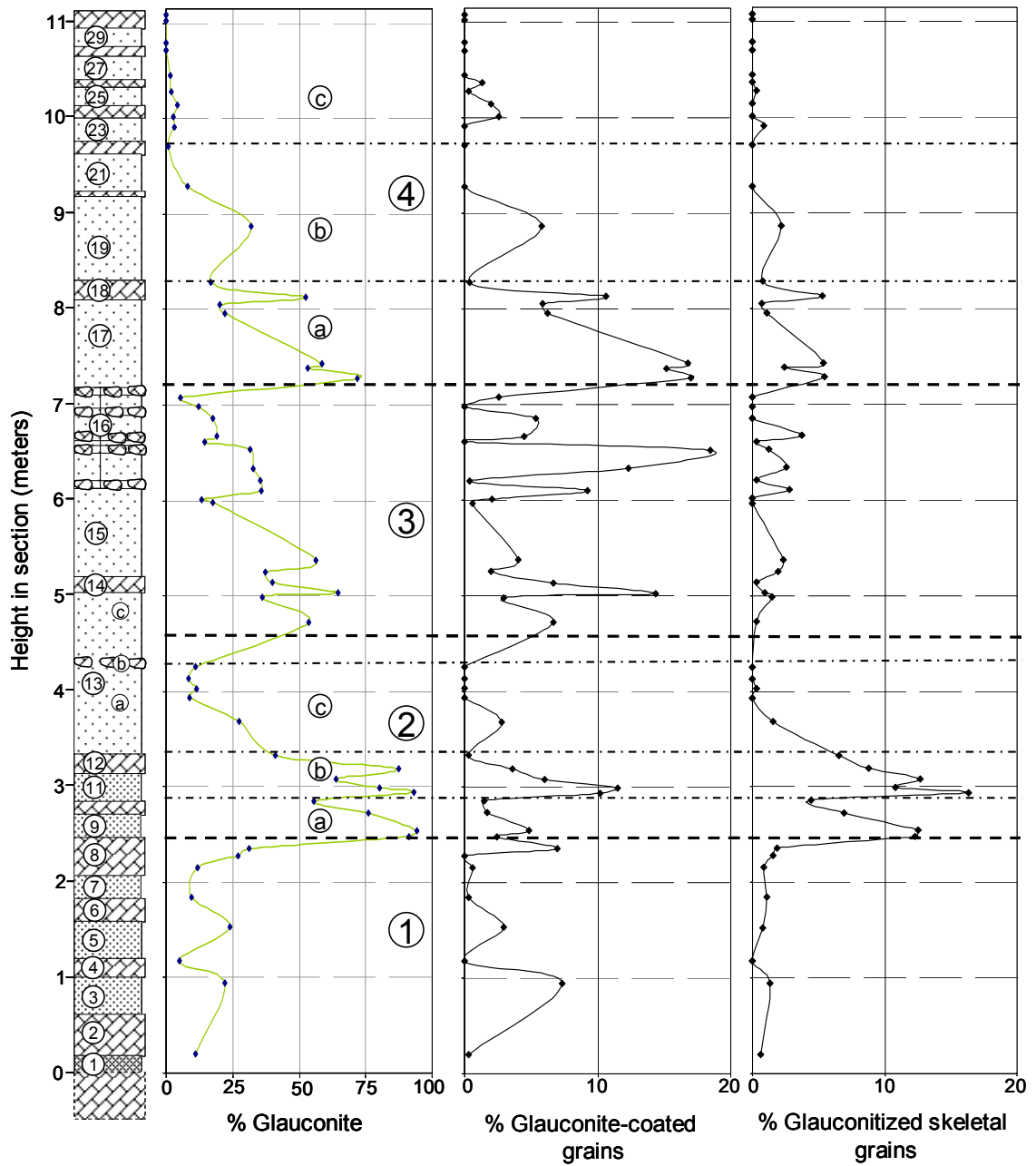


Figure 27 – Percent total glauconite, percent glauconite-coated detrital grains, and percent glauconitized skeletal grains in the study section. Dashed and dot-dashed lines define boundaries of parasequences and mini-cycles, respectively. Section legend is shown in figure 6.

glaucinite content. Coated grains are most common in the lower parts of parasequences and of mini-cycles therein.

6.2.3 Glaucinitized Skeletal Grains

A variety of originally carbonate skeletal fragments have been partly or wholly replaced by glauconite (Fig. 28). These include foraminifers (Fig. 28A) and bivalve (Fig. 28B), bryozoan (Fig. 28C), and echinoid spine (Fig. 28D) fragments. In addition to replacement of original calcite, glauconite also commonly fills intraparticle pore space (e.g., foraminifer chambers, stereom, etc.) within these carbonate grains.

The relative abundances of glauconitized skeletal grains in point-counted samples are provided in Table 7, and the stratigraphic distribution of these grains is shown in Figure 27. As with coated grains, the abundance of replaced skeletal fragments generally varies with total glauconite content. Notably, peak abundances (>10% of rock volume) are associated with the condensed section, which contains the greatest percentage of skeletal fragments in general (Fig. 16).

6.2.4 Relationships to Systems Tracts and Parasequences

Observations described above indicate that the relative abundances of glauconite grain varieties do vary with inferred changes in sea-level and sedimentation rates and, hence, can be of use in delineating systems tracts and parasequences. Capsule-shaped, mammillated, and lobate grain morphotypes, all of which contain glauconite-healed cracks, are regarded as relative mature varieties and are indicative of relatively slow sedimentation rates. In contrast, vermicular grains are considered to be indicative of lower maturity (Huggett and Gale, 1997) and, hence, limited sediment starvation. As expected, the relative abundances of these grain types (Figs. 24 and 25) clearly reflect

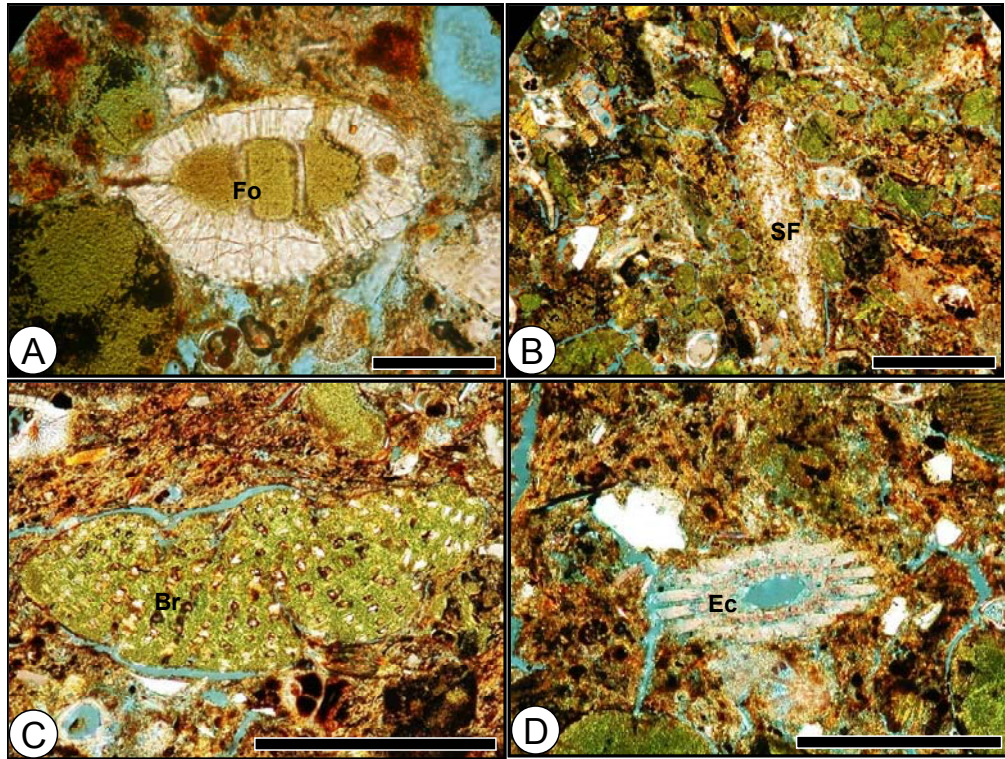


Figure 28 – Photomicrographs showing glauconitized fossil fragments. (A) Glauconite infilling and partially replacing foraminifer (Fo). (B) Glauconite replacing shell fragment (SF). (C) Glauconitized bryozoan (Br). (D) Echinoderm fragment (echinoid spine) (Ec) partially replaced and infilled with glauconite. Bar scales are ~ 0.5 mm long.

decreasing maturity through the highstand system tract in general and upward through each parasequence.

Ovoidal grains may acquire their shape in several ways. They may reflect the reworking and rounding of other grain morphotypes (detrital glauconite) or inherit their shape from precursor grains (Triplehorn, 1966; Hugget and Gale, 1997; Amorosi, 1997). The abundance of ovoidal grains in the incised valley fill (unit 1, Clayton sand) and the transgressive systems tract (units 2-8) likely reflect reworking of glauconite grains in relatively shallow settings during early stages of sea-level rise. Other peaks in abundance of ovoidal grains (i.e., in units 15 and 16) also may reflect detrital glauconite associated with reworking near the upper part of parasequence 2. Alternatively, these peaks may reflect inherited morphologies related to glauconite infilling of foram chambers or other fossil cavities or replacement of fecal pellets.

Glauconitized skeletal fragments are most abundant in the condensed section. However, the abundances of these and glauconite-coated detrital grains are generally proportional to total glauconite content and to abundances of relatively mature grain morphotypes. Therefore, common glauconitized carbonate grains and coated detrital grains also appear to be indicative of significant sediment starvation and could be employed in delineating sequence stratigraphic packages.

6.3 Glauconite Grain Color

Glauconite color was assessed based on observations of sand fractions under reflected light and of thin sections viewed under plane-polarized transmitted light. Although quantitative color analyses of glauconite-grain separates may be a productive pursuit for future work, only qualitative observations were made for the current study.

Although grains in the upper oxidized part of the section tend to be reddish-brown, most glauconite grains in the study interval are various shades of light to dark green. Shades of green may vary within a single grain (e.g., glauconitic fracture fills tend to be lighter green than glauconite host grains; see Fig. 21) and among glauconite grains within a single sample (Fig. 21F). Nonetheless, some general color trends can be discerned throughout the study section and within parasequences. Glauconite grains throughout parasequences 1 and 2 are generally medium to dark green. However, glauconite grains generally change from medium to dark green to light green to light greenish brown from the bases to the tops of parasequences 3 and 4 (Figs. 27, 30). Hence, general glauconite color does appear to reflect sea-level controlled changes in sedimentation rate and glauconite maturity.

6.4 Glauconite Chemistry

Ten grains from each of thirteen samples were subjected to microprobe analysis. Three samples fall within the top of parasequence 1, five samples are from parasequence 2, and five samples are from parasequence 3. Average abundances of major oxides for each sample are listed in Table 8. As expected, the data show a strong positive correlation between FeO and K₂O and inverse relationships between Al₂O₃ and FeO and K₂O (Fig. 31).

K₂O contents of glauconite are plotted versus stratigraphic height in Figure 32. Averaged K₂O contents for twelve of the samples fall between 6 and 8%, indicating that the glauconite is evolved. The remaining sample, which is stratigraphically highest, has an average K₂O content of 4.8%, indicating slightly evolved glauconite. In the context of parasequences 2 and 3, K₂O contents are highest at the base and decrease significantly

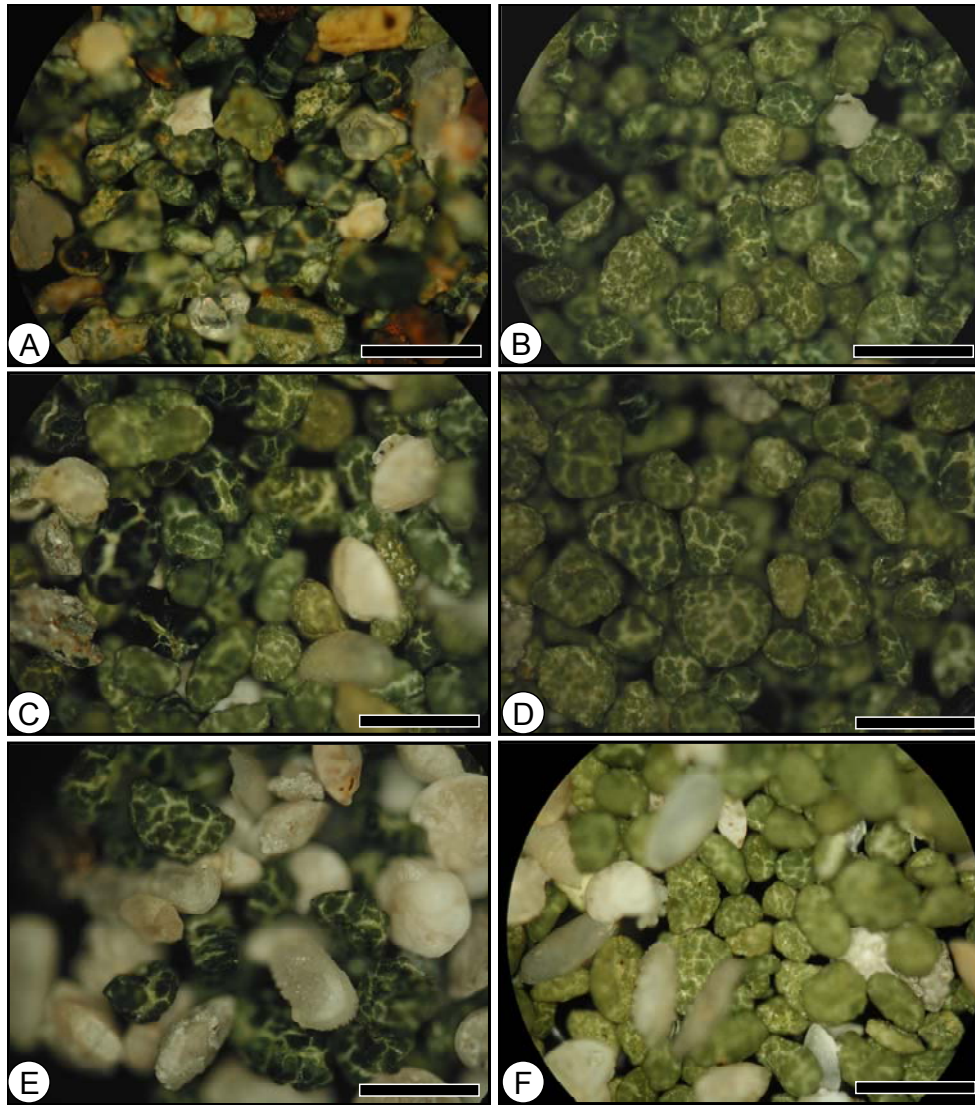


Figure 29 – Reflected light photographs showing color variation of glauconite grains in parasequences. (A) Bottom and (B) top of parasequence 2. (C) Bottom and (D) top of parasequence 3. (E) Bottom and (F) top of parasequence 4. Samples in A, B, C, D, E, and F are from unit 9, lower and upper parts of unit 13, unit 16, unit 17, and unit 23, respectively. Bar scales are ~ 1 mm long.

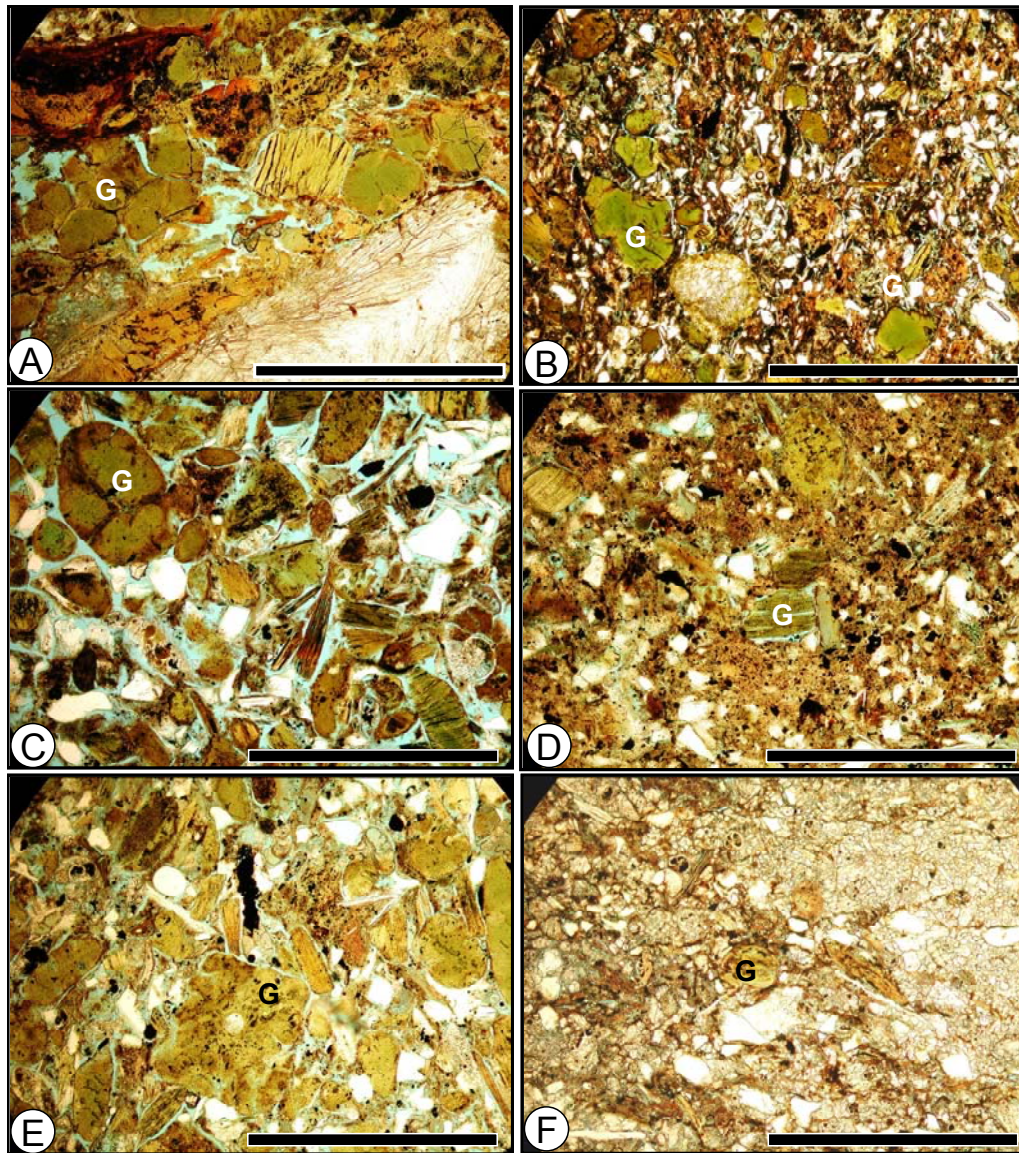


Figure 30 – Plane-light photomicrographs showing color variation of glauconite grains in parasequences. (A) Bottom and (B) top of parasequence 2. (C) Bottom and (D) top of parasequence 3. (E) Bottom and (F) top of parasequence 4. Samples in A, B, C, D, E, and F are from unit 9, lower and upper parts of unit 13, unit 16, unit 17, and unit 23, respectively. Bar scales are ~ 1 mm long.

Table 8 – Average abundances (weight percent) of major oxides in glauconite grains as determined by microprobe analysis.

Sample name	Sample no.	Height in section (cm)	SiO ₂ %	Al ₂ O ₃ %	FeO %	MgO %	CaO %	Na ₂ O %	K ₂ O %	Total
MC-8-0-5	13	215.5	47.07	5.87	24.30	3.82	0.44	0.02	6.35	87.87
MC-8-10-20	14	228	49.55	4.33	25.41	4.12	0.31	0.02	7.56	91.29
MC-8-20-25	15	235.5	50.10	5.41	24.25	3.59	0.58	0.02	6.72	90.71
MC-8-30-40	16	248	49.00	4.04	25.31	3.77	0.40	0.02	7.16	89.69
MC-9-0-3	17	254.5	49.59	4.81	25.15	4.03	0.63	0.01	7.29	91.51
MC-9-13-25	18	273	47.43	4.50	25.89	3.93	0.64	0.01	7.18	89.57
MC-11-24-29	27	319	42.34	4.45	23.19	3.79	0.97	0.02	6.29	87.71
MC-13-45-55	33	403	50.73	7.49	22.58	3.95	1.02	0.01	6.20	91.98
MC-13c-147-153	43	503	48.00	4.80	24.60	3.90	0.65	0.03	7.20	89.22
MC-14-0-15	45	525.5	49.50	6.50	22.80	3.85	0.72	0.03	6.00	89.36
MC-15-8-13	47	543.5	47.20	5.70	24.50	3.96	0.86	0.01	6.40	88.75
MC-15-60-68	53	597	48.73	6.85	21.70	3.85	1.03	0.02	6.06	88.24
MC-16b-top	60	653	49.10	9.10	18.80	3.99	1.17	0.04	4.80	86.99

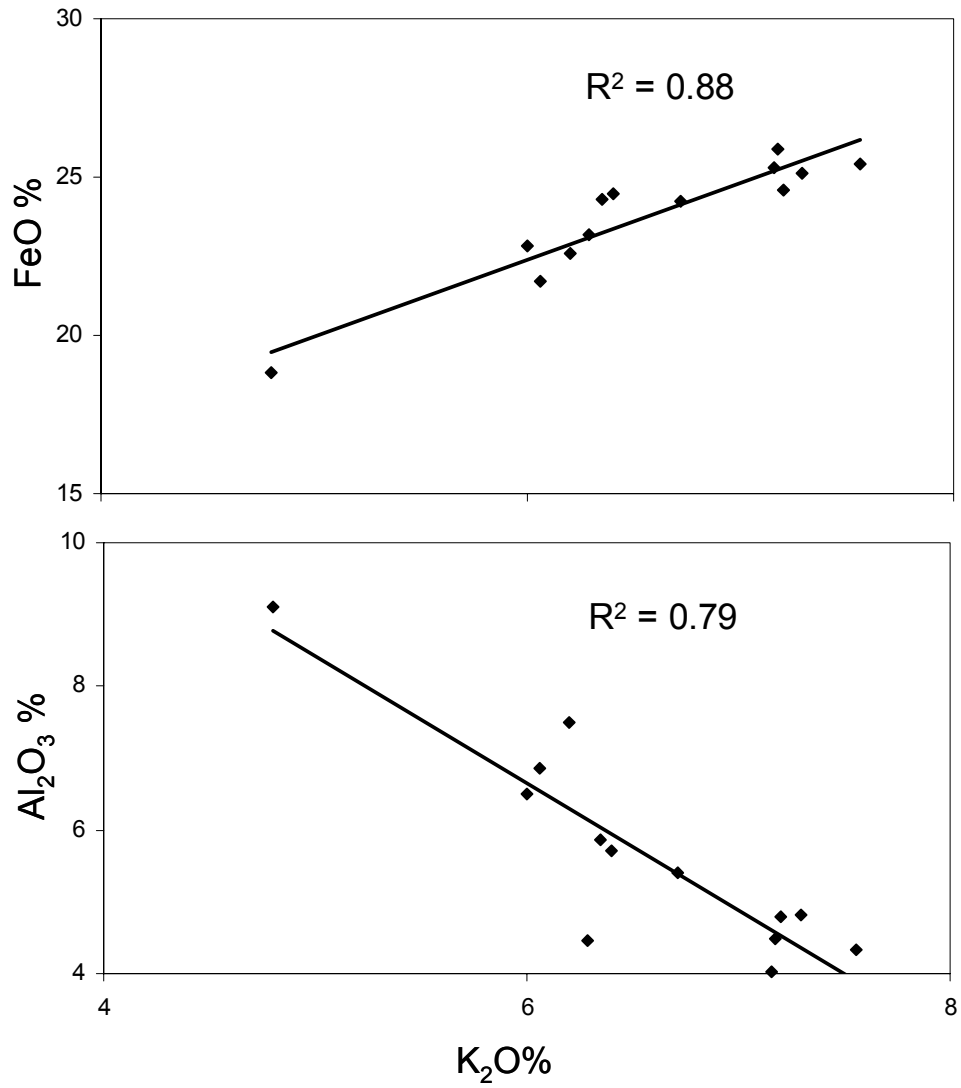


Figure 31 – Relationships among average oxide contents for thirteen glauconite samples

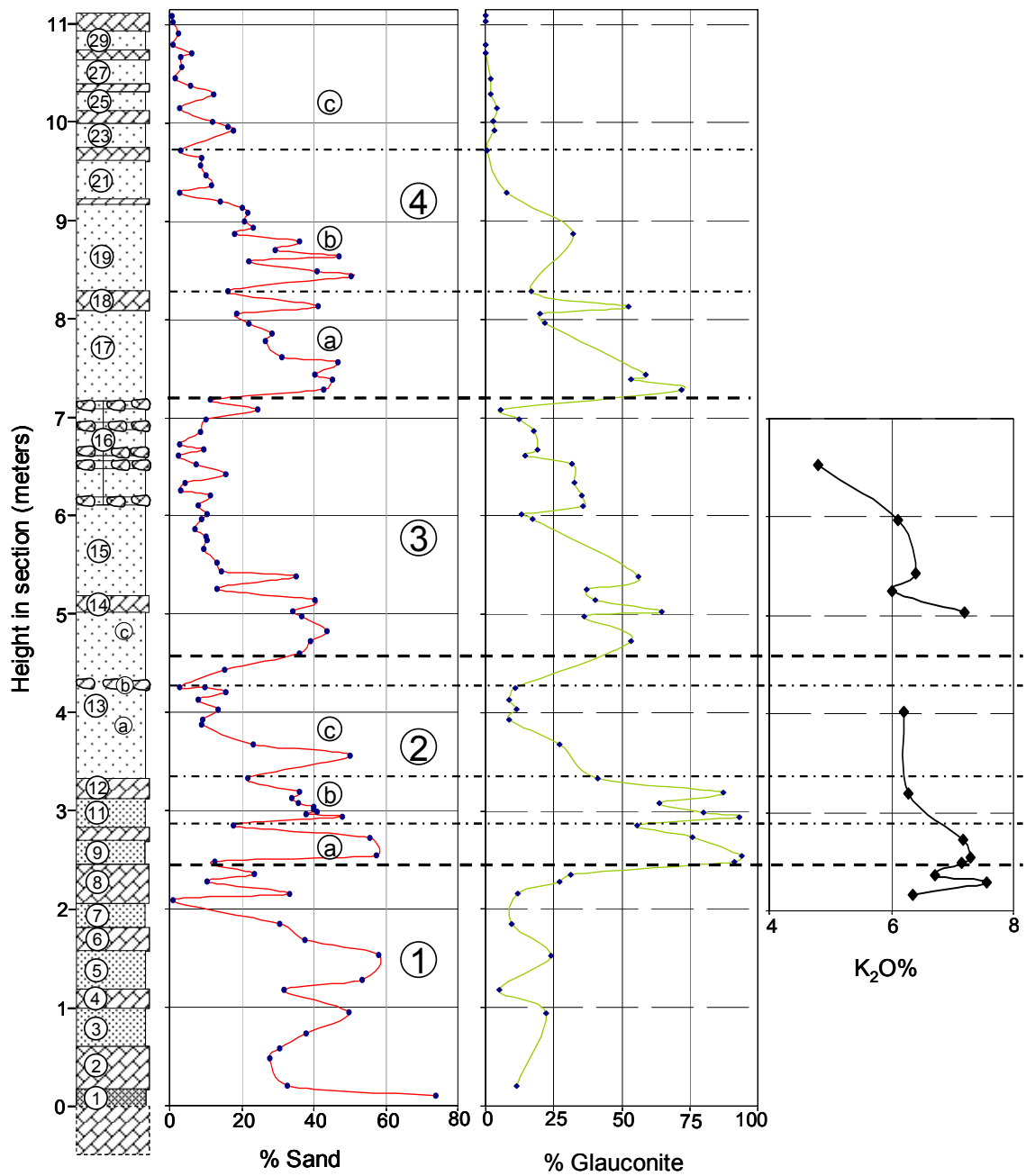


Figure 32 – Percent sand, percent glauconite, and K₂O % in the study section. Dashed and dot-dashed lines define boundaries of parasequences and mini-cycles, respectively. Section legend is shown in figure 6.

towards the middle and top. This is consistent with increasing sedimentation rate and associated reduction in glauconite maturity upward through the parasequences. Hence, the available data suggest that relative glauconite maturity based on elemental analysis may be of use in delineating parasequences.

6.7 XRD Analysis

A total of eight samples were selected for XRD analysis. Four of these samples are derived from the condensed section and lower part of the highstand systems tract (parasequence 2), while the other four are derived from higher in the section (parasequence 4).

Diffraction patterns for the first four samples, shown in ascending stratigraphic order in Figure 33, reveal little obvious differences from the bottom to the top of the parasequence 2. All are dominated by glauconite mica peaks centered at $\sim 10 \text{ \AA}$ and 4.52 \AA . Only the diffraction pattern for the upper sample has a weakly defined smectite peak (at $\sim 14 \text{ \AA}$). Diffraction patterns from the two middle samples manifest weak peaks (at $\sim 7.05 \text{ \AA}$) that may reflect berthierine, an Fe-rich clay commonly associated with glauconite.

Diffraction patterns for samples from parasequence 4 are shown in ascending stratigraphic order in Figure 34. No obvious differences can be detected through the parasequence. However, diffraction patterns for this parasequence do differ from those of parasequence 2. In general, peaks inferred to reflect smectite and berthierine are more prominent in parasequence 4 (see Fig. 35 for ready comparison).

X-ray diffraction results reveal little obvious change in structural state of glauconite through the two parasequences. This suggests that the XRD approach may not be sensitive enough to detect changes in sedimentation rate and glauconite maturity

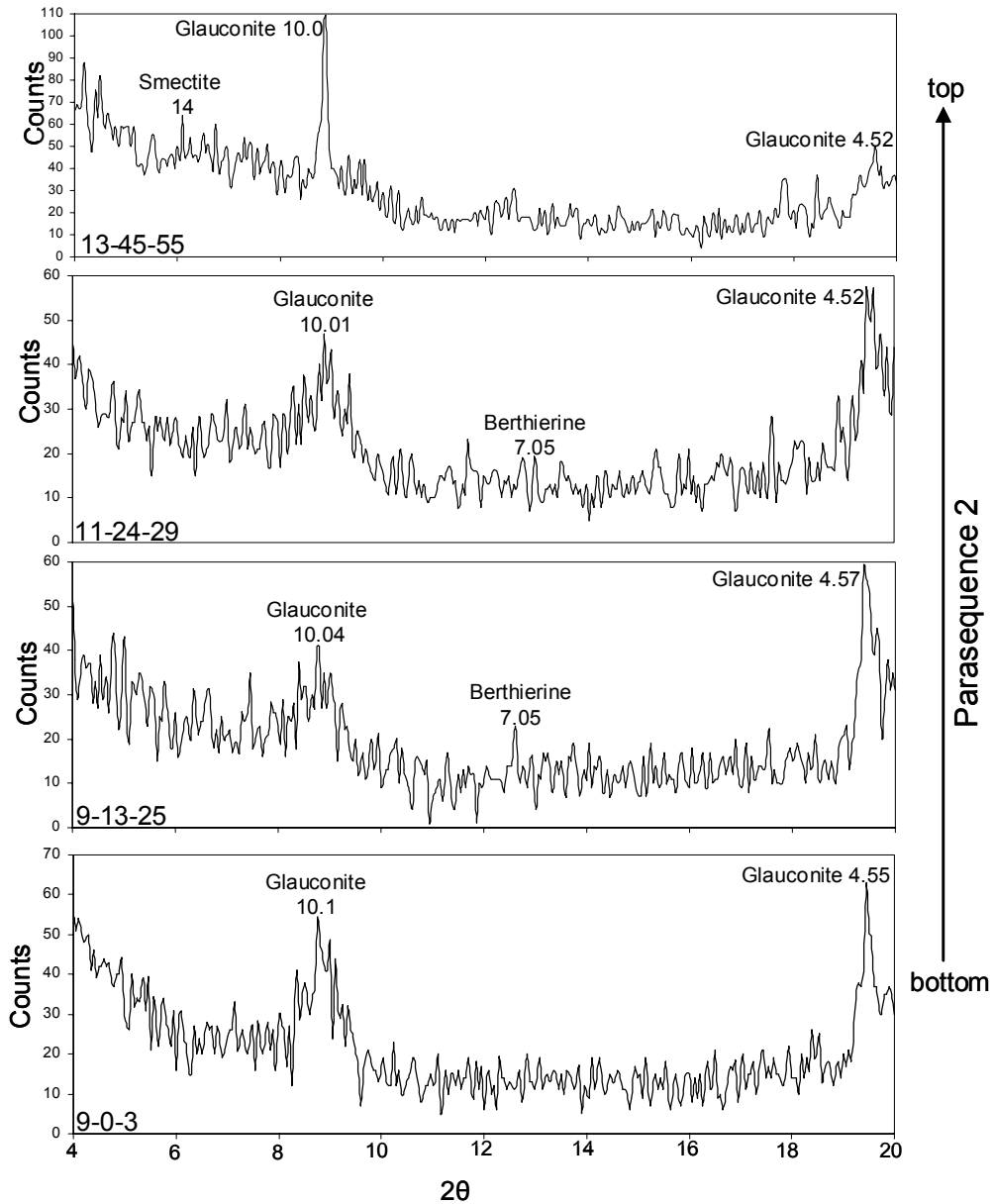


Figure 33 – X-ray diffractograms derived from the parasequence 2. Note changes in expression of glauconite peaks (at $\sim 10\text{\AA}$ and $\sim 4.55\text{\AA}$) and eventual appearance of smectite peak (at $\sim 14\text{\AA}$) towards the top of the parasequence. Fe-rich clay mineral berthierine often occurs within the glaucony facies.

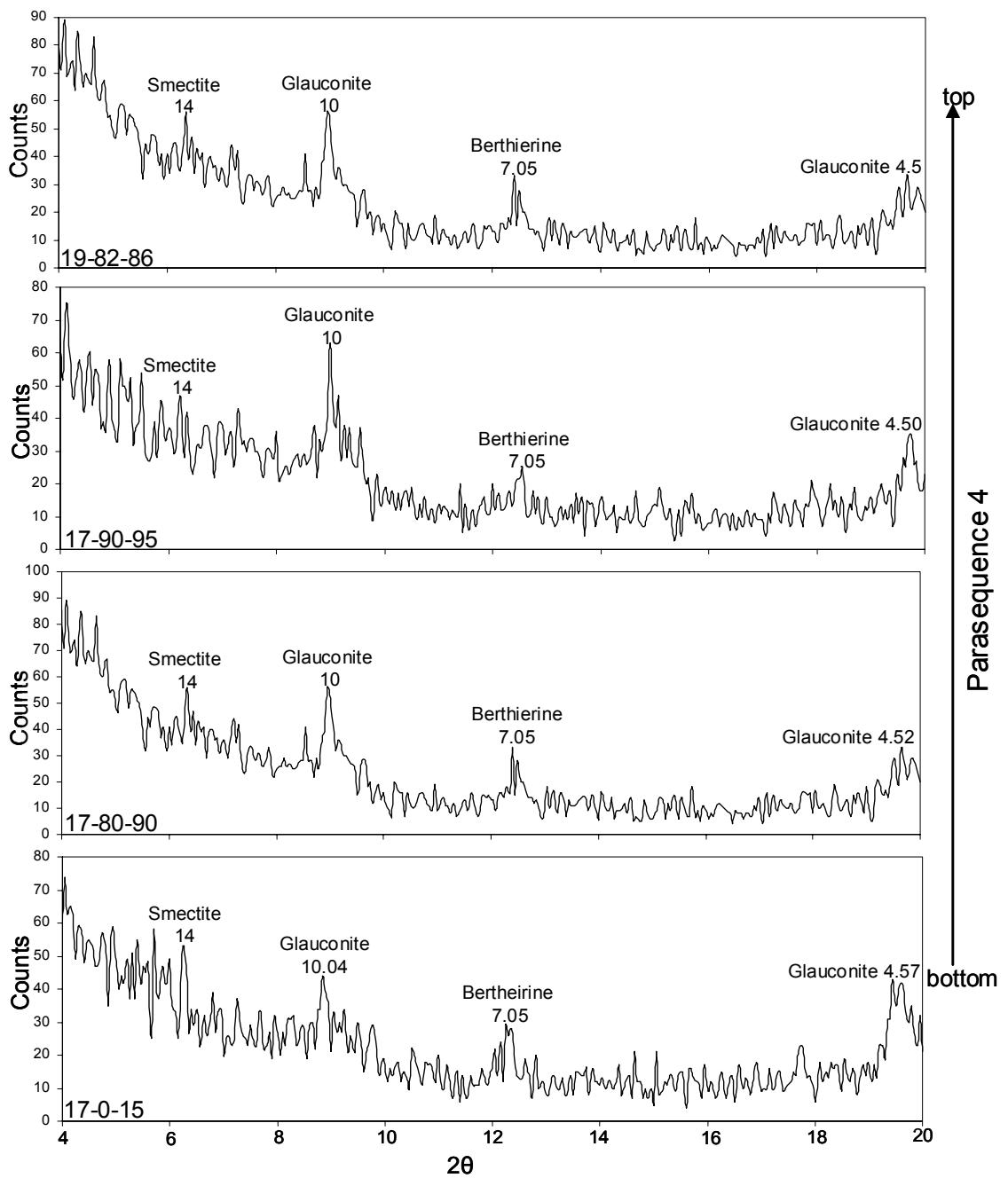


Figure 34 – X-ray diffractograms derived from the parasequence 4. Note the decrease of glauconite peak (at $\sim 4.55\text{\AA}$) peak and increase in smectite peak (at $\sim 14\text{\AA}$) towards the top of the parasequence.

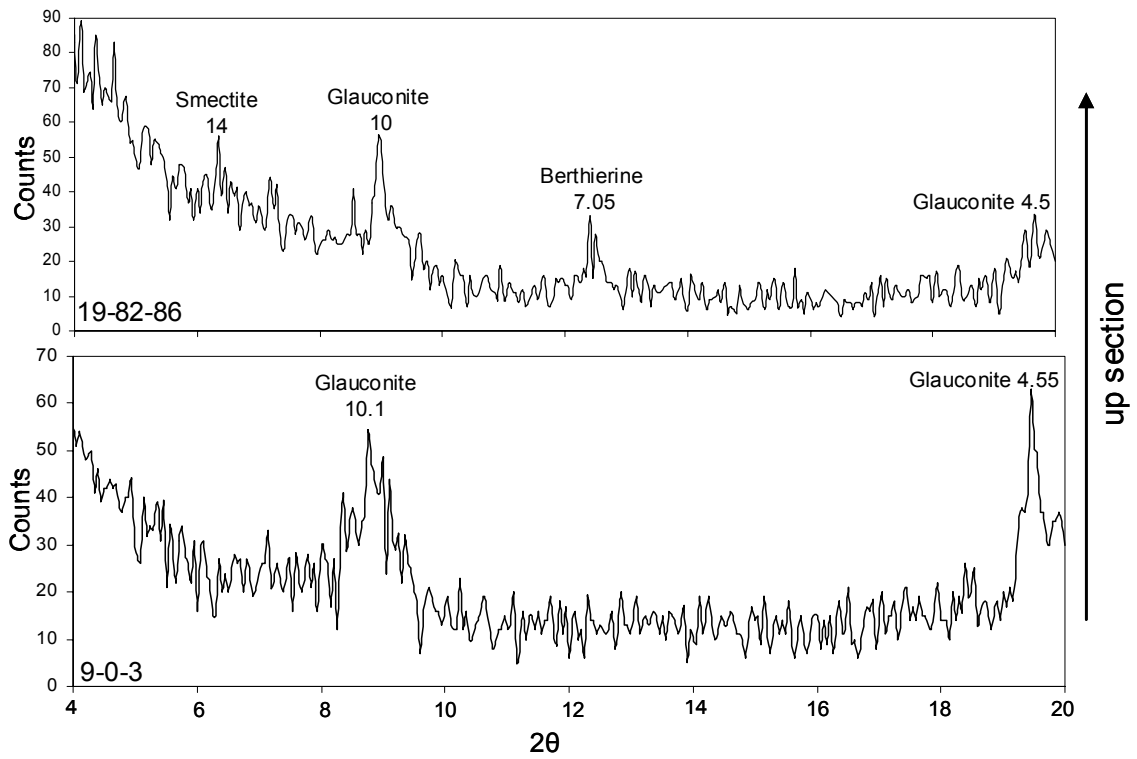


Figure 35 – X-ray diffractograms of samples from unit 9 (condensed section; base of parasequence 2) and unit 19 (middle of parasequence 4).

associated with 4th-order sea-level fluctuations, at least for those recorded in the parasequences of the study section. However, following previous authors (Odin and Matter, 1981; Hugget and Gale, 1997; Kelly and Web, 1999), relatively high smectite contents (and, perhaps, berthierine contents) in the upper part of the section (parasequence 4) may be interpreted to reflect limited glauconitization. In this sense, the XRD approach may help to detect larger differences in relative sedimentation rate that occur at the systems tract scale.

7.0 DISCUSSION

7.1 Role of Glauconite in Delineating Sequence Stratigraphic Packages

The main intent of this thesis was to test two hypotheses: (1) the abundance and maturity of glauconite vary systematically through a depositional sequence in response to sea-level dynamics and associated changes in sedimentation rate; and (2) the abundance and maturity of glauconite vary systematically through individual parasequences in response to short-term changes in sea-level. Both of these hypotheses are supported by studies of a passive-margin sequence in the Lower Paleocene Clayton Formation.

Glauconite abundance and character vary in a predictable way through systems tracts in the Clayton sequence. Lowstand incised valley fill deposits (Clayton sand) are characterized by low abundances of glauconite, most of which is detrital. The bulk of the transgressive systems tract contains low to moderate amounts of glauconite, including detrital and authigenic grains. The condensed section is characterized by peak abundances of highly mature glauconite grains, which occur in association with coarsest sands and abundant skeletal debris. The highstand systems tract is characterized by an upward decrease in glauconite abundance and maturity as indicated by changes in abundance of grain morphotypes, color, and chemistry.

The abundance and character of glauconite also varies in a systematic way through parasequences. Within the condensed section/highstand system tract, parasequences are expressed as asymmetrical cycles in glauconite abundance and maturity.

Bases of parasequences are dominated by relatively abundant, darker colored, K and Fe-rich, mature grains. Total glauconite abundances and K and Fe contents decrease, abundances of immature glauconite morphotypes increase, and glauconite becomes lighter in color progressively towards parasequence tops.

These observations indicate that detailed studies of glauconite can be used to decipher changes in sea-level and sedimentation rate. Use of glauconite is best applied to relatively condensed passive-margin shelf sequences wherein glauconite is common and other sedimentologic evidence for sea-level dynamics is absent.

7.2 Comparison with Previous Parasequence-Scale Studies

Previous studies of glauconite at the parasequence scale include those by Ruffell and Wach (1998) and Urash (2005). Ruffell and Wach (1998) described two different types of parasequences in the Cretaceous Lower Greensand Group in southern England, only one of which contains glauconitic sediments (their type A parasequences). They noted that glauconite is restricted to the bases of these coarsening upward sequences. Urash (2005) focused on parasequences in a condensed sequence of fossiliferous, glauconitic muddy sand in the Eocene Lisbon Formation, southern Alabama. He noted that parasequences are reflected by transitions from coarser, glauconitic-rich sands at bases to finer-grained, less glauconitic sands at tops. In both of these earlier studies, workers focused on general sedimentology and ichnology, and they did not address glauconite morphotypes or any other indicators of glauconite maturity. Hence, to date, the current study of the Clayton Formation represents the most in-depth analysis of glauconite at the parasequence scale.

7.3 Comparison with Foreland Basin Parasequences

As previously noted, parasequences are relatively conformable successions of genetically related beds or bedsets that reflect shorter-term sea-level fluctuations. They reflect upward shallowing and are bounded by marine flooding surfaces (Van Wagoner et al., 1988). In foreland basins, wherein sediment supply is relatively large, parasequences typically *coarsen* upwards in response to a seaward shift in shallow marine facies (e.g., Frey and Howard, 1990; Van Wagoner et al., 1990). The parasequences in the condensed passive-margin deposits described in the current study deviate from this general trend; Clayton parasequences are characterized by fining upward sequences. When viewed by itself, this textural pattern could be misinterpreted to reflect a progressive decrease in environmental energy or a deepening event. However, sediment textures in the Clayton Formation apparently do not reflect primary detrital grain size. Instead, sand fractions are composed primarily of authigenic glauconite. Hence, as previously noted by Urash (2005) for Eocene deposits, the glauconitization process can result in the formation of fining-upward parasequences in deeper shelf settings wherein sea-level controlled facies shifts are not recorded.

7.4 Origin of the Clayton Limestones

The occurrence of fine-grained, bedded and nodular limestones in the study section requires some discussion. In a previous study, Huchison and Savrda (1994) attributed limestone/mudstone couplets in the Pine Member of the Clayton Formation to sea-level-controlled dilution cycles. They suggested that the limestones represent periods of short-term sea-level rise when the supply of clastic sediments was reduced, while mudstones record stillstands or minor relative sea-level drops. In this interpretation, each

limestone/mudstone pair would represent a parasequence. However, this is inconsistent with observations in the current study. As a generalization, most of the limestones in the condensed section/highstand systems tract occur in the relatively glauconite-poor upper parts of parasequences (or tops of 5th-order minicycles) that were deposited at relatively high sedimentation rates. Hence, the limestones cannot be attributed to dilution.

How and why then did the limestones form? Certain limestone intervals (e.g., in units 13 and 16) are nodular and clearly diagenetic. Notably, all other limestones in the highstand systems tract are characterized by the same microspar textures that are observed in the nodular limestones. This may indicate that all limestone units (both bedded and nodular) in the highstand systems tract have a common *diagenetic* origin. That is, they all may have formed as concretions well after deposition of the host sediments. In this case, carbonate precipitation may be related yet to marine flooding and clastic starvation. The position of limestones in upper parts of parasequences is consistent with a mechanism whereby marine flooding and associated processes (e.g., glauconization of carbonate grains) resulted in selective carbonate precipitation in pre-existing sediments *below* marine flooding surfaces. The viability of this mechanism is worthy of future study.

8.0 CONCLUSIONS

The Pine Barren Member of the Lower Paleocene Clayton Formation exposed in central Alabama contains a single 3rd-order, passive-margin shelf depositional sequence composed of glauconitic muddy sands, sandy muds, and limestones. This sequence was the subject of a detailed sedimentologic study designed mainly to test relationships between glauconite abundance and maturity and sequence stratigraphic context. Major conclusions of this study are as follows:

(1) Glauconite abundance and maturity vary predictably between systems tracts. In lowstand incised valley fill sands, glauconite is rare and mainly detrital. Lower parts of the transgressive systems tract are characterized by low to moderate abundances of glauconite, representing a mixture of detrital and authigenic varieties. The condensed section is marked by peak abundances of mature glauconite, as well as by coarsest sand fractions and common skeletal debris. Glauconite abundance and maturity generally decrease upward through the highstand systems tract.

(2) Parasequences can be delineated based on asymmetric cycles in sediment texture and glauconite content. From bottoms to tops of parasequences, total glauconite content, abundance of mature glauconite grain morphotypes, and K and Fe contents of glauconite decrease, and glauconite becomes lighter green in color.

(3) Results generally support observations by previous workers regarding glauconite maturity indicators. As proposed by Huggett and Gale (1997), vermicular

grains represent a lower degree of maturity than mammillated, lobate, and capsule-shaped grains. In the current study, variations in glauconite color and K₂O contents reflect differences in maturity at the parasequence scale. However, structural states of glauconite reflected by x-ray diffraction signatures appear to reflect only longer-term changes in maturity.

(4) Unlike those typical of foreland basin successions, parasequences formed on sediment-starved passive margins may be characterized by fining-upward sequences. This upward fining reflects the glauconitization process rather than detrital grain texture and should not be misinterpreted to represent waning energy or deepening.

(5) Observations made in the current study indicate that limestones in the Pine Barren Member are most prevalent in upper parts of parasequences and are likely diagenetic in origin. They do not reflect primary deposition of carbonate during episodes of marine flooding and clastic sediment starvation as previously suggested.

REFERENCES

- AMOROSI, A., 1995, Glaucony and sequence stratigraphy: A conceptual framework of distribution in siliciclastic sequences: *Journal of Sedimentary Research*, v. B65, p. 419-425.
- AMOROSI, A., 1997, Detecting compositional, spatial, and temporal attributes of glaucony: a tool for provenance research: *Sedimentary Geology*, v. 109, p. 135-153.
- AMOURIC, M., and PARRON, C., 1985, Structure and growth mechanism of glauconite as seen by high-resolution transmission electron microscopy: *Clays and Clay Minerals*, v. 33, no. 6, p. 473-482.
- ANDERSON, A., JONAS, E.C., and ODUM, H.T., 1958, Alteration of clay minerals by digestive processes of marine organisms: *Science*, v. 127, p. 190-191.
- BAUM, G.R., and VAIL, P.R., 1988, Sequence stratigraphic concepts applied to Paleogene outcrops, Gulf and Atlantic basins, *in* Wilgus, C.K., Hastings, B. S., Ross, C.A., Posamentier, H.W., Van Wagoner, J., and Kendall, C.G., eds., *Sea-level Changes: An Integrated Approach*: Society of Economic Paleontologists and Mineralogists, Special Publication 42, p. 309-327.
- BHATTACHARYA, J., and WALKER, R.G., 1991, Allostratigraphic subdivision of the Upper Cretaceous, Dunvegan, Shaftesbury, and Kaskapau Formations in the subsurface of northwestern Alberta: *Bulletin of Canadian Petroleum Geology*, v. 39, p. 145-164.
- BIRCH, G.F., WILLIS, J.P., and RICKARD, R.S., 1976, An electron microprobe study of glauconites from the continental margin off the west coast of South Africa: *Marine Geology*, v. 22, p. 271-283.
- BLOTT, S.J., 2000, GRADISTAT (Version 4): A Grain Size Distribution and Statistics Package for the Analysis of Unconsolidated Sediments by Sieving or Laser Granulometer. (URL: http://www.kpal.co.uk/gradistat_abstract.htm; last accessed 26 July 2007).
- BORNHOLD, B.D., and GIRESSE, P., 1984, Glauconitic sediments on the continental shelf off Vancouver Island, British Columbia, Canada: *Journal of Sedimentary Petrology*, v. 55, p. 653-664.

- BOURGEOIS, J., HANSEN, T.A., WIBERG, P.L., and KAUFFMAN, E.G., 1988, A tsunami deposit at the Cretaceous-Tertiary boundary in Texas: *Science*, v. 241, p. 557-570.
- CHAFETZ, H.S., and REID, A., 2000, Syndepositional shallow-water precipitation of glauconitic minerals: *Sedimentary Geology*, v. 136, p. 29-42.
- DELIUS, H., KAUPP, A., MULLER, A., and WOHLBERG, J., 2001, Stratigraphic correlation of Miocene to Plio-/Pleistocene sequences on the New Jersey shelf based on petrophysical measurements from ODP leg 174A: *Marine Geology*, v. 175, p. 149-165.
- DONOVAN, A.D., BAUM, G.R., BLECHSCHMIDT, G.L., LOUTIT, T.S., PFLUM, C.E., and VAIL, P.R., 1988, Sequence stratigraphic setting of the Cretaceous-Tertiary boundary in central Alabama, *in* Wilgus, C.K., Hastings, B. S., Ross, C.A., Posamentier, H.W., Van Wagoner, J., and Kendall, C.G., eds., *Sea-level Changes: An Integrated Approach*: Society of Economic Paleontologists and Mineralogists, Special Publication 42, p. 299-308.
- DREVER, J.I., 1973, The preparation of oriented clay mineral specimens for X-ray diffraction analysis by a filter-membrane peel technique: *American Mineralogist*, v. 58, p. 553-554.
- DUPLAY, J., and BUATIER, M., 1990, The problem of differentiation of glauconite and Celadonite: *Geochemistry of the Earth's surface and of mineral formation*, 2nd International Symposium, France, p. 264-266.
- ERRAIOUI, L., SRASRA, E., ZARGOUNI, F., and TAJEDDINE, K., 2005, Petrological and physico-chemical investigations of a Tunisian glauconitic deposit: *Journal de Physique IV France*, v. 123, p. 71-74.
- FOLK, R.L., and WARD, W.C., 1957, Brazos River bar [Texas]: a study in the significance of grain size parameters: *Journal of Sedimentary Petrology*, v. 27, p. 3-26.
- FREY, R.W., and HOWARD, J.D., 1990, Trace fossils and depositional sequences in a clastic shelf setting, Upper Cretaceous of Utah: *Journal of Paleontology*, v. 64, p. 803-820.
- GRESSE, P., and WEIWIÓRA, A., 2001, Stratigraphic condensed deposition and diagenetic evolution of green clay minerals in deep water sediments on the Ivory Coast-Ghana Ridge: *Marine Geology*, v. 179, p. 51-70.
- HABIB, D., MOSHKOVITZ, S., and KRAMER, C., 1992, Dinoflagellate and calcareous nannofossil response to sea-level change in Cretaceous-Tertiary boundary sections: *Geology*, v. 20, p. 165-168.

- HARRIS, L.C., and WHITING, B.M., 2000, Sequence-stratigraphic significance of Miocene to Pliocene glauconite-rich layers, on- and offshore of the US Mid-Atlantic margin: *Sedimentary Geology*, v. 134, p. 129-147.
- HESSELBO, S.P., and HUGGETT, J.M., 2001, Glaucony in ocean-margin sequence stratigraphy (Oligocene-Pliocene, offshore New Jersey, U.S.A.; ODP Leg 174A): *Journal of Sedimentary Research*, v. 71, p. 599-607.
- HILDEBRAND, A.R., PENFIELD, G.T., KRING, D.A., PILKINGTON, M., CAMARGO, A.Z., JACOBSEN, S.B., and BOYNTON, W.V., 1991, Chicxulub crater: A possible Cretaceous/Tertiary boundary impact crater on the Yucatan Peninsula, Mexico: *Geology*, v. 19, p. 867-871.
- HUCHISON, R.A., and SAVRDA, C.E., 1994, Rhythmic bedding in the Pine Barren Member of the Clayton Formation (lower Paleocene), Alabama: *Southeastern Geology*, v. 34, no. 2, p. 57-77.
- HUCHISON, R.A., 1993, Character and origin of the rhythmic bedding in the Pine Barren Member of the Clayton Formation, Lower Paleocene, Alabama: Unpublished MS thesis, Auburn University, 145 p.
- HUGGETT, J.M., 2005, Glauconites: Minerals, p. 542-548.
- HUGGETT, J.M., and GALE, A.S., 1997, Petrology and paleoenvironmental significance of glaucony in the Eocene succession at Whitecliff Bay, Hampshire Basin, UK: *Journal of the Geological Society, London*, v. 154, p. 897-912.
- KELLY, J.C., and WEBB, J.A., 1999, The genesis of glaucony in the Oligo-Miocene Torquay Group, southeastern Australia: petrographic and geochemical evidence: *Sedimentary Geology*, v. 125, p. 99-114.
- KITAMURA, A., 1998, Glaucony and carbonate grains as indicators of the condensed section: Omma Formation, Japan: *Sedimentary Geology*, v. 122, p. 151-163.
- LAMOREAUX, P.E., and TOULMIN, L.D., 1959, Geology and ground water resources of Wilcox County, Alabama: Alabama Geological Survey County Report no. 4, 280 p.
- LOGVINENKO, N.V., 1982, Origin of Glauconite in the recent bottom sediments of the ocean: *Sedimentary Geology*, v.31, p. 43-48.
- MANCINI, E.A., and TEW, B.H., 1993, Eustasy versus subsidence: Lower Paleocene depositional sequences from southern Alabama, eastern Gulf Coastal Plain: *Geological Society of America Bulletin*, v. 105, p. 3-11.

- MANCINI, E.A., PUCKETT, T.M., TEW, B.H., and SMITH, C.C., 1995, Upper Cretaceous sequence stratigraphy of the Mississippi-Alabama area: Transactions, Gulf Coast Association of Geological Societies, v. 45, p. 377-384.
- MANCINI, E.A., and TEW, B.H., 1988, Paleogene stratigraphy and biostratigraphy of southern Alabama: Field trip guidebook for the GCAGS-GCS/SEPM, 38th annual convention, New Orleans, Louisiana, Oct. 19-21; Geological Survey of Alabama, Tuscaloosa, 63 p.
- MANCINI, E.A., TEW, B.H., and SMITH, C.C., 1989, Cretaceous-Tertiary contact, Mississippi and Alabama: Journal of Foraminiferal Research v. 19, p. 93-104.
- MCRAE, S.G., 1972, Glauconite: Earth Science Review, v. 8, p. 397-440.
- MOORE, D.M., and REYNOLDS, R.C. Jr., 1989, X-Ray Diffraction and the Identification and Analysis of Clay Minerals: Oxford University Press, Oxford, 1st ed., 332 p.
- MOORE, D.M., and REYNOLDS, R.C. Jr., 1997, X-Ray Diffraction and the Identification and Analysis of Clay Minerals: Oxford University Press, Oxford, 2nd ed., 378 p.
- ODIN, G.S., and FULLAGAR, P.D., 1988, Geological significance of the Glaucony Facies. In: Odin, G.S. (Eds.). Green Marine Clay, Elsevier, Amsterdam, p. 295-332.
- ODIN, G.S., and MORTON, A.C., 1988, Authigenic green particles from marine environments. *in* Chilingarian, G.V., Wolf, K.H. eds., Diagenesis II. Developments in Sedimentology 43: Elsevier, Amsterdam, p. 213-264.
- ODIN, G.S., and MATTER, A., 1981, De glauconiarum origine: Sedimentology, v. 28, p. 611-641.
- PEMBERTON, S.G., MACEACHERN, J.A., and FREY, R.W., 1992, Trace fossils facies models: environmental and allostratigraphic significance. *in*: Walker, R.G., James, N.P. (eds.), Facies Models Response to Sea Level Change: Geological Association Canada, p. 47-72.
- POSAMENTIER, H.W., and VAIL, P.R., 1988, Eustatic controls on clastic deposition II – Sequence and systems tract models, *in* Wilgus, C.K., Hastings, B. S., Ross, C.A., Posamentier, H.W., Van Wagoner, J., and Kendall, C.G., eds., Sea-level Changes: An Integrated Approach: Society of Economic Paleontologists and Mineralogists, Special Publication 42, p. 125-154.
- PRYOR, W.A., 1975, Biogenic sedimentation and alternation of argillaceous sediments in shallow marine environments: Geological Society of America Bulletin, v. 86, p. 1244-1254.

- RUFFEL, A., and WACH, G., 1998, Firmgrounds – Key surfaces in the recognition of parasequences in the Aptian Lower Greensand Group, Isle of Wight (southern England): *Sedimentology*, v. 45, p. 91-107.
- SAVRDA, C.E., 1991, Ichnology in sequence stratigraphic studies: An example from Lower Paleocene of Alabama: *Palaios*, v. 6, p. 39-53.
- SAVRDA, C.E., 1993, Ichnosedimentologic evidence for a noncatastrophic origin of Cretaceous-Tertiary boundary sands in Alabama: *Geology*, v. 21, p. 1075-1078.
- SMIT, J., ROEP, T.B., ALVAREZ, W., MONTANARI, A., CLAEYS, P., GRAJALES-NISHIMURA, J.M., and BERMUEDEZ, J., 1996, Coarse grained, clastic sandstone complex at the K/T boundary around the Gulf of Mexico: Deposition by tsunami waves induced by the Chicxulub impact? *in* Ryder, G., Fastovski, D., and Gratner, S., eds., *The Cretaceous-Tertiary Event and Other Catastrophes in Earth History: Geological Society of America Special Paper No. 307*, p. 151-182.
- SMITH, E.A., JOHNSON, L.C., and LANGDON, D.W., JR., 1894, *Geology of the coastal plain of Alabama: Alabama Geological Survey, Special Report, 6, 759 p.*
- SRASRA, E., and TRABELSI-AYEDI, M., 2000, Textural properties of acid activated glauconite: *Applied Clay Science*, v. 17, p. 71-84.
- TAPPER, M., and FANNING, D.S., 1968, Glauconite pellets: similar X-ray patterns from individual pellets of lobate and vermiform morphology: *Clays and Clay Minerals*, v. 16, p. 275-283.
- THOMPSON, G.R., and HOWER, J., 1975, The mineralogy of glauconite: *Clays and Clay Minerals*, v. 23, p. 289-300.
- TRIPLEHORN, D.M., 1966, Morphology, internal structure, and origin of glauconite pellets: *Sedimentology*, v. 6, p. 247-266.
- URASH, R.G. II, 2005, *Sedimentology and ichnology of a passive margin condensed section, Eocene Lisbon Formation, Southern Alabama: Unpublished MS thesis, Auburn University, 100 p.*
- VAN WAGONER, J.C., MITCHUM, R.M., CAMPION, K.M., and RAHMANIAN, V.D., 1990, Siliciclastic sequence stratigraphy in well logs, cores, and outcrops: Concepts for high-resolution correlation of time and facies: *AAPG Methods in Exploration Series*, No. 7, 55 p.

VAN WAGONER, J.C., POSAMENTIER, H.W., MITCHUM, R.M., VAIL, P.R., SARG, J.F., LOUTIT, T.S., and HARDENBOL, J., 1988, An overview of the fundamentals of sequence stratigraphy and key definitions, *in* Wilgus, C.K., Hastings, B. S., Ross, C.A., Posamentier, H.W., Van Wagoner, J., and Kendall, C.G., eds., *Sea-level Changes: An Integrated Approach*: Society of Economic Paleontologists and Mineralogists, Special Publication 42, p. 39-45.

APPENDIX

Table TA1 – Abundances (weight percent) of major oxides in glauconite grains as determined by microprobe analyses.

Sample MC-8-0-5										
Weight Percent Oxides										
	13a	13b	13c	13d	13e	13f	13g	13h	13i	13j
SiO ₂	50.50	48.12	46.68	37.40	43.17	47.78	50.08	48.07	48.78	50.10
TiO ₂										
Al ₂ O ₃	4.60	7.69	6.53	6.88	5.09	6.39	6.06	5.17	5.00	5.24
FeO	23.74	22.85	23.69	29.39	26.39	21.76	22.91	23.78	24.37	24.15
MnO										
MgO	3.89	3.54	3.61	3.07	3.90	3.76	3.87	4.10	4.34	4.14
CaO	0.49	0.43	0.36	0.40	0.50	0.53	0.56	0.31	0.49	0.38
Na ₂ O	0.00	0.05	0.03	0.00	0.02	0.00	0.01	0.03	0.03	0.01
K ₂ O	6.07	6.64	6.66	4.80	5.29	6.19	6.51	7.55	6.49	7.30
Sum	89.28	89.32	87.56	81.94	84.36	86.41	90.00	89.00	89.50	91.33
Mineral Formulas on Basis of 22 Oxygen										
Si	7.983	7.618	7.620	6.879	7.470	7.776	7.838	7.750	7.78	7.82
Ti	0.000	0.000	0.000	0.000	0.000	0.000	0.000	0.000	0.00	0.00
iv AL	0.017	0.382	0.380	1.121	0.530	0.224	0.162	0.250	0.22	0.18
vi AL	0.840	1.053	0.877	0.371	0.508	1.002	0.956	0.732	0.72	0.79
Fe	3.138	3.025	3.234	4.521	3.819	2.962	2.999	3.206	3.25	3.15
Mn	0.000	0.000	0.000	0.000	0.000	0.000	0.000	0.000	0.00	0.00
Mg	0.917	0.835	0.878	0.842	1.006	0.912	0.903	0.985	1.03	0.96
Ca	0.082	0.073	0.064	0.078	0.092	0.093	0.093	0.054	0.08	0.06
Na	0.000	0.015	0.010	0.001	0.005	0.000	0.002	0.010	0.01	0.00
K	1.224	1.341	1.387	1.127	1.168	1.285	1.300	1.553	1.32	1.45
Si + iv Al	8.00	8.00	8.00	8.00	8.00	8.00	8.00	8.00	8.00	8.00
Sum vi	4.98	4.99	5.05	5.81	5.42	4.97	4.95	4.98	5.09	4.97
Na+K	1.22	1.36	1.40	1.13	1.17	1.29	1.30	1.56	1.33	1.46

Table TA1 – Continued.

Sample MC-8-10-20										
Weight Percent Oxides										
	14a	14b	14c	14d	14e	14f	14g	14h	14i	14j
SiO ₂	49.70	48.60	50.02	49.28	50.46	49.90	49.42	48.70	49.30	50.16
TiO ₂										
Al ₂ O ₃	4.40	2.47	4.99	4.66	5.12	2.44	7.24	2.78	2.92	6.32
FeO	25.37	27.29	22.95	26.04	24.98	27.54	23.24	27.16	26.29	23.21
MnO										
MgO	4.18	4.01	4.03	4.27	4.14	4.08	4.24	4.22	3.97	4.01
CaO	0.29	0.23	0.35	0.23	0.40	0.32	0.34	0.22	0.30	0.41
Na ₂ O	0.03	0.00	0.01	0.00	0.00	0.03	0.04	0.04	0.00	0.00
K ₂ O	7.50	7.86	7.18	7.96	7.28	7.69	7.73	7.73	7.37	7.29
Sum	91.48	90.46	89.52	92.44	92.39	91.99	92.25	90.85	90.15	91.40
Mineral Formulas on Basis of 22 Oxygen										
Si	7.824	7.883	7.915	7.729	7.811	7.926	7.617	7.847	7.935	7.773
Ti	0.000	0.000	0.000	0.000	0.000	0.000	0.000	0.000	0.000	0.000
iv AL	0.176	0.117	0.085	0.271	0.189	0.074	0.383	0.153	0.065	0.227
vi AL	0.640	0.355	0.846	0.591	0.746	0.383	0.933	0.376	0.489	0.927
Fe	3.340	3.702	3.037	3.416	3.234	3.658	2.996	3.660	3.539	3.008
Mn	0.000	0.000	0.000	0.000	0.000	0.000	0.000	0.000	0.000	0.000
Mg	0.981	0.970	0.951	0.998	0.955	0.966	0.974	1.014	0.953	0.926
Ca	0.049	0.041	0.059	0.039	0.067	0.054	0.056	0.038	0.051	0.067
Na	0.010	0.000	0.002	0.000	0.000	0.010	0.013	0.012	0.000	0.000
K	1.507	1.627	1.450	1.593	1.438	1.559	1.520	1.589	1.514	1.442
Si + iv Al	8.00	8.00	8.00	8.00	8.00	8.00	8.00	8.00	8.00	8.00
Sum vi	5.01	5.07	4.89	5.04	5.00	5.06	4.96	5.09	5.03	4.93
Na+K	1.52	1.63	1.45	1.59	1.44	1.57	1.53	1.60	1.51	1.44

Table TA1 – Continued.

Sample MC-8-20-25										
Weight Percent Oxides										
	15a	15b	15c	15d	15e	15f	15g	15h	15i	15j
SiO ₂	51.46	50.21	49.15	49.22	49.88	50.21	50.14	49.58	50.90	50.26
TiO ₂										
Al ₂ O ₃	6.45	5.23	4.85	6.42	3.88	3.31	7.09	4.35	7.12	5.37
FeO	24.25	24.11	24.98	22.17	24.93	25.96	23.34	24.77	23.18	24.80
MnO										
MgO	3.65	3.75	3.55	3.53	3.83	4.03	3.90	3.82	3.89	3.59
CaO	0.57	0.39	0.50	0.60	0.28	0.40	0.36	0.34	0.48	0.58
Na ₂ O	0.02	0.00	0.02	0.08	0.07	0.02	0.02	0.00	0.01	0.02
K ₂ O	6.11	6.67	6.71	5.70	7.53	7.22	7.41	6.92	6.86	6.03
Sum	92.50	90.36	89.77	87.72	90.39	91.17	92.26	89.79	92.44	90.65
Mineral Formulas on Basis of 22 Oxygen										
Si	7.831	7.885	7.841	7.849	7.932	7.944	7.699	7.902	7.751	7.864
Ti	0.000	0.000	0.000	0.000	0.000	0.000	0.000	0.000	0.000	0.000
iv AL	0.169	0.115	0.159	0.151	0.068	0.056	0.301	0.098	0.249	0.136
vi AL	0.988	0.853	0.753	1.056	0.659	0.562	0.982	0.719	1.029	0.855
Fe	3.086	3.166	3.333	2.957	3.316	3.435	2.997	3.301	2.952	3.245
Mn	0.000	0.000	0.000	0.000	0.000	0.000	0.000	0.000	0.000	0.000
Mg	0.828	0.878	0.844	0.839	0.908	0.951	0.893	0.908	0.883	0.837
Ca	0.093	0.066	0.085	0.103	0.047	0.067	0.059	0.059	0.079	0.098
Na	0.005	0.000	0.007	0.024	0.020	0.007	0.005	0.000	0.003	0.006
K	1.186	1.337	1.366	1.160	1.528	1.458	1.452	1.407	1.333	1.204
Si + iv Al	8.00	8.00	8.00	8.00	8.00	8.00	8.00	8.00	8.00	8.00
Sum vi	5.00	4.96	5.02	4.96	4.93	5.01	4.93	4.99	4.94	5.04
Na+K	1.19	1.34	1.37	1.18	1.55	1.46	1.46	1.41	1.34	1.21

Table TA1 – Continued.

Sample MC-8-30-40										
Weight Percent Oxides										
	16a	16b	16c	16d	16e	16f	16g	16h	16i	16j
SiO ₂	51.41	49.92	48.86	48.10	49.23	47.15	49.10	47.59	49.83	48.77
TiO ₂										
Al ₂ O ₃	4.80	3.24	3.69	4.39	4.22	3.42	3.27	4.07	4.30	4.95
FeO	23.38	25.55	26.47	25.06	27.18	24.68	25.62	23.83	25.76	25.59
MnO										
MgO	4.27	4.23	3.95	3.37	3.75	3.50	3.97	3.64	3.46	3.59
CaO	0.42	0.25	0.39	0.42	0.28	0.48	0.25	0.49	0.48	0.53
Na ₂ O	0.00	0.01	0.04	0.00	0.00	0.00	0.04	0.04	0.04	0.01
K ₂ O	7.72	7.62	7.32	7.03	7.72	6.19	7.65	6.33	7.36	6.64
Sum	92.00	90.82	90.72	88.37	92.38	85.42	89.91	86.00	91.23	90.07
Mineral Formulas on Basis of 22 Oxygen										
Si	7.931	7.936	7.824	7.845	7.766	7.938	7.913	7.912	7.875	7.783
Ti	0.000	0.000	0.000	0.000	0.000	0.000	0.000	0.000	0.000	0.000
iv AL	0.069	0.064	0.176	0.155	0.234	0.062	0.087	0.088	0.125	0.217
vi AL	0.804	0.543	0.520	0.689	0.550	0.617	0.534	0.709	0.676	0.714
Fe	3.016	3.397	3.545	3.418	3.586	3.475	3.453	3.313	3.405	3.415
Mn	0.000	0.000	0.000	0.000	0.000	0.000	0.000	0.000	0.000	0.000
Mg	0.982	1.002	0.943	0.819	0.882	0.878	0.954	0.902	0.815	0.854
Ca	0.070	0.042	0.066	0.074	0.047	0.086	0.043	0.088	0.081	0.090
Na	0.001	0.004	0.012	0.000	0.000	0.001	0.014	0.011	0.013	0.004
K	1.520	1.546	1.496	1.463	1.554	1.330	1.573	1.343	1.484	1.352
Si + iv Al	8.00	8.00	8.00	8.00	8.00	8.00	8.00	8.00	8.00	8.00
Sum vi	4.87	4.99	5.07	5.00	5.06	5.06	4.98	5.01	4.98	5.07
Na+K	1.52	1.55	1.51	1.46	1.55	1.33	1.59	1.35	1.50	1.36

Table TA1 – Continued.

Sample MC-9-0-3										
Weight Percent Oxides										
	17a	17b	17c	17d	17e	17f	17g	17h	17i	17j
SiO ₂	49.17	50.21	50.01	50.78	49.50	49.42	48.78	49.80	49.46	48.77
TiO ₂										
Al ₂ O ₃	3.57	4.55	4.55	5.55	7.07	5.56	4.93	4.31	2.83	5.13
FeO	26.91	25.06	24.95	24.78	22.75	24.34	25.76	24.73	26.96	25.23
MnO										
MgO	4.12	3.86	4.20	4.37	3.78	3.76	3.72	4.23	4.15	4.15
CaO	0.60	0.62	0.53	0.64	0.90	0.55	0.67	0.67	0.57	0.52
Na ₂ O	0.02	0.02	0.01	0.00	0.00	0.01	0.02	0.02	0.01	0.03
K ₂ O	7.55	7.59	7.58	7.17	6.77	7.40	6.99	7.30	7.60	6.98
Sum	91.93	91.92	91.84	93.28	90.77	91.04	90.86	91.06	91.58	90.81
Mineral Formulas on Basis of 22 Oxygen										
Si	7.795	7.850	7.825	7.765	7.699	7.768	7.745	7.848	7.878	7.723
Ti	0.000	0.000	0.000	0.000	0.000	0.000	0.000	0.000	0.000	0.000
iv AL	0.205	0.150	0.175	0.235	0.301	0.232	0.255	0.152	0.122	0.277
vi AL	0.462	0.689	0.664	0.765	0.995	0.799	0.668	0.648	0.410	0.680
Fe	3.568	3.277	3.265	3.169	2.959	3.200	3.421	3.259	3.591	3.341
Mn	0.000	0.000	0.000	0.000	0.000	0.000	0.000	0.000	0.000	0.000
Mg	0.974	0.900	0.980	0.996	0.876	0.881	0.881	0.994	0.985	0.980
Ca	0.102	0.105	0.089	0.105	0.150	0.093	0.113	0.113	0.097	0.088
Na	0.005	0.007	0.004	0.000	0.000	0.004	0.005	0.006	0.002	0.008
K	1.527	1.514	1.513	1.399	1.344	1.484	1.416	1.468	1.545	1.410
Si + iv Al	8.00	8.00	8.00	8.00	8.00	8.00	8.00	8.00	8.00	8.00
Sum vi	5.11	4.97	5.00	5.04	4.98	4.97	5.08	5.01	5.08	5.09
Na+K	1.53	1.52	1.52	1.40	1.34	1.49	1.42	1.47	1.55	1.42

Table TA1 – Continued.

Sample MC-9-13-25										
Weight Percent Oxides										
	18a	18b	18c	18d	18e	18f	18g	18h	18i	18j
SiO ₂	48	48.79	48.9	47.82	48.14	47.69	43.85	46.29	44.35	50.4
TiO ₂										
Al ₂ O ₃	4.62	4.8	4.12	3.92	3.74	4.8	6.52	4.61	3.92	3.92
FeO	26.07	25.79	26.4	25.76	25.62	25.5	23.92	26.2	26.62	27
MnO										
MgO	3.63	3.66	4.06	3.98	4.06	4.17	3.81	3.97	3.89	4.04
CaO	0.69	1.04	0.59	0.52	0.66	0.61	0.55	0.53	0.61	0.60
Na ₂ O	0.02	0.00	0.01	0.02	0.00	0.01	0.03	0.00	0.05	0.01
K ₂ O	6.71	6.15	7.54	7.58	7.22	7.28	7.26	7.41	7.22	7.41
Sum	89.75	90.23	91.6	89.59	89.43	90.04	85.94	89.01	86.66	93.4
Mineral Formulas on Basis of 22 Oxygen										
Si	7.741	7.770	7.757	7.767	7.805	7.674	7.412	7.608	7.563	7.825
Ti	0.000	0.000	0.000	0.000	0.000	0.000	0.000	0.000	0.000	0.000
iv AL	0.259	0.230	0.243	0.233	0.195	0.326	0.588	0.392	0.437	0.175
vi AL	0.619	0.671	0.527	0.517	0.520	0.585	0.711	0.501	0.351	0.542
Fe	3.516	3.435	3.506	3.499	3.474	3.432	3.381	3.601	3.797	3.504
Mn	0.000	0.000	0.000	0.000	0.000	0.000	0.000	0.000	0.000	0.000
Mg	0.873	0.869	0.960	0.964	0.981	1.000	0.960	0.973	0.989	0.935
Ca	0.120	0.178	0.100	0.090	0.115	0.105	0.100	0.093	0.111	0.100
Na	0.005	0.001	0.004	0.005	0.000	0.002	0.009	0.000	0.017	0.004
K	1.381	1.250	1.526	1.571	1.494	1.495	1.566	1.554	1.571	1.467
Si + iv Al	8.00	8.00	8.00	8.00	8.00	8.00	8.00	8.00	8.00	8.00
Sum vi	5.13	5.15	5.09	5.07	5.09	5.12	5.15	5.17	5.25	5.08
Na+K	1.39	1.25	1.53	1.58	1.49	1.50	1.57	1.55	1.59	1.47

Table TA1 – Continued.

Sample MC-11-24-29									
Weight Percent Oxides									
	27a	27b	27c	27d	27e	27f	27g	27h	27i
SiO ₂	45.93	42.16	47.37	46	46.4	46.5	48.57	45.3	48.26
TiO ₂									
Al ₂ O ₃	5.17	3.69	6.22	5.76	3.35	5.37	4.63	4.52	4.58
FeO	24.45	25.27	23.53	25.8	26.8	25	25.03	23.6	25.16
MnO									
MgO	3.78	3.86	3.74	3.52	3.73	3.72	4.01	3.56	4.16
CaO	0.60	0.49	0.84	0.96	0.62	0.61	0.58	3.55	0.477
Na ₂ O	0.01	0.00	0.01	0.00	0.00	0.03	0.02	0.10	0.004
K ₂ O	6.95	7.23	6.26	6.13	7.43	7.34	7.42	6.04	7.24
Sum	86.9	82.7	87.98	88.2	88.3	88.6	90.26	86.7	89.86
Mineral Formulas on Basis of 22 Oxygen									
Si	7.645	7.549	7.669	7.553	7.726	7.618	7.765	7.589	7.750
Ti	0.000	0.000	0.000	0.000	0.000	0.000	0.000	0.000	0.000
iv AL	0.355	0.451	0.331	0.447	0.274	0.382	0.235	0.411	0.250
vi AL	0.659	0.328	0.855	0.669	0.384	0.655	0.637	0.481	0.617
Fe	3.403	3.784	3.186	3.547	3.734	3.423	3.347	3.298	3.379
Mn	0.000	0.000	0.000	0.000	0.000	0.000	0.000	0.000	0.000
Mg	0.938	1.030	0.903	0.862	0.926	0.908	0.956	0.888	0.996
Ca	0.108	0.094	0.146	0.169	0.111	0.106	0.099	0.637	0.082
Na	0.004	0.000	0.002	0.000	0.001	0.009	0.007	0.033	0.001
K	1.476	1.652	1.293	1.285	1.579	1.534	1.514	1.290	1.484
Si + iv Al	8.00	8.00	8.00	8.00	8.00	8.00	8.00	8.00	8.00
Sum vi	5.11	5.24	5.09	5.25	5.15	5.09	5.04	5.30	5.07
Na+K	1.48	1.65	1.30	1.29	1.58	1.54	1.52	1.32	1.48

Table TA1 – Continued.

Sample MC-13-45-55										
Weight Percent Oxides										
	33a	33b	33c	33d	33e	33f	33g	33h	33i	33j
SiO ₂	50.70	48.97	50.27	50.83	51.08	51.68	50.67	51.65	50.19	51.23
TiO ₂										
Al ₂ O ₃	6.65	6.18	4.42	8.33	8.83	8.77	8.08	8.42	7.26	7.97
FeO	23.60	25.50	25.60	20.18	20.62	20.57	21.53	21.35	25.19	21.64
MnO										
MgO	4.19	4.06	4.11	3.95	3.94	3.89	3.69	3.81	3.90	3.91
CaO	0.87	0.89	0.45	1.58	1.09	1.28	1.14	1.08	0.71	1.12
Na ₂ O	0.00	0.00	0.00	0.00	0.00	0.00	0.04	0.03	0.01	0.03
K ₂ O	6.75	6.63	7.70	5.58	5.56	5.28	5.61	5.98	7.01	5.92
Sum	92.76	92.24	92.55	90.45	91.12	91.47	90.77	92.32	94.26	91.82
Mineral Formulas on Basis of 22 Oxygen										
Si	7.726	7.617	7.827	7.744	7.718	7.755	7.742	7.745	7.597	7.747
Ti	0.000	0.000	0.000	0.000	0.000	0.000	0.000	0.000	0.000	0.000
iv AL	0.274	0.383	0.173	0.256	0.282	0.245	0.258	0.255	0.403	0.253
vi AL	0.920	0.750	0.639	1.240	1.290	1.306	1.198	1.233	0.892	1.168
Fe	3.008	3.317	3.334	2.571	2.606	2.581	2.751	2.677	3.189	2.737
Mn	0.000	0.000	0.000	0.000	0.000	0.000	0.000	0.000	0.000	0.000
Mg	0.952	0.941	0.954	0.897	0.887	0.870	0.841	0.852	0.880	0.881
Ca	0.141	0.149	0.076	0.258	0.176	0.206	0.187	0.173	0.115	0.181
Na	0.000	0.000	0.000	0.000	0.000	0.000	0.012	0.008	0.003	0.009
K	1.313	1.316	1.530	1.085	1.072	1.011	1.094	1.144	1.354	1.142
Si + iv Al	8.00	8.00	8.00	8.00	8.00	8.00	8.00	8.00	8.00	8.00
Sum vi	5.02	5.16	5.00	4.97	4.96	4.96	4.98	4.94	5.08	4.97
Na+K	1.31	1.32	1.53	1.08	1.07	1.01	1.11	1.15	1.36	1.15

Table TA1 – Continued.

Sample MC-13c-147-153										
Weight Percent Oxides										
	43a	43b	43c	43d	43e	43f	43g	43h	43i	43j
SiO ₂	47.67	48.60	47.53	48.27	48.18	47.29	47.93	47.53	49.20	48.11
TiO ₂										
Al ₂ O ₃	5.26	2.98	5.60	4.33	4.95	5.45	4.34	5.66	5.33	3.72
FeO	25.33	25.23	24.63	24.40	23.89	24.81	24.58	25.11	22.69	25.53
MnO										
MgO	3.60	4.49	3.62	4.17	3.64	3.87	3.92	3.79	3.86	4.07
CaO	0.84	0.40	0.88	0.67	0.71	0.60	0.55	0.76	0.66	0.47
Na ₂ O	0.04	0.06	0.01	0.03	0.01	0.01	0.00	0.03	0.00	0.06
K ₂ O	6.42	8.06	6.76	7.51	6.75	7.33	7.75	6.79	7.26	7.61
Sum	89.15	89.82	89.03	89.38	88.14	89.36	89.06	89.67	89.00	89.58
Mineral Formulas on Basis of 22 Oxygen										
Si	7.698	7.868	7.676	7.788	7.817	7.646	7.784	7.64	7.849	7.803
Ti	0.000	0.000	0.000	0.000	0.000	0.000	0.000	0	0	0.000
iv AL	0.302	0.132	0.324	0.212	0.183	0.354	0.216	0.36	0.151	0.197
vi AL	0.700	0.437	0.742	0.611	0.763	0.685	0.615	0.71	0.852	0.515
Fe	3.421	3.416	3.327	3.292	3.242	3.355	3.339	3.38	3.027	3.463
Mn	0.000	0.000	0.000	0.000	0.000	0.000	0.000	0	0	0.000
Mg	0.867	1.084	0.872	1.003	0.880	0.933	0.949	0.91	0.918	0.984
Ca	0.145	0.069	0.152	0.117	0.124	0.104	0.095	0.13	0.114	0.082
Na	0.014	0.019	0.005	0.009	0.003	0.003	0.000	0.01	0	0.019
K	1.323	1.665	1.393	1.546	1.397	1.512	1.606	1.39	1.478	1.575
Si + iv Al	8.00	8.00	8.00	8.00	8.00	8.00	8.00	8.00	8.00	8.00
Sum vi	5.13	5.01	5.09	5.02	5.01	5.08	5.00	5.12	4.91	5.04
Na+K	1.34	1.68	1.40	1.56	1.40	1.52	1.61	1.40	1.48	1.59

Table TA1 – Continued.

Sample MC-14-0-15										
Weight Percent Oxides										
	45a	45b	45c	45d	45e	45f	45g	45h	45i	45j
SiO ₂	50.55	51.21	50.12	50.45	48.98	50.43	47.92	49.65	47.44	48.63
TiO ₂										
Al ₂ O ₃	3.78	8.29	7.80	8.25	5.72	8.77	4.82	3.93	6.51	6.65
FeO	25.12	19.36	21.38	20.60	25.04	20.44	25.06	24.94	23.61	22.01
MnO										
MgO	4.12	3.56	3.37	3.84	3.85	3.72	3.90	4.40	3.65	4.05
CaO	0.39	0.96	0.62	0.92	0.69	0.97	0.67	0.39	0.66	0.89
Na ₂ O	0.01	0.11	0.01	0.00	0.03	0.02	0.05	0.01	0.03	0.02
K ₂ O	7.39	4.84	5.69	5.33	6.13	4.70	6.40	7.69	6.35	5.65
Sum	91.36	88.34	89.01	89.38	90.45	89.05	88.83	91.01	88.24	87.89
Mineral Formulas on Basis of 22 Oxygen										
Si	7.939	7.890	7.806	7.771	7.728	7.755	7.753	7.858	7.654	7.751
Ti	0.000	0.000	0.000	0.000	0.000	0.000	0.000	0.000	0.000	0
iv AL	0.061	0.110	0.194	0.229	0.272	0.245	0.247	0.142	0.346	0.249
vi AL	0.639	1.395	1.238	1.269	0.792	1.345	0.672	0.591	0.892	1
Fe	3.299	2.494	2.785	2.654	3.304	2.629	3.391	3.301	3.186	2.934
Mn	0.000	0.000	0.000	0.000	0.000	0.000	0.000	0.000	0.000	0
Mg	0.965	0.818	0.782	0.882	0.905	0.853	0.941	1.038	0.878	0.962
Ca	0.066	0.159	0.104	0.151	0.117	0.159	0.117	0.066	0.114	0.151
Na	0.005	0.032	0.004	0.000	0.010	0.005	0.015	0.003	0.010	0.006
K	1.481	0.952	1.131	1.048	1.234	0.922	1.321	1.553	1.307	1.149
Si + iv Al	8.00	8.00	8.00	8.00	8.00	8.00	8.00	8.00	8.00	8.00
Sum vi	4.97	4.87	4.91	4.96	5.12	4.99	5.12	5.00	5.07	5.05
Na+K	1.49	0.98	1.14	1.05	1.24	0.93	1.34	1.56	1.32	1.15

Table TA1 – Continued.

Sample MC-15-8-13										
Weight Percent Oxides										
	47a	47b	47c	47d	47e	47f	47g	47h	47i	47j
SiO ₂	45.87	46.09	47.71	46.81	45.98	47.75	47.02	48.06	48.79	48.26
TiO ₂										
Al ₂ O ₃	4.48	5.40	3.79	6.77	7.37	7.45	5.05	6.60	4.02	6.22
FeO	25.97	24.73	26.11	25.23	22.87	23.57	25.42	23.16	24.53	23.77
MnO										
MgO	4.08	4.13	4.09	4.15	3.89	3.79	3.87	3.83	3.89	3.83
CaO	0.89	0.73	0.57	0.87	0.88	1.10	0.87	1.18	0.56	0.92
Na ₂ O	0.00	0.01	0.01	0.03	0.00	0.00	0.01	0.02	0.00	0.00
K ₂ O	6.73	6.87	7.46	5.83	6.24	5.31	6.63	5.69	7.50	6.20
Sum	88.03	87.96	89.73	89.70	87.21	88.98	88.88	88.54	89.29	89.19
Mineral Formulas on Basis of 22 Oxygen										
Si	7.604	7.582	7.750	7.487	7.502	7.579	7.653	7.674	7.870	7.691
Ti	0.000	0.000	0.000	0.000	0.000	0.000	0.000	0.000	0.000	0.000
iv AL	0.396	0.418	0.250	0.513	0.498	0.421	0.347	0.326	0.130	0.309
vi AL	0.480	0.629	0.476	0.763	0.919	0.973	0.621	0.916	0.634	0.859
Fe	3.601	3.402	3.547	3.375	3.121	3.129	3.460	3.093	3.309	3.168
Mn	0.000	0.000	0.000	0.000	0.000	0.000	0.000	0.000	0.000	0.000
Mg	1.008	1.013	0.990	0.989	0.946	0.897	0.939	0.912	0.935	0.910
Ca	0.158	0.129	0.099	0.149	0.153	0.187	0.152	0.203	0.097	0.157
Na	0.000	0.002	0.002	0.008	0.000	0.000	0.005	0.006	0.000	0.000
K	1.424	1.442	1.546	1.190	1.299	1.076	1.377	1.159	1.544	1.261
Si + iv Al	8.00	8.00	8.00	8.00	8.00	8.00	8.00	8.00	8.00	8.00
Sum vi	5.25	5.17	5.11	5.28	5.14	5.19	5.17	5.12	4.98	5.09
Na+K	1.42	1.44	1.55	1.20	1.30	1.08	1.38	1.16	1.54	1.26

Table TA1 – Continued.

Sample MC-15-60-68										
Weight Percent Oxides										
	53a	53b	53c	53d	53e	53f	53g	53h	53i	53j
SiO ₂	47.34	49.57	48.6	48.49	47.15	48.49	49.57	49.26	50.2	48.6
TiO ₂										
Al ₂ O ₃	6.79	7.46	5.76	7.32	6.03	6.79	6.02	7.34	7.71	7.26
FeO	20.13	21.85	22.4	20.68	23.86	21.57	23.21	21.99	19.2	22.1
MnO										
MgO	3.38	3.99	3.71	4.02	3.86	3.98	4.00	3.95	4.01	3.64
CaO	1.05	1.10	1.09	1.15	0.82	1.03	0.60	1.19	1.13	1.15
Na ₂ O	0.03	0.00	0.01	0.03	0.06	0.01	0.01	0.00	0.01	0.04
K ₂ O	5.47	5.98	5.99	5.56	6.62	6.07	7.39	5.84	6	5.69
Sum	84.19	89.94	87.6	87.25	88.4	87.94	90.8	89.56	88.2	88.5
Mineral Formulas on Basis of 22 Oxygen										
Si	7.819	7.704	7.827	7.729	7.637	7.733	7.760	7.698	7.823	7.701
Ti	0.000	0.000	0.000	0.000	0.000	0.000	0.000	0.000	0.000	0.000
iv AL	0.181	0.296	0.173	0.271	0.363	0.267	0.240	0.302	0.177	0.299
vi AL	1.141	1.071	0.920	1.105	0.788	1.010	0.871	1.050	1.240	1.057
Fe	2.781	2.840	3.011	2.757	3.232	2.877	3.039	2.874	2.509	2.929
Mn	0.000	0.000	0.000	0.000	0.000	0.000	0.000	0.000	0.000	0.000
Mg	0.832	0.924	0.890	0.955	0.932	0.946	0.934	0.920	0.932	0.860
Ca	0.185	0.183	0.189	0.196	0.143	0.176	0.101	0.199	0.188	0.195
Na	0.009	0.001	0.003	0.009	0.019	0.004	0.003	0.000	0.004	0.012
K	1.153	1.186	1.230	1.131	1.368	1.235	1.476	1.165	1.194	1.150
Si + iv Al	8.00	8.00	8.00	8.00	8.00	8.00	8.00	8.00	8.00	8.00
Sum vi	4.94	5.02	5.01	5.01	5.09	5.01	4.94	5.04	4.87	5.04
Na+K	1.16	1.19	1.23	1.14	1.39	1.24	1.48	1.16	1.20	1.16

Table TA1 – Continued.

Sample MC-16b-top										
Weight Percent Oxides										
	60a	60b	60c	60d	60e	60f	60g	60h	60i	60j
SiO ₂	49.52	49.75	46.90	49.54	49.15	45.93	49.64	50.32	49.86	50.01
TiO ₂										
Al ₂ O ₃	7.15	8.83	13.20	10.23	10.18	7.78	8.82	6.28	9.57	9.17
FeO	23.46	19.06	13.54	16	16.61	15.7	21.70	22.41	21.11	18.72
MnO										
MgO	4.04	3.89	4.05	4.39	3.99	3.38	4.04	4.27	3.69	4.13
CaO	0.92	1.28	1.27	1.50	1.04	1.02	1.19	0.92	1.31	1.21
Na ₂ O	0.04	0.02	0.08	0.02	0.13	0.05	0.00	0.00	0.03	0.04
K ₂ O	6.51	4.45	2.547	4.45	4.53	4.39	5.33	6.39	4.55	4.67
Sum	91.63	87.29	81.58	86.2	85.64	78.2	90.73	90.6	90.1	87.95
Mineral Formulas on Basis of 22 Oxygen										
Si	7.645	7.758	7.501	7.697	7.708	7.914	7.599	7.801	7.611	7.729
Ti	0.000	0.000	0.000	0.000	0.000	0.000	0.000	0.000	0.000	0.000
iv AL	0.355	0.242	0.499	0.303	0.292	0.086	0.401	0.199	0.389	0.271
vi AL	0.946	1.381	1.989	1.570	1.590	1.494	1.190	0.949	1.333	1.399
Fe	3.029	2.486	1.811	2.084	2.179	2.255	2.778	2.906	2.695	2.419
Mn	0.000	0.000	0.000	0.000	0.000	0.000	0.000	0.000	0.000	0.000
Mg	0.930	0.904	0.966	1.017	0.933	0.868	0.922	0.987	0.840	0.951
Ca	0.152	0.214	0.217	0.250	0.175	0.188	0.195	0.152	0.214	0.200
Na	0.012	0.006	0.024	0.007	0.041	0.015	0.000	0.000	0.007	0.013
K	1.283	0.885	0.520	0.882	0.907	0.965	1.041	1.264	0.886	0.921
Si + iv Al	8.00	8.00	8.00	8.00	8.00	8.00	8.00	8.00	8.00	8.00
Sum vi	5.06	4.98	4.98	4.92	4.88	4.81	5.09	4.99	5.08	4.97
Na+K	1.29	0.89	0.54	0.89	0.95	0.98	1.04	1.26	0.89	0.93